Fabrication and characterization of silicon nanowires for pressure sensing applications

Elham Aghabalaei Fakhri

Thesis of 240 ECTS credits submitted to the Department of Engineering and Faculty of Science at Reykjavík University and University of Iceland in partial fulfillment of the requirements for the joint degree of Doctor of Philosophy

April 16, 2023

Thesis Committee:

Halldór Guðfinnur Svavarsson, Supervisor
Professor, Reykjavik University, Iceland

Snorri Þorgeir Ingvarsson, Supervisor
Professor, University of Iceland, Iceland

Andrei Manolescu, Advisor
Professor, Reykjavik University, Iceland

István Csarnovics, Examiner
Associate Professor, University of Debrecen, Hungary

Anna Kaźmierczak-Bałata, Examiner
Associate Professor, Silesian University of Technology, Poland

Fabrication and characterization of silicon nanowires for pressure sensing applications

Short title: Pressure sensing of silicon nanowires

Copyright © 2023 Elham Aghabalaei Fakhri

Author ORCID: 0000-0002-8771-2005
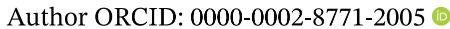

This work is licensed under the Creative Commons Attribution-NonCommercial-NoDerivatives 4.0 International License. You may copy and redistribute the material in any medium or format, provide appropriate credit, link to the license and indicate what changes you made. You may do so in any reasonable manner, but not in any way that suggests the licensor endorses you or your use. You may not use the material for commercial purposes. If you remix, transform or build upon the material, you may not distribute the modified material. The images or other third party material in this thesis are included in the book's Creative Commons license, unless indicated otherwise in a credit line to the material. If material is not included in the book's Creative Commons license and your intended use is not permitted by statutory regulation or exceeds the permitted use, you will need to obtain permission directly from the copyright holder. The use of general descriptive names, registered names, trademarks, service marks, etc. in this publication does not imply, even in the absence of a specific statement that such names are exempt from the relevant protective laws and regulations and therefore free for general use.

Bibliographic information: Elham Aghabalaei Fakhri, 2023, *Fabrication and characterization of silicon nanowires for pressure sensing applications*, PhD dissertation, Department of Engineering, Reykjavík University, Faculty of Science, University of Iceland, 86 pp.

ISBN 978-9935-539-10-6 (print version)
ISBN 978-9935-539-11-3 (electronic version)

Printing: Svansprent ehf.
Font: 10pt stix-2
Printed on 90g Sopor paper

I sincerely dedicate this dissertation to all the women who were unjustly deprived of the opportunity to receive an education.

To my parents for all their sacrifice, love, and support the driving force behind my academic pursuits.

To my precious brother for being an incredible sibling and for always being there for me.

And finally to my beloved husband Hadi, for his unwavering support and for being my partner in life and in academia.

Contents

Contents **iv**

List of Figures **vi**

Abstract **viii**

Acknowledgments **ix**

Preface **xi**

1 Introduction **1**

2 Theoretical frame of reference **3**
2.1 Semiconductors 3
2.2 Silicon 5
2.3 Silicon nanowires, SiNWs 5
2.4 Piezoresistivity 6
2.4.1 Piezoresistance effect in silicon 7
2.4.2 Piezoresistance effect in SiNWs 7
2.5 Memristors 8
2.6 Ohmic and Schottky contacts 9

3 Experiments and methods **13**
3.1 Metal assisted chemical etching, MACE 13
3.2 Deposition by electron-beam evaporation 15
3.3 Photoluminenescence 17
3.4 Piezoresistance analysis 18
3.4.1 Piezoresistance under uniaxial force 18
3.4.2 Piezoresistance in isostatic pressure 21
3.5 X-ray diffraction 23
3.6 Scanning electron microscopy 23

3.7 Energy-dispersive X-ray analysis 24

4 SiNWs as human respiratory sensor 27

4.1 Sensor's mechanism 27

4.2 Experiments on SiNWs as a respiratory sensor 28

5 Summary of papers 31

Paper I 33

Paper II 44

Paper III 55

Paper IV 60

Bibliography 65

List of Figures

2.1 Schematic representation of semiconductors band structure alignment in k-space: (a) direct transition with accompanying photon emission; (b) indirect transition. 4
2.2 Charge Carriers in Semiconductors (electron–hole pairs) and energy Band gap 5
2.3 Unit-cell of the diamond lattice-structure of silicon. 5
2.4 Hysteresis current-voltage characteristics of Al/SiNWs/Al structure synthesized from p-type silicon. 9
2.5 Energy band diagrams of metal and n-type semiconductor contacts. E_{vac} vacuum energy; E_c energy of conduction band minimum; E_v energy of valence band maximum; ϕ_m metal work function; ϕ_s semiconductor work function; κ_s electron affinity of the semiconductor [87]. 11

3.1 Mechanism models for the redox reactions between Si and reactants in solution through a metal catalyst (Ag) during MACE process and formation of SiNWs. 14
3.2 Top-view SEM image of a SiNWs obtained by MACE processing on n-type Si, the scale bar provided is 10 μm. 15
3.3 Schematic of e-beam evaporation technique [96]. 16
3.4 Schematic of co-planar and top-bottom contacts configuration. 16
3.5 Red-shift, RT PL-spectra of synthesized SiNWs by increasing etching time. 18
3.6 Schematic of the force-meter setup for testing PZR characteristics. 19
3.7 Instantaneous resistance (right y-axis, red line) in response to applied force (left 4-axis, blue line) over time. 20
3.8 Resistance vs. applied force for SiNWs samples (blue line), and bulk-Si (red line). Data for SiNWs are average values of four distinct replica samples; the error bars show the range in which the measurements fell on. . . 20
3.9 A photograph of the vacuum chamber and sample during the test. 22

3.10 The resistance of sample E (on a log 10 scale) as a function of pressure measured in the vacuum chamber, is shown with the blue curve. For comparison, in red color, the resistance of a bulk silicon sample (i.e. without nanowires). 22
3.11 Illustration of constructive interference when Bragg´s law is satisfied. . . . 23
3.12 Schematic diagram of SEM. 24
3.13 Components of a modern digital energy dispersive spectroscopy system. . 25
3.14 (a) cross-sectional SEM image, (b) vertical cross-sectional view of wires, and c) respective EDS line-scan analysis (yellow line in (b)) 26

4.1 Schematic of measurement setup for breath monitoring, the inset graph shows an example of long-term breath monitoring in (NB = normal breathing) mode. 29
4.2 Breath sensing test operated in 3 different breathing modes (NB = normal breathing, RB = rapid breathing and DB = deep breathing) for p-type SiNWs with Au electrodes in (a) as-grown state and (b) Ge:SiNWs annealed at 700°C. 30

Fabrication and characterization of silicon nanowires for pressure sensing applications

Elham Aghabalaei Fakhri

March 31, 2023

Abstract

Nanostructures made from crystalline silicon, especially in the form of nanowires (SiNWs), have shown great potential as pressure sensors due to their unique properties such as high sensitivity, small size, and low power consumption. When a force is applied to SiNWs, they undergo a mechanical deformation that results in a change in their electrical resistance. Such an effect has been referred to as the piezoresistance effect. This change in resistance can be measured and used to determine the amount of pressure being applied. By integrating these nanowires into a sensor device, it is possible to create a highly sensitive pressure sensor that can be used in a variety of applications such as in medical devices, aerospace technology, and robotics. Many available techniques can be applied to fabricate such SiNWs. One of the simplest ones is the so-called *metal-assisted-chemical-etching* (MACE) which has gained significant attention in recent years. This process involves the use of a metal catalyst, such as silver, to etch silicon in a controlled manner to produce nanowires with high aspect ratios. The nanowires can be integrated with other materials to create a flexible and stretchable sensor that can conform to curved surfaces and be used in a variety of applications. One advantage of using MACE to fabricate silicon nanowires is that it is a low-cost and scalable process. This makes it possible to produce large quantities of nanowires at a low cost, which is important for commercial applications.

This thesis describes the fabrication of SiNWs using MACE and applications of the SiNWs as an accurate and sensitive pressure sensor for an isostatic and uniaxial load. Its use was further extended to fabricate a novel, small, and compact, breath sensor that could potentially have an impact on sleep research.

Keywords / Efnisord: Silicon nanowires, pressure sensors, piezoresistance

Acknowledgments

I would like to express my sincere gratitude to my supervisors, prof. Halldor Svavarsson, prof. Snorri Ingvarsson, and prof. Andrei Manolescu for providing guidance, support, and encouragement throughout my doctoral studies. Your expertise, insight, and constructive feedback have been invaluable in shaping my research and enhancing its quality.

I would also like to thank a member of our research group, Dr. Muhammad Taha Sultan, for which nothing would have been possible without his valuable support, contributions, and constructive discussions. Further gratitude to our Romanian collaborators, Dr. Neculai Plugaru, and Dr. Rodica Plugaru for their time, effort, and willingness to share their experiences with me.

I am incredibly grateful to all of my fellow colleagues and friends, both in VRIII and Reykjavik University, who have supported me throughout this project.

Finally, I would like to express my deepest appreciation to my family and friends for their love, encouragement, and unwavering support throughout my academic journey. Your belief in me has been a source of strength and inspiration, and I could not have completed this thesis without your support.

Thank you all for your contributions to my research and for being a part of this journey with me.

This dissertation was supported by Reykjavik University Ph.D. fund no. 220006.

Preface

This dissertation is original work by the author, Elham Aghabalaei Fakhri. A major portion of the thesis is based on three refereed journal papers (two published and one submitted), and two refereed conference papers published during the course of Ph.D. study. The published papers appear as per their submitted version at the end of the thesis. The overall list of journal and conference papers throughout this study is listed in below.

Published ISI Journal papers:

- Fakhri, Elham, Rodica Plugaru, Muhammad Taha Sultan, Thorsteinn Hanning Kristinsson, Hákon Örn Árnason, Neculai Plugaru, Andrei Manolescu, Snorri Ingvarsson, and Halldor Gudfinnur Svavarsson. "Piezoresistance characterization of silicon nanowires in uniaxial and isostatic pressure variation." Sensors 22, no. 17 (2022): 6340.
- Plugaru, R., E. Fakhri, C. Romanitan, I. Mihalache, G. Craciun, N. Plugaru, H. Ö. Árnason et al. "Structure and electrical behavior of silicon nanowires prepared by MACE process." Surfaces and Interfaces 33 (2022): 102167.

Refereed conference papers:

- Fakhri E, Sultan MT, Manolescu A, Ingvarsson S, Plugaru N, Plugaru R, Svavarsson HG. "Synthesis and photoluminescence study of silicon nanowires obtained by metal assisted chemical etching." In2021 International Semiconductor Conference (CAS) 2021 Oct 6 (pp. 147-150). IEEE.
- Fakhri, E., M. T. Sultan, A. Manolescu, S. Ingvarsson, and H. G. Svavarsson. "Germanium coated silicon nanowires as human respiratory sensing device." In 2022 International Semiconductor Conference (CAS), pp. 163-166. IEEE, 2022.

Submitted ISI journal paper

- Fakhri, E., M. T. Sultan, A. Manolescu, S. Ingvarsson, and H. G. Svavarsson. "Application of silicon nanowires as human respiratory sensing device - effect of different metal electrodes."

Chapter 1

Introduction

Semiconductors made of silicon (Si) are arguably the most important base material for electronic devices today and like no other material dramatically changed our world. Especially, the whole of information, electronics, and communication technology would have developed completely differently without the availability of silicon. Furthermore, nanostructured Si has been shown to possess some unique properties quite different from its bulk counterpart. Nanostructured Si is a structure made of silicon with at least one dimension in the nanoscale range. Examples include nanowires, quantum dots, nanopillars, nanoparticles, and nanotubes. They have many potential applications in various fields and are considered extremely promising candidates for future high-performance nanoelectronic and nanophotonic devices [1]–[6]. Silicon nanostructures as rods or wires (SiNWs) with nanoscale diameters have been highly investigated in recent decades due to their desired properties and versatile production methods. For some decades, SiNWs have been highly touted as promising building blocks in the fields of nanoelectronics, optoelectronics, energy conversion, energy storage, biochemical and piezoresistive sensors [7]–[13]. SiNWs have been studied on their ability to exhibit high energy peaks of photoluminescence (PL) spectra at room temperature. Strong visible photoluminescence is suitable for the fabrication of light-emitting devices. Studies on the PL spectrum of different types of SiNWs related the origin to the quantum confinement (QC) effects and surface defects [14]–[18]. SiNWs have also been shown to exhibit exceptionally large changes in their electrical resistance upon applied pressure, a property normally referred to as piezo-resistivity. Piezoresistive sensors are among the simplest, most common, and most investigated classes of sensors and continuous efforts are focused on creating further improved devices that can be used in many commercial and non–commercial applications (e.g. evaluation of strain, pressure, acceleration, force, etc.) [19]–[21]. Many commercially available microelectromechanical systems (MEMS), which suffered from low sensitivity, are now using the second generation of such devices, re-

named nanoelectromechanical systems (NEMS), by using nanostructured materials instead of bulk material. In this regard, the new generation of NEMS is developing around using SiNWs instead of bulk silicon. The origin of piezoresistivity has been argued but most frequently it is attributed to surface states [22]. However, to date, most experimental and theoretical studies were focused on PZR effect in a single SiNW and only a few studies exist on PZR effect in arrays of SiNWs, as is done here.

This thesis focuses on the fabrication and preparation of arrays of random SiNWs with metal-assisted catalyzed etching of single crystalline Si-wafers and their characterization through structural, optical, and electrical measurements. The structural characterizations of the samples, in particular, form the base of the study since it strongly affects their optical and electrical properties. The variable parameters in the fabrication process affect the final structure of synthesized SiNWs. In the first step, a comprehensive investigation was carried out to determine the optimal structure. Afterward, the prepared samples were characterized with different methods such as X-ray diffraction, scanning electron microscopy (SEM), and energy-Dispersive X-Ray (EDX) analysis. Depending on the type of electrical measurements, different electrode configurations (either co-planar or top-bottom electrodes) were employed by using electron-beam evaporation. A detailed description of the fabrication process is given in Chapter 3.

The second main subject of the thesis is to investigate the piezoresistance effect, of which a theoretical discussion is given in Chapter 2. As mentioned earlier, a comprehensive study on the piezoresistance effect in arrays of randomly distributed SiNWs is still unavailable and scientists who studied this effect were mainly focused on single SiNWs or periodic arrays under isostatic load. To fill this gap, we employed different types of pressure applications on prepared samples and the results are described in Chapter 3. The results of electrical characterization lead us to a study of the so-called memristive behavior of SiNWs. The theory of memristors is briefly introduced in Chapter 2.

Finally, the SiNWs samples were evaluated as human respiratory (breath) sensors. Chapter 4 is devoted to the respiratory sensor design and tests methods and discussions about the possible mechanisms behind this phenomenon.

Chapter 2

Theoretical frame of reference

2.1 Semiconductors

Semiconductors are a group of materials having conductivity somewhere between those of metals and insulators. Semiconductors may be of a compound type, such as gallium arsenide (GaAs) and indium gallium arsenide (InGaAs), or elemental, such as silicon (Si) and germanium (Ge). If we consider an individual atom, each of its electrons has a certain discrete level of energy. As many atoms come together to form a solid, the energy levels of the electrons merge and form a bundle of energy levels, so-called energy bands, in which the electrons reside. The highest occupied energy band at zero temperature (0 K) is called valence-band, and the first unoccupied band is called conduction-band. These two bands are separated by a certain energy difference, referred to as bandgap or simply energy-gap. A completely filled band or completely empty band cannot carry an electric current. At any temperature above 0 K, a certain population of the outermost electrons has sufficient thermal energy to overcome the bandgap and thus become free to carry a current through the semiconductor. For each electron that leaves the valence-band, a positively charged hole (thus, lack of electron) that also can carry a current, is created in the semiconductor. For undoped (intrinsic) semiconductors, this population increases exponentially with temperature. By substituting some atoms of the semiconductor's crystal lattice with atoms having either fewer or more valence electrons than the host atom (a process called doping), new energy levels are created in the bandgap. Doping atoms having fewer valence electrons are referred to as acceptors, and those with more are referred to as donors. If the donor's population is higher than the acceptor´s population, an excess of loosely bound electrons are created, and the semiconductor is said to be n-conductive or simple being n-type. Vice versa, if the acceptor´s population is higher, the structure lacks electrons, and positively charged holes are created. Such semiconductors are said to be p-conductive or p-type. Semiconductors

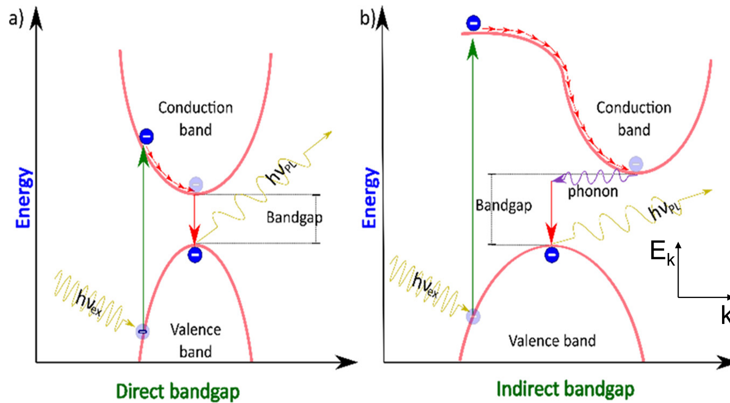

Figure 2.1: Schematic representation of semiconductors band structure alignment in k-space: (a) direct transition with accompanying photon emission; (b) indirect transition.

can further be classified as either direct bandgap or indirect bandgap based on their band structures. In direct bandgap materials, electrons exited over the bandgap to the conduction-band can make the smallest energy transition without changing their momentum. Thus, in order to create a photo-emitted electron-hole pair, in addition to photon emission, a phonon absorption must occur to conserve both momentum ($\vec{k}$-vector) and energy. Similar applies to de-exitation of electrons (electron-hole recombination) where the emission of a phonon is required.

In an indirect transition, a part of the energy is generally given up as heat to the lattice rather than as an emitted photon. This difference between direct and indirect band structures is very important for deciding which semiconductors can be used in devices requiring light output. For example, light emitter semiconductors and lasers generally must be made of materials capable of direct band-to-band transitions or of indirect materials with vertical transitions between defect states. The mechanism of current conduction in semiconductors is similar to insulators at low temperatures and conductors at higher temperatures. They have a filled valence band and an empty conduction band at 0 K, so basically the same structure as insulators. The difference lies in the size of the band gap E_g, which is much smaller in semiconductors than in insulators. The relatively small band gaps of semiconductors allow for the excitation of electrons from the valence band to the conduction band by reasonable amounts of thermal or optical energy. In addition, after electrons are excited to the conduction band, the empty states left in the valence band (holes) can contribute to the conduction process. If the conduction band electron and the hole are created by the excitation of a valence band electron to the conduction band, they are called an electron–hole pair (EHP).

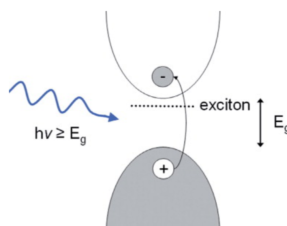

Figure 2.2: Charge Carriers in Semiconductors (electron–hole pairs) and energy Band gap

2.2 Silicon

Silicon (Si) is the world´s most perceived material in modern electronics and optics, mainly due to its abundance, relatively low production cost, and incoherent toxicity [23]. Si crystallizes in a diamond structure with a lattice constant a_0 of 5.431 Å (see Fig. 2.3). Si has an indirect bandgap and, therefore, poor emission properties. Its bandgap is E_g of 1.12 eV which means that intrinsic Si has low conductivity at room temperature. Si is in group IV of the periodic table and thus has 4 valence electrons. By doping with atoms with different valences, such as group III (acceptors) or group V (donors) elements, the resistivity of Si can be varied over a wide range, up to 10 orders of magnitudes.

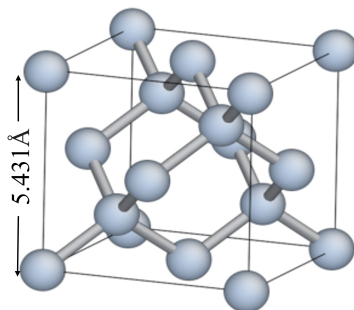

Figure 2.3: Unit-cell of the diamond lattice-structure of silicon.

2.3 Silicon nanowires, SiNWs

Silicon nanowires (SiNWs) are rod-like structures made of silicon with diameters on a nanoscale. Fabrication methods of semiconductor nanowires can be divided into two fundamental types: bottom-up and top-down. With the bottom-up approach,

the nanowires grow up from a substrate and are typically used to fabricate nanowires from III-V semiconductors, but may also be suitable for silicon nanowires [24]. One of the best-known methods is the so-called vapor-liquid-solid (VLS) which relies on the growth of a crystal through direct adsorption of a gas phase onto a solid surface and is generally very slow [25]. In contrast, the top-down methods use material removal to produce nanostructures from a bulk precursor and involve either wet or dry etching of a substrate to a certain depth, such as with laser beam ablation [24], ion beam etching [26], thermal evaporation oxide-assisted growth (OAG) [27], molecular beam epitaxy (MBE) [28], and metal-assisted chemical etching (MACE) [29]. The approaches used for SiNWs fabrication have a crucial impact on their application fields, influencing the performances and the cost of the final devices. Compared to other techniques, MACE offers the perspective of easy integration with microelectronics technologies at a lower cost with larger processable areas. Both disordered and ordered arrays of SiNWs can be obtained by tuning different parameters according to the desired applications, enabling the route for the realization of commercial devices based on SiNWs as electronic circuits. [30], [31]. A more detailed theoretical and experimental demonstration and discussion of structures obtained with this method are given in subsequent sections.

2.4 Piezoresistivity

The term “piezo” is rooted in the term “piezen” from the Greek meaning to press. The history of the piezoresistance (PZR) effect dates back to the late nineteenth century (1856) when the change of resistance in copper and iron wires was discovered [32]. Briefly, the property of some solids to change their electrical resistivity upon applied mechanical stress has been referred to as the piezoresistive effect. ”Piezoelectricity” sounds similar, but with a very different effect, where an electronic charge is generated by applied stress. In contrast to piezoelectric materials, piezoresistive materials are not inherently able to generate an electric signal when strained. The former needs to be supplied by an external voltage source. As Ohm’s law states; the resistance of an electrically conductive rod of length l and cross-sectional area A, with resistivity ρ, is $R = \rho l/A$. By stretching the rod, its length increases, its cross-section area decreases, and its resistance increases. In this case, the change of resistance is strictly related to the change of the geometric parameters of the rod, or in general of the conductor. The piezoresistive effect in semiconductors, which manifests itself at the atomic level is less evident but much more important than the purely geometrical effect and contributes to the dependence of the resistance variation on the strain. The resistivity can change with stress via small changes at the level of the crystalline structure of the material, like inter-atomic spaces or lattice constant [33], [34]. Also, other microscopic details are important for the electrical conduction in this material, such as doping level; due to the sensitivity of the bandgap and effective mass of charge

carriers [34]. Pressure sensors based on this effect are being widely used and commercially available and have the reputation of being robust and reliable [35]. Such sensors made of PZR material have conventionally been in the form of bulk material or thin film [36].

2.4.1 Piezoresistance effect in silicon

The various effects of stress and strain on silicon and silicon technology have been studied since the 1950s. It was recognized early that when the band structure of a material is changed, many material properties are altered, including band gap, the effective mass of carriers, mobility, the diffusivity of dopants, and oxidation rates [37], [38]. The PZR effect was found to be much larger in Si than in other materials [39] and quickly adopted to make sensors based on silicon [40]. Due to its high PZR response and mature processing/fabrication infrastructure, Si has become a natural choice for such devices. Various sensors based on PZR of bulk silicon have been proposed over time, like pressure transducers [41], cantilevers for atomic force microscopy [42], accelerometers [43] and biosensors [44]. Pressure sensors based on PZR of Si have mainly been studied and commercialized because of their high yield and wide dynamic range. Still, they suffer from relatively low sensitivity and large size compared to other common sensors [45].

2.4.2 Piezoresistance effect in SiNWs

In order to overcome the low sensitivity of PZR sensors based on bulk Si, SiNWs PZR sensors were proposed over time. Scaling down the physical dimensions of the sensing units has thus become a focus of interest and many microelectromechanical systems (MEMS) using Si PZR properties are now commercially available. A new generation of such devices, renamed nanoelectromechanical systems (NEMS) has been proposed over the recent years, now using SiNWs instead of bulk Si, more sensitive and faster than the traditional MEMS [46]–[51]. NEMS-based SiNWs sensors have been shown to possess the ability to increase significantly the PZR response, and in fact, the sensitivity of such SiNWs has been referred to as a Giant PZR [52]. The giant PZR was observed in p-doped SiNWs with diameters of 50-350 nm and a length of few μm, initially, under tensile uniaxial stress [52]. However, the PZR effect in n-doped nanowires was found to be comparable to that in the bulk counterpart, both for tensile and compressive uniaxial stress [53]. Many applications based on PZR properties of SiNWs have been proposed, for instance, airflow sensing devices [10], [54], mechanical sensors [55]–[59], pressure sensors [60]–[62], gas sensors [63]–[67], flexible sensors [68]–[72], and human breath sensors [73]. All these experimental devices use either a single SiNWs fixed at both ends (clamped-clamped) or periodic patterned SiNWs arrays, of diameter between few tens and few hundred nm and length of up to several μm. The theoretical origin of the PZR effect in SiNWs has been debated, and

it has been referred to as anomalous PZR effect [10]. It has been related to quantum confinement effects [70], surface charge effects [74], [75], strain-induced bandgap shift [76], or changes in the charge carrier's effective masses [77]. A complex model incorporating these mechanisms has been proposed to quantify analytically the PZR effect in silicon and its nanostructures [34]. We examined the PZR effect in randomly oriented SiNWs in the paper I and discussed its possible origin.

2.5 Memristors

The term "memristor" is an abbreviation of memory resistor, i.e., a resistor having a memory effect. A memristive behavior was predicted by Chua in 1971 from a theoretical study of symmetries in electrical devices and circuits [78]. These electronic devices are non-linear, two-terminal, electrical components that limit or regulate the flow of electrical current in a circuit and remember the amount of charge that has previously flowed through it, and provide key features to combine memory and computational elements at the same location to reduce device size and power consumption. The memristive properties of various electronic devices can be a consequence of several physical and chemical processes, such as; formation of conductive filaments [79], migration of ions and/or dopants [80], or modulation of Schottky barrier heights [81]. Schottky-barrier modulation is especially relevant to our study due to the Schottky junction created by depositing aluminum electrodes on the Si substrates. The properties of the Schottky junction depend on both macro and microscopic features of a semiconductor-metal contact. Two main microscopic components should be taken into account:

- Defective surface states of the semiconductor itself and nanostructures
- Metal-induced gap states (MIGS)

The Schottky junction arises from the abrupt termination of metal and semiconductor lattices (which render some of the forbidden states allowed), followed by electron flow, equilibrating the Fermi levels of both materials. The sign of the accumulated charge of MIGS depends on the work-functions of the metal ϕ_M and the semiconductor ϕ_S. The electron density can shift toward the semiconductor if $\phi_M < \phi_S$, which results in a downward band-bending and positive interface charge. The opposite changes are expected when $\phi_M > \phi_S$. Depending on the relation between work-functions, both positive and negative contributions to surface charge can be expected [82]. A discussion of the results of Ohmic and Schottky contacts will be given in the subsequent section. All these processes contribute to the complex structure of the metal-semiconductor interface and a hysteresis loop should appear in its I-V characteristics. Such characteristics are a fingerprint of a memristor and can be interpreted in terms of memory features of the junction [83]. This kind of hysteresis

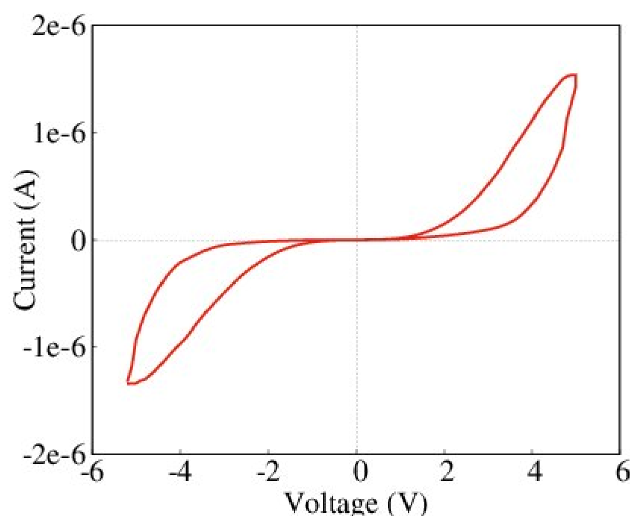

Figure 2.4: Hysteresis current-voltage characteristics of Al/SiNWs/Al structure synthesized from p-type silicon.

I-V characteristics is displayed in Fig. 2.4 which is driven by our synthesized SiNWs with Al contacts (Al/SiNWs) at room temperature which suggests that a process of trapping and de-trapping of (e) charge carriers take place at the Al-SiNWs-Al interface.

2.6 Ohmic and Schottky contacts

A metal contact on a semiconductor can behave in two ways; as a rectifying Schottky contact or as a low-resistant ohmic contact with linear I-V characteristics. The band bending concept was first developed by Schottky and Mott to explain the rectifying effect of metal-semiconductor contacts [84]. Schottky contacts are typical for low-doped semiconductors. In a highly doped semiconductor, the ohmic behavior originates from the tunneling of carriers through the thin Schottky barrier. Semiconductors, depending on their doping state (n- vs p-type conductivity) accumulate charge carriers at the surface, which results in band bending (upward for n-type semiconductors and downward for p-type semiconductors). In the space charge region, the energy band edges in the semiconductor are also shifted continuously due to the electric field between the semiconductor and the metal due to the charge transfer, which is called band bending. Fig. 2.5 shows the ideal energy band diagrams of metal and n-type semiconductor contacts [85]. When the metal and semiconductor are in contact,

the free electrons will transfer between the metal and semiconductor due to the work function difference. When $\phi_m < \phi_s$ in an n-type semiconductor (electrons as the majority of charge carriers), there is no Schottky barrier and the metal-semiconductor contact is ohmic, and when $\phi_m > \phi_s$ barrier forms at the metal-semiconductor interface, which is called the Schottky barrier ϕ_{SB} that the electrons are depleted in the space charge region, and this region is therefore called the depletion layer and it is characterized by an excess positive charge. An opposite trend occurs in p-type semiconductors (holes as the majority of charge carriers); when $\phi_m > \phi_s$ in a p-type semiconductor, there is no Schottky barrier and the metal-semiconductor contact is ohmic, and when $\phi_m < \phi_s$ a Schottky barrier forms at the metal-semiconductor interface and a Schottky contact is formed. In this study, Schottky contacts were obtained by depositing Aluminium (Al) on p-type SiNWs and Gold (Au) on n-type SiNWs; Whereas $\phi_{Al} < \phi_{Si}$ and $\phi_{Au} > \phi_{Si}$ [86].

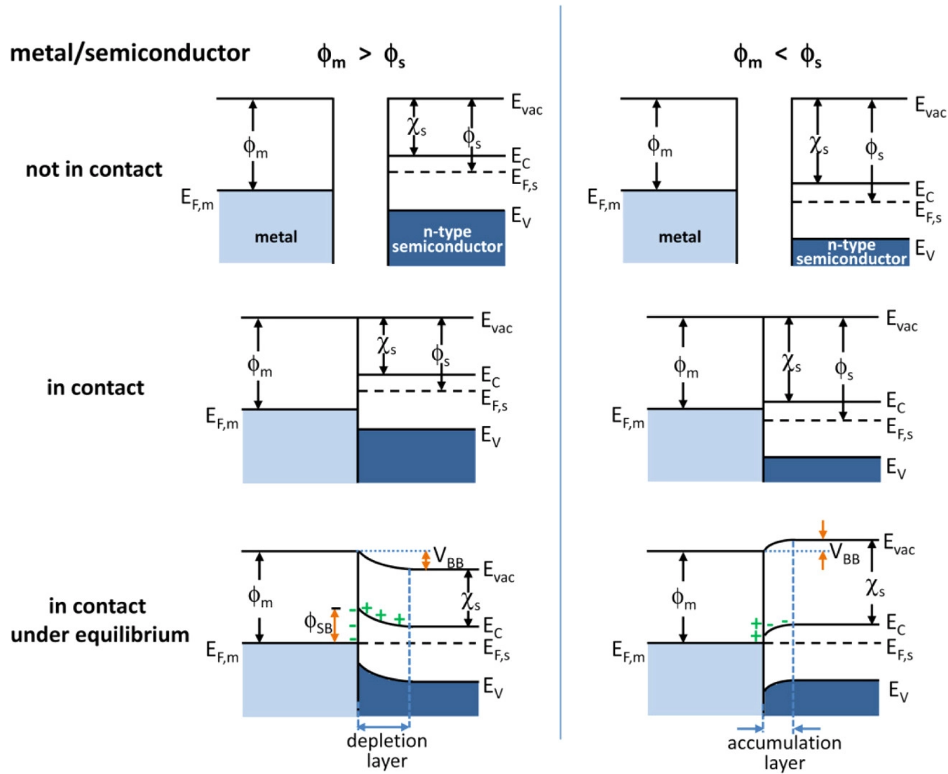

Figure 2.5: Energy band diagrams of metal and n-type semiconductor contacts. E_{vac} vacuum energy; E_{c} energy of conduction band minimum; E_{v} energy of valence band maximum; ϕ_{m} metal work function; ϕ_{s} semiconductor work function; $\varkappa_{\mathrm{s}}$ electron affinity of the semiconductor [87].

Chapter 3

Experiments and methods

This chapter gives a brief overview of methods employed by the author for fabrication as well as a brief description of characterization techniques. After fabrication and characterization, samples undergo structural investigation, surface analysis, electrical and optical measurements. Other characterization methods such as capacitance measurements in Paper II and hydrogenation methods in Paper I which were performed by others will not be described.

3.1 Metal assisted chemical etching, MACE

In 1997, Dimova reported the first demonstration of metal-assisted chemical etching of Si [88]. Porous Si was fabricated by etching an aluminum (Al) covered Si substrate in a solution composed of HF, HNO_3 and H_2O. The widely used MACE method was first investigated in some detail by Li and Bohn, who found that a thin layer of noble metal (e.g., Ag, Au, Pt, or Au/Pd alloy) sputtered on the surface of a Si substrate catalyzed the etching of Si in a mixed solution containing HF, H_2O, and EtOH, resulting in straight pores or columnar structures. The etching method described by Li and Bohn gained increasing attention and various approaches derived from their method were developed to fabricate Si-based nanostructures [89]. Later, in 2002, Peng et al. [90] realized a high density of vertically aligned SiNWs with the MACE by using an $AgNO_3$:HF aqueous solution in a Teflon-lined stainless-steel autoclave. Due to the formation of silver precipitates and to the use of $AgNO_3$, this method is commonly known as the silver salts approach and it is identified as the main single-step MACE approach. In a typical MACE procedure, a Si substrate partly covered by a noble metal is subjected to an etchant composed of HF and an oxidative agent. Typically, the Si beneath the noble metal is etched much faster than the Si without noble metal coverage. As a result, the noble metal sinks into the Si substrate, generating pores in the Si substrate or SiNWs. This also implies that the metal film must be sufficiently

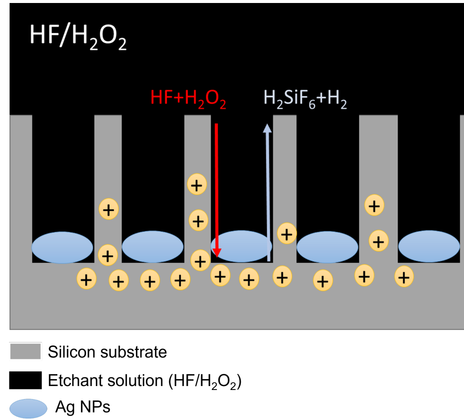

Figure 3.1: Mechanism models for the redox reactions between Si and reactants in solution through a metal catalyst (Ag) during MACE process and formation of SiNWs.

thin (or porous) to allow for a migration of the liquid to the interface. Dissipation of the dissolved product, the metal-silicon interface, must also be active for a fast etching. Si etching and dissolution occur selectively only at the interface between the metal and silicon layer by the redox reaction formulated as stated below:

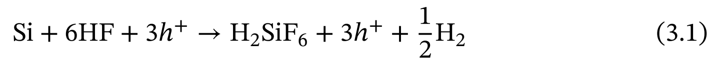

$$Si + 6HF + 3h^+ \rightarrow H_2SiF_6 + 3h^+ + \frac{1}{2}H_2 \tag{3.1}$$

The reduction of an oxidizing agent (in our case H_2O_2) is catalyzed at the surface of a noble metal NPs (in our case Ag). Due to this redox reaction, holes (h^+) inject into the valence band of the Si substrate. These holes weaken chemical bonds in the Si and thus, dissolution of the substrate at the metal-substrate interface takes place. Fig. 3.1 depicts the MACE mechanism and formation of the SiNWs.

The detailed geometries of the resulting SiNWs depend mostly on the initial morphology of the noble metal coverage. Deposition of the noble metal can be done by different methods, for instance; thermal evaporation [91], sputtering [26], electron beam (e-beam) evaporation [92], electroless deposition [93], focused-ion-beam (FIB)-assisted deposition [94], or spin-coating of particles via other methods such as laser interference lithography (LIL)[30], [95]. To obtain patterned structures of Si or periodic SiNWs, LIL+MACE method can be used and the morphology of the noble metal film and consequently, the geometry of the SiNWs can easily be determined by this method [30]. Electroless deposition is a simple and low-cost method for the deposition of noble metals and is usually utilized to deposit the noble metal if there is no strict demand on the morphology of the resulting SiNWs. In this study, electroless deposition of Ag nanoparticles was carried out for SiNWs fabrication, resulting

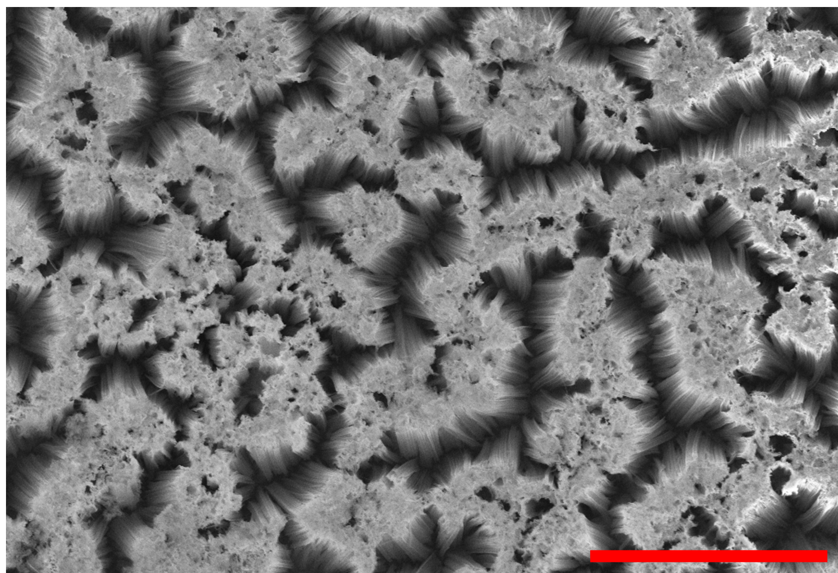

Figure 3.2: Top-view SEM image of a SiNWs obtained by MACE processing on n-type Si, the scale bar provided is 10 μm.

in randomly distributed and interconnected SiNWs with diameters around 50 $\sim$ 150 nm. An SEM image of a typical SiNWs array, is shown in Fig. 3.2.

3.2 Deposition by electron-beam evaporation

Metal contacts were deposited by electron beam (e-beam) evaporation. This technique uses a focused electron beam to heat and evaporates metals. A high-voltage DC source accelerates electrons toward the target material. A schematic of the electrons forming a unified beam by a magnetic field is shown schematically in Fig. 3.3. The e-beam can be generated from electron guns by thermionic emission, accelerated to high kinetic energy, and focused toward the target material. The kinetic energy of the electrons is converted into thermal energy that will increase the surface temperature of the target, leading to evaporation and deposition of the target onto the adjacent substrate. Evaporation occurs at a highly localized point near the beam bombardment site on the surface of the target, minimizing contamination from the crucible. In this study, an e-beam evaporation system (Polyteknik Cryofox Explorer 600 LT) was utilized to deposit metallic contacts (Al or/and Au) on synthesized SiNWs, either two co-planar or top-and-bottom contacts, with respect to the type of electrical measurements. A schematic of co-planar and top-bottom contacts configuration is

depicted in Fig. 3.4.

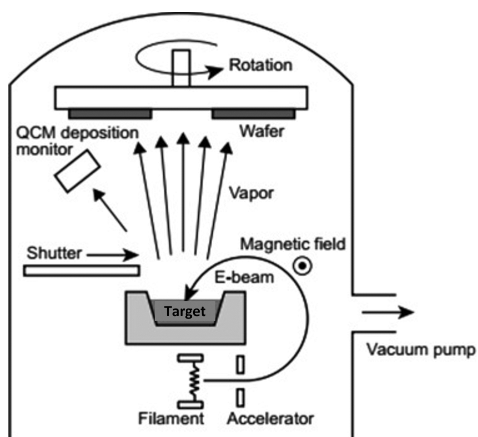

Figure 3.3: Schematic of e-beam evaporation technique [96].

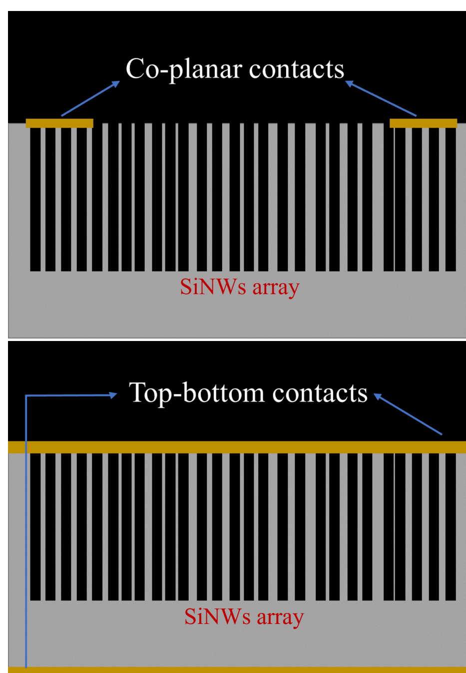

Figure 3.4: Schematic of co-planar and top-bottom contacts configuration.

3.3 Photoluminenescence

The simplest light emission from a semiconductor occurs due to the recombination of an electron-hole pair (EHP) created by the excitation of an electron from valence-band to the conduction-band (also referred to as exciton). Emissions can also originate from defect states located within the bandgap of the semiconductor, upon excitation and subsequent recombination. This general property of the semiconductor's light emission is called luminescence. If the EHPs are created by photon absorption, the resulting radiation is called photoluminescence (PL) [97]. SiNWs have been studied on their ability to exhibit high energy peaks of PL spectra at room temperature, due to quantum confinement (QC) effects and surface defects [16]–[18]. Results of Naffeti et. al. [18], indicated that for the QC effect to take place, the dimension of the nanostructures should be less than the exciton Bohr radius (in principle the physical distance between the electron and the hole of the EHP). However, for NWs with a diameter larger than the excitons Bohr radius (i.e. $\sim$ 5 nm for Si), the resulting PL spectra are unlikely to originate from the SiNWs. In such cases (as in our SiNWs structures), it is more likely that the emission originates from the Si nanocrystals or nanopores on the surface.

In the paper II, our XRD results indicated that the MACE process had caused the formation of 0D defects, nanocrystals, or nanopores on the surface of SiNWs, rather than extended structural defects. In our papers II and III we analyzed the nature of structural defects by recording the PL emission from SiNW arrays using a Princeton Instrument Acton SP2750 triple grating monochromator/spectrograph equipped with a Si-CCD detector. The samples were mounted in a cryogenic pump (Leybold-Heraeus RG 210) and excited with 15 mW HeCd laser of 325 nm wavelength and spot diameter of $\sim$ 100 to 200 μm. A combination of bandpass filters, mirrors, and various lenses mounted over a guided rail was utilized to guide the laser and remove second and higher-order diffractions. The observed red-shift with longer etching time is shown in Fig. 3.5. The enhancement of the PL intensity and the wavelength red-shift could be attributed to increased porosity of the SiNWs surface and a porous Si layer formed at the base of SiNWs, as a result of longer MACE process [98], [99].

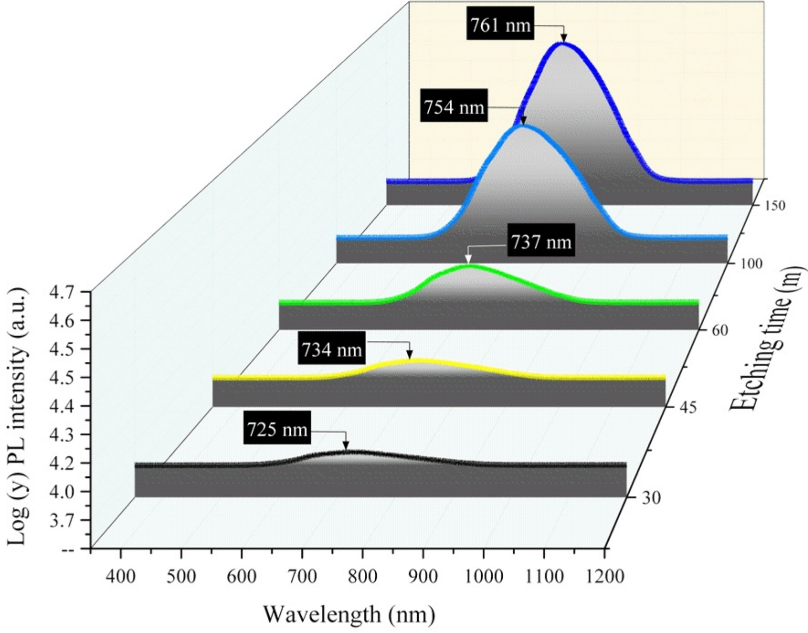

Figure 3.5: Red-shift, RT PL-spectra of synthesized SiNWs by increasing etching time.

3.4 Piezoresistance analysis

With the aim of studying the PZR phenomena in synthesized SiNWs, two different approaches (uniaxial load, and isostatic load) were utilized and will be discussed in this section. The results are published in paper I.

3.4.1 Piezoresistance under uniaxial force

In semiconductors, the inter-atomic spacing may be altered by strain. Consequently, apart from geometric changes in semiconductors, bandstructure-related details, such as the bandgap or effective mass, may change, as well as the resistivity. The quantitative relation between resistivity or conductivity and stress/strain is given by a fourth-rank piezoresistance tensor[40]. When uniaxial stress X is applied to the wires, the PZR coefficient of a wire array with resistivity ρ, in the direction of the stress is defined as

$$\pi_l = \frac{\Delta\rho}{\rho_0}\frac{1}{X}\,, \tag{3.2}$$

where $\Delta\rho$ is the stress-induced change in the resistivity and ρ_0 is the reference resistivity of the unstressed material[52]. The resistivity is then given as the reciprocal of conductivity (the product of carrier concentration, carrier mobility, and charge of the carrier) $\rho = \rho(x) = \frac{1}{n(x)\mu_n(x)q}$. So-called piezoresistivity is observed when an applied strain changes the bandgap and the effective mass of charge carriers, which, in turn, affects the carrier concentration, as well as their mobility [100]. This relationship is linear in a certain range of strain [34], [101]. Niquet et al [102] showed that electron mobility eventually saturates with strain. Subsequently, the PZR response saturates above a certain range of strain. This has been observed experimentally in other studies such as by Kim et al [69], showing SiNWs arrays to exhibit good linearity below a certain amount of pressure.

In this study, a simple measurement setup was utilized to study the PZR under uniaxial force, using a force meter (Mark-10, M5-012). A schematic of the setup is shown in Fig. 3.6. The force meter was mounted on a vertical rod allowing for movement on the z-axis (vertical) by a manually adjusted screw. Uniaxial pressure was applied to the samples by pressing the pin of the force meter into the samples' surface with an intensity determined by the aforementioned screw. Finally, a Keithley 2400 source meter was used to measure the resistance R through the sample as a function of applied pressure at a constant bias voltage of 2 V. Fig. 3.7 shows an example of the PZR response of SiNWs under force variation as a function of time when the force and the instantaneous resistance are measured after applying the force to the SiNWs. As clearly visible, the resistance changes significantly and inversely with pressure. In order to check the repeatability and reproducibility of the sensor, 4 replica samples were fabricated. The same measurements were repeated four times on each replica sample. The results are shown in Fig. 3.8. The error bars show the average values of all measurements on all replica samples. Fig. 3.8 also shows a striking difference between the PZR response of SiNWs vs. bulk Si. No measurable change in resistance is seen for the bulk Si, in very sharp contrast to the SiNWs samples.

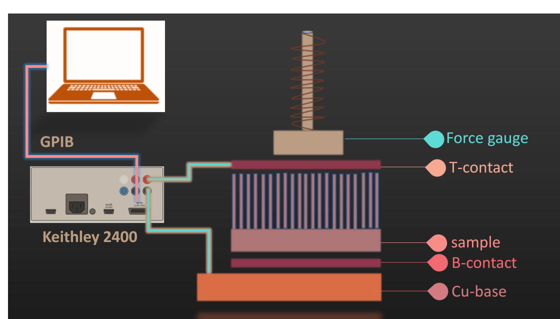

Figure 3.6: Schematic of the force-meter setup for testing PZR characteristics.

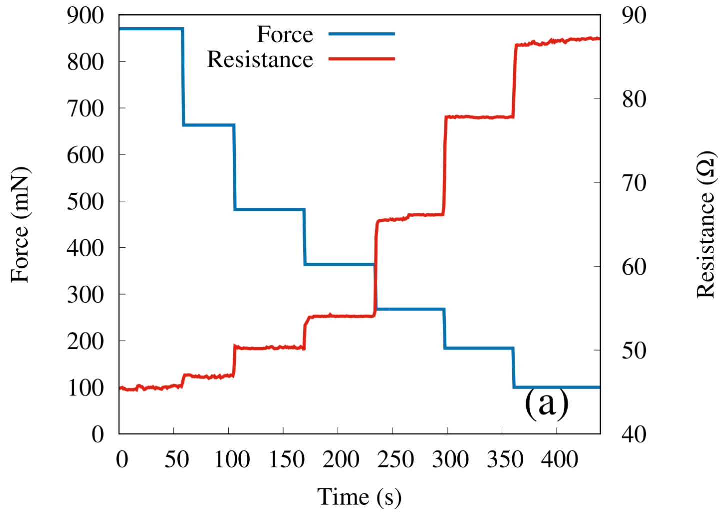

Figure 3.7: Instantaneous resistance (right y-axis, red line) in response to applied force (left 4-axis, blue line) over time.

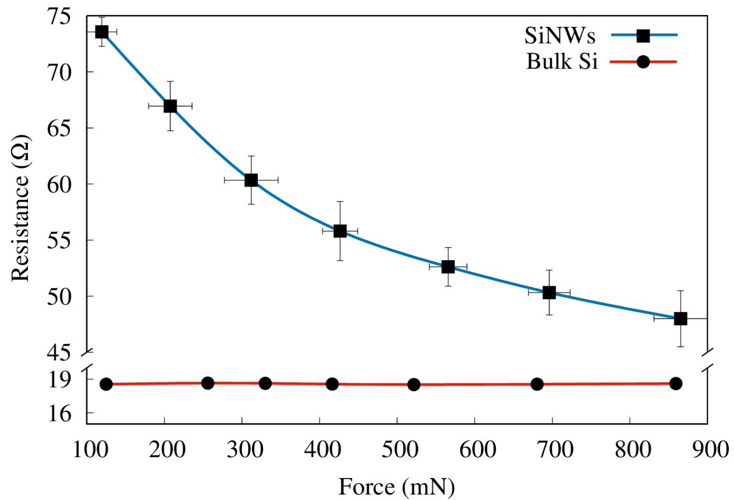

Figure 3.8: Resistance vs. applied force for SiNWs samples (blue line), and bulk-Si (red line). Data for SiNWs are average values of four distinct replica samples; the error bars show the range in which the measurements fell on.

3.4.2 Piezoresistance in isostatic pressure

To date, the origin of the PZR effect in SiNWs has been debated, and most frequently, it is referred to as anomalous PZR [10]. Studies have been focused on using gas flow to apply direct pressure on SiNWs, either single SiNW or arrays of them[11], [57], [103], [104] and SiNWs modified by graphene [105]. Few if any deals with arrays of SiNWs under isostatic load. To fill this gap we studied the SiNWs response in a vacuum chamber, which creates a pressure uniformly distributed on the sample surface.

The resistance over the samples was measured at a fixed bias voltage of 5 V while the air vacuum chamber was either gradually filled with air or evacuated. In order the get maximum exposure to the air, the contacts were made in co-planar configuration, two separate strips on each side of the SiNWs area, instead of top-and-bottom contacts as used for the uniaxial measurements. As shown in the Fig. 3.9, the samples were mounted on a fixed sample station inside the chamber with tungsten needle tip kelvin probes as a steady connection. The chamber was evacuated of air to the pressure of 10^{-4} mbar and the PZR response was tested under repressurizing up to the atmospheric level of 10^3 mbar. A PZR response of a SiNWs sample is shown in Fig. 3.10 with a comparison to a bulk Si. We observed a dramatic increase in the SiNWs resistance by more than two orders of magnitude when pumping the air out of the vacuum chamber, which is significantly higher than for bulk Si. The pressure sensitivity of the sensor in the isostatic pressure variation given by $S = \frac{\Delta R}{R}/\Delta P$ [106], gives the highest sensitivity of $8.8 \times 10^{-3}\text{Pa}^{-1}$, at the pressure range of roughly 10^{-2} and 10^{-1} mbar.

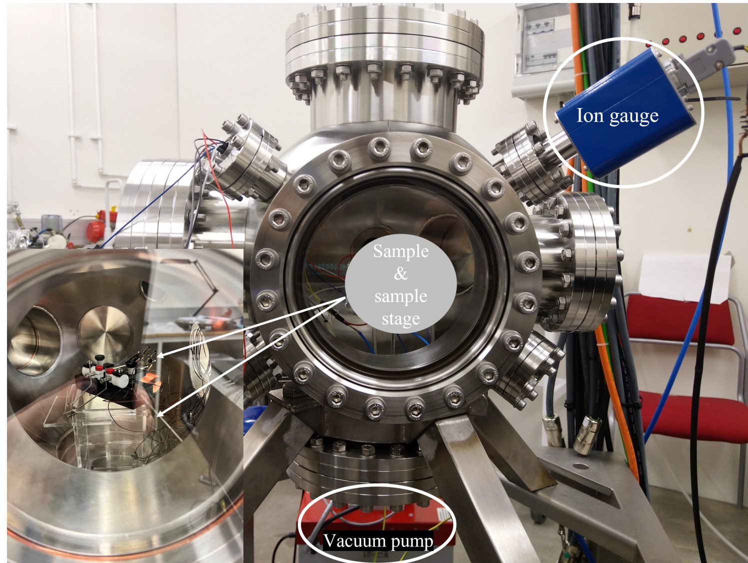

Figure 3.9: A photograph of the vacuum chamber and sample during the test.

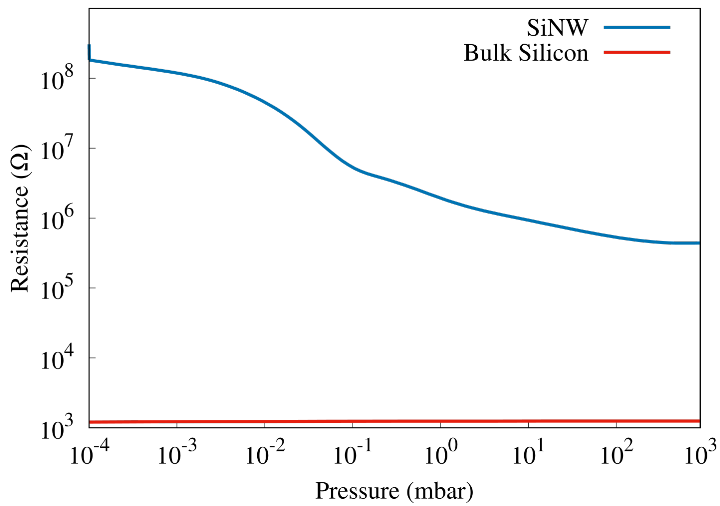

Figure 3.10: The resistance of sample E (on a log 10 scale) as a function of pressure measured in the vacuum chamber, is shown with the blue curve. For comparison, in red color, the resistance of a bulk silicon sample (i.e. without nanowires).

3.5 X-ray diffraction

In 1912, Max von Laue, discovered that crystalline substances act as three-dimensional diffraction gratings for X-ray wavelengths similar to the spacing of planes in a crystal lattice. X-ray diffraction (XRD), is based on constructive interference of monochromatic X-rays in a crystalline sample [107]. This technique is used to study periodically ordered structures at atomic scales. When the X-rays enter the material they will be scattered by the electron clouds around the atoms. The periodicity of the lattice planes gives rise to constructive interference of the X-rays and the intensity of the scattered X-rays can be plotted against the angle 2θ [108], [109]. The interference is described mathematically by Bragg's Law:

$$2d \sin\theta = n\lambda \tag{3.3}$$

Where, d is the separation distance between the Bragg planes, θ is the Bragg angle, n is the diffraction order, and λ is the X-ray wavelength. The term Bragg planes refer to planes that are comprised of these constructively diffracting atoms (see Fig. 3.11). Conversion of the diffraction peaks to d-spacing allows one to identify the chemical composition of the sample because each crystalline material has a set of unique d-spacings. Typically, this is achieved by comparing the obtained results with that of d-spacing from standard reference patterns.

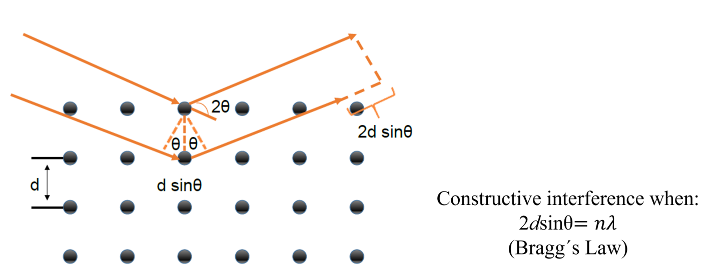

Figure 3.11: Illustration of constructive interference when Bragg´s law is satisfied.

3.6 Scanning electron microscopy

A scanning electron microscope (SEM) can be defined as a tool that uses a beam of electrons to generate images for analysis of the topographic features of a specimen. In contrast to an optical microscope, which uses visible light to illuminate samples and a series of optical lenses to magnify samples in the range approximately between 10 to 1,000 times, the SEM permits the observation of materials down to nm scale. In the SEM, a beam of electrons is focused on a spot volume of the specimen, resulting

in a transfer of energy to the spot. These bombarding electrons, also referred to as primary electrons, dislodge electrons from the specimen itself. The dislodged electrons, known as secondary electrons (SE), are attracted and collected by a positively biased grid or detector and then translated into a signal. Scattered primary electrons can also be used to give an image. To produce an SEM image, the electron beam is swept across the area being inspected, producing many such signals. These signals are then amplified, analyzed, and translated into images of the topography being inspected. Finally, the image is shown on a computer screen. Fig. 3.12 shows the basic structure of an SEM from the link: (https://www.thinkymixer.com).

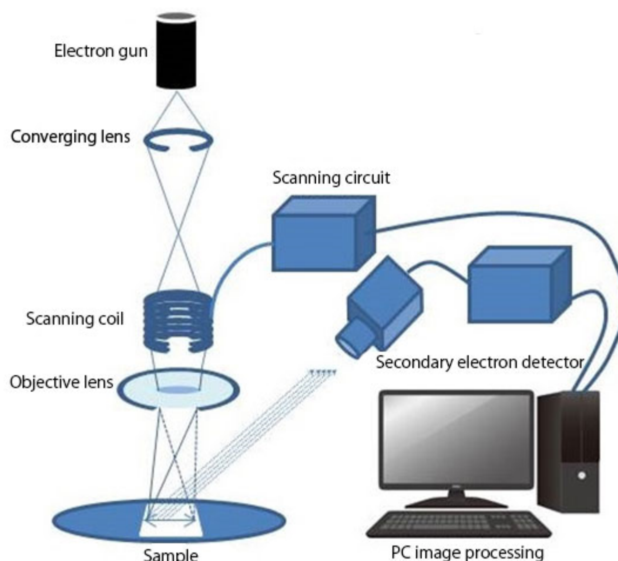

Figure 3.12: Schematic diagram of SEM.

In this study, SEM is applied to get topographic and cross-sectional images of the fabricated SiNWs, along with the elemental and structural determination. Zeiss Supra 35 scanning electron microscope was utilized for structural and elemental analysis.

3.7 Energy-dispersive X-ray analysis

The energy dispersive X-ray (EDX) microanalysis is a technique of elemental analysis associated with electron microscopy and is based on the generation of characteristic X-rays that reveals the presence of elements present in the specimens. This technique is ideal for revealing what elements – and by inference chemical compounds – are

present in a particular specimen. Basically, EDX consists of detecting the characteristic X-rays produced by each element after bombarding a sample with high-energy electrons in an electron microscope. Using a process known as X-ray mapping, information about the elemental composition of a sample can then be overlaid on top of the magnified image of the sample. The spectrum of EDX microanalysis contains both semi-qualitative and semi-quantitative information. The EDX technique is an important tool to detect nanoparticles [110], [111]. Qualitative analysis involves the identification of the lines in the spectrum and is fairly straightforward owing to the simplicity of X-ray spectra. Quantitative analysis (determination of the concentrations of the elements present) entails measuring line intensities for each element in the sample and for the same elements in calibration Standards of known composition. An EDX system typically consists of several key units that is depicted in Fig. 3.13. These include: a semiconductor detector housed with a field-effect transistor (FET) pre-amplifier, cooled to a sub-ambient temperature; and a main amplifier that provides further amplification and a fast pulse inspection function to reduce pile-up events. When the electron beam hits the sample, there is a high probability that an X-ray will be generated. The resulting X-ray escapes the sample and hits the detector which creates a charge pulse in the detector. This short-lived current is then converted into a voltage pulse with an amplitude reflecting the energy of the detected X-ray. Finally, this voltage pulse is converted to a digital signal, and one more count is added to the corresponding energy channel. Once the measurement is completed, the accumulated counts produce a typical X-ray spectrum with the major peaks superimposed on the background.

An EDX analysis was carried out from a cross-sectional SEM image of the Germanium coated SiNWs (Ge:SiNWs) and annealed at 700 °C to explore the distribution of the Ge nanoparticles, and the respective EDX spectra are shown in Fig. 3.14. Figure 3.14(a), shows Ge-nanoparticles (appearing as white spots), roughly 50 nm in diameter, formed on SiNWs after rapid thermal annealing at 700 °C. As seen in Fig. 3.14(b and c), the length of the SiNWs is around 6 μm and the EDX vertical line-spectra indicate that the majority of Ge nanoparticles residing at the tips of the SiNWs rather than covering the side-walls of the wires. The provided results from the EDX analysis will be discussed in detail in the following chapter.

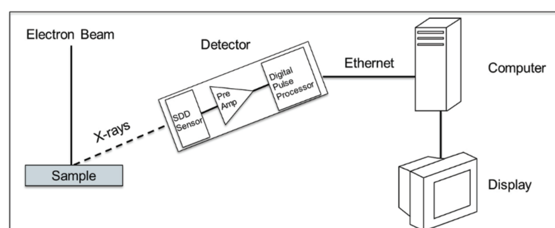

Figure 3.13: Components of a modern digital energy dispersive spectroscopy system.

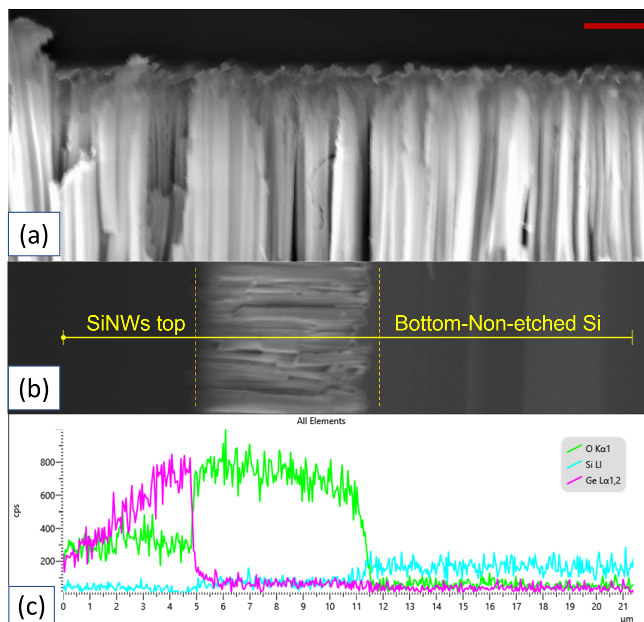

Figure 3.14: (a) cross-sectional SEM image, (b) vertical cross-sectional view of wires, and c) respective EDS line-scan analysis (yellow line in (b))

Chapter 4

SiNWs as human respiratory sensor

Breathing is one of the most fundamental processes of human life, and monitoring it accurately can provide valuable insights into an individual's health and well-being. Human health monitoring requires developing sensors to be able to monitor precisely the vital signs and provide alerts of possible harm in real-time. SiNWs-based sensors can provide real-time analysis of the breath due to their high sensitivity to low-pressure detection which is critical for bio-compatible devices such as breath sensors[10]. The development of SiNWs breath sensors can be traced back to early 2000 when Cui and Lieber et al. first explored the use of SiNWs as transducers for gas-sensing applications which laid the foundation for using SiNWs in breath analysis [112]. In 2011, Chen et al. reported the use of SiNWs for humidity sensing applications, demonstrating their capability to detect humidity changes in real-time [113]. Recently, Gosh, et al. [75] proposed a breath sensor on n-type arrays of periodic silicon nanorods [75] and related this effect to the piezoresistance effect. However, the mechanism behind this effect may be controversial and in the following sections, the possible mechanism behind this effect and respiratory tests will be discussed.

4.1 Sensor's mechanism

It was observed that the electrical resistance over the SiNWs was highly dependent on the breath (thus, inhaling and exhaling) of a human. Such changes in resistance have been referred to as piezoresistance (PZR) or anomalous PZR but surface effects due to humidity or temperature changes may also account for the changes. Section 2.4 provided theoretical discussions on the piezoresistance effect, while section 3.4 covered experimental discussions on the same topic. Briefly, according to the model of piezoresistance effect, any pressure applications such as airflow on the SiNWs surface can impart sufficient normal pressures that can deform the SiNWs and cause a change in the resistance [40]. In our study on the PZR effect on the SiNWs (pa-

per I), we demonstrated that the effect was significantly reduced by hydrogenation. Hydrogenation is known to passivate shallow and deep defects in SiNWs, so these results strongly indicate that surface states may play a significant role in the PZR effect. Surface states of the SiNWs may also have played an important role in the humidity-sensing mechanism described in a review article by Akbari-Saatlu et al. for metal-oxide semiconductors [114]. The humidity sensing mechanism is commonly based on the variations in capacitance or resistance resulting from the adsorption and desorption of water molecules on SiNWs [113], [115]. Research has shown that the adsorption of water on nanowires can alter the conductance and capacitance of porous silicon by changing its dielectric constant or electrical resistance. Additionally, it may result in chemisorption and physisorption on the surface of the silicon, causing changes in its surface states, which can be detected by measuring the current flow through the sensor [116]. In order to determine the source of SiNWs' response to human breath, a qualitative investigation was conducted, utilizing a sensor made of SiNWs, exposed to air, N_2 gas, and human breath. From these experiments, we observed that the humidity level at the SiNWs decreased by 10% and 20% for compressed air and N_2 gas, respectively, compared to the ambient humidity level. In contrast, exposure to human breath resulted in a humidity level increase of up to 35%. While SiNWs demonstrated increased resistance upon exposure to compressed air, N_2 gas, and human breath, the response to breath was more pronounced. Therefore, we can conclude that the breath-sensing mechanism is a combination of piezoresistive response and humidity effect.

4.2 Experiments on SiNWs as a respiratory sensor

The SiNWs samples were synthesized as explained in chapter 3. Two parallel and coplanar metal electrodes (Al, Au, or V) were deposited on SiNWs samples by using an electron beam evaporator. Then the sensor samples were mounted on a ceramic chip having patterned interdigital Au-electrode. Thin Al-wires were attached to coplanar electrodes on the sample's electrodes. The sensor was mounted firmly on to philtrum of a volunteer, using double-sided tape. A schematic of the sensor is given in Fig. 4.1. The connection between the sensor and the signal processing unit was suitably secured inside the cannula tube to prevent any possible loose connections or interference with other objects. The measurement was carried out at a fixed bias voltage of 2 V. Keithly meter 2400 was used to monitor and record the resistance variation. The breathing patterns were obtained by exhaling and inhaling over the samples for three different breathing modes i.e., normal (NB), rapid (RB), and deep breathing (DB). Fig. 4.2 (a) shows an example of the response of a SiNWs sensor breath in the aforementioned three different modes. It can be observed that there is a significant drift in the resistance baseline with time. In order to overcome this issue and to obtain the optimum respiratory sensing, the SiNWs were coated with a

thin film of germanium and annealed at 700°C, using rapid thermal annealing for 5 minutes. A similar respiratory test was repeated on Ge:SiNWs sample, for which the result is shown in Fig. 4.2 (b). It was observed that Ge:SiNWs resulted in an improved signal profile and much less baseline drift in resistance. We attribute this difference to the higher germanium hole mobility as compared to silicon. Additionally, our sensors effectively captured breathing patterns while retaining all their features over time, suggesting their potential as cost-effective and versatile devices for diagnosing respiratory diseases in humans. These SiNWs sensors have the ability to detect risky situations, such as sleep apnea or other breathing-related issues, and can serve as useful healthcare monitoring devices.

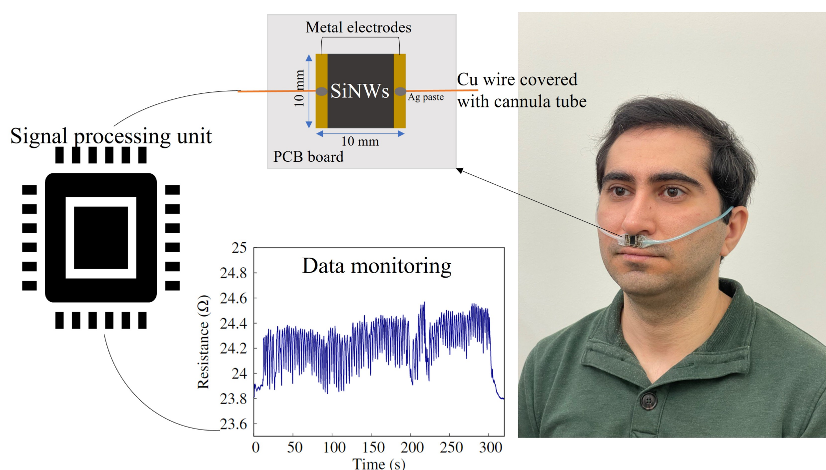

Figure 4.1: Schematic of measurement setup for breath monitoring, the inset graph shows an example of long-term breath monitoring in (NB = normal breathing) mode.

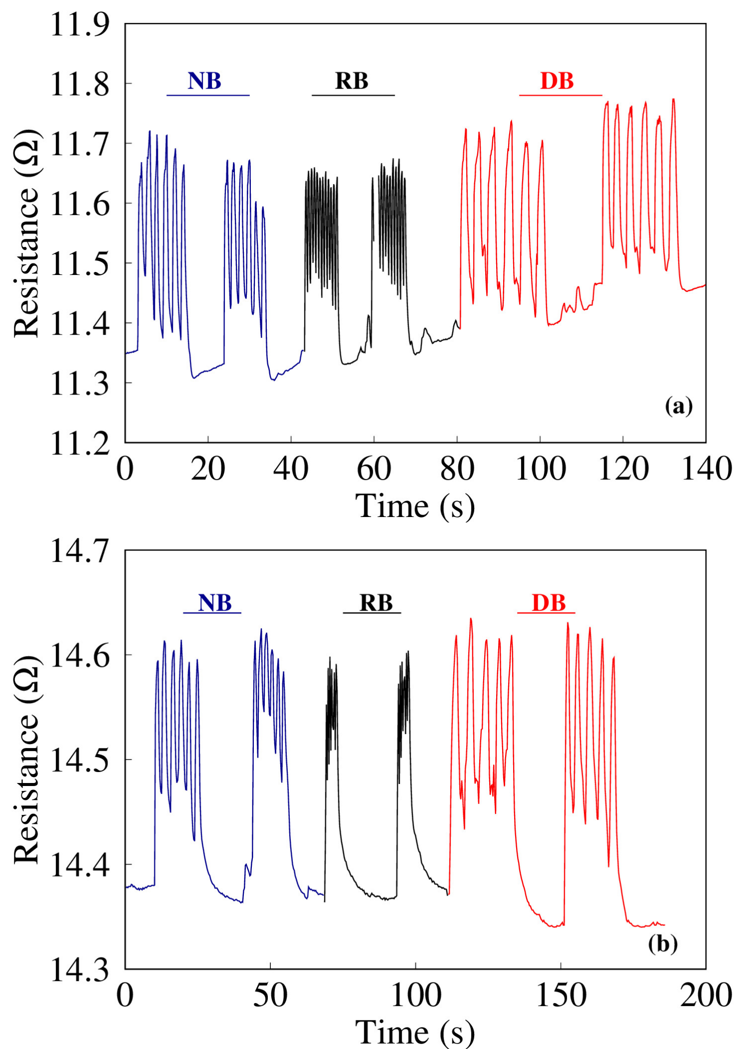

Figure 4.2: Breath sensing test operated in 3 different breathing modes (NB = normal breathing, RB = rapid breathing and DB = deep breathing) for p-type SiNWs with Au electrodes in (a) as-grown state and (b) Ge:SiNWs annealed at 700°C.

Chapter 5

Summary of papers

Papers II, and III discuss the optical, electrical, and structural properties of SiNWs. Papers I and IV discuss the functionality of SiNWs as piezoresistive and bio-sensing devices.

- **Paper I: Piezoresistance characterization of silicon nanowires in uniaxial and isostatic pressure variation**

  The piezoresistance response of SiNWs was analyzed by measuring their electrical resistance variation under applied uniaxial as well as isostatic pressure variation. The PZR coefficient of SiNWs calculated based on uniaxial pressure application resulted in almost two orders of magnitude higher than reported for a single SiNW. In isostatic pressure variation, the electrical resistance of SiNWs measured in a vacuum increased by more than two orders of magnitude.

- **Paper II: Structure and electrical behavior of silicon nanowires prepared by MACE process**

  Structure and electrical characteristics of SiNWs prepared by the MACE method, investigated by SEM and high-resolution X-ray diffraction (HR-XRD) methods. X-ray reciprocal space maps (RSMs) indicated the presence of 0D structural defects rather than extended defects. The I-V characteristics of the nanowires showed a memristive behavior with hysteresis vs applied voltage rates that were used to assess the effect of surface traps on the transport properties of the pristine SiNWs.

- **Paper III: Synthesis and photoluminescence study of silicon nanowires obtained by metal assisted chemical etching**

  The morphology and photoluminescence properties were investigated for SiNWs of different lengths obtained by varying the Ag concentration (as silver nitrate,

$AgNO_3$) and the etching time. The PL spectra revealed that the emission intensity from the SiNWs arrays increased with increasing etching time. This was accompanied by a red-shift in the peak position of approximately 0.09 eV.

- **Paper IV: Germanium coated silicon nanowires as human respiratory sensing device**

  Germanium-coated SiNWs structures were synthesized with MACE method and tested as human respiratory sensors. SiNWs were coated by 50 nm thick Ge film using a magnetron sputtering and post-treated by rapid thermal annealing at 450 and 700C. It was observed that SiNWs coated with Ge and annealed for 5 min at 700C resulted in higher efficiency, faster response, and improved signal profile, and without any baseline drift in the resistance.

Paper I

****

Piezoresistance Characterization of Silicon Nanowires in Uniaxial and Isostatic Pressure Variation

Elham Fakhri [1], Rodica Plugaru [2] , Muhammad Taha Sultan [1,3], Thorsteinn Hanning Kristinsson [1] , Hákon Örn Árnason [1] , Neculai Plugaru [2] , Andrei Manolescu [1] , Snorri Ingvarsson [3] and Halldor Gudfinnur Svavarsson [1]

1 Department of Engineering, Reykjavik University, Menntavegur 1, 102 Reykjavik, Iceland

2 National Institute for Research and Development in Microtechnologies-IMT Bucharest,

077190 Voluntari, Romania

3 Science Institute, University of Iceland, Dunhaga 3, 107 Reykjavik, Iceland

Received: 25 July 2022

Accepted: 18 August 2022

Published: 23 August 2022

Sensors 2022, 22, 6340. https://doi.org/10.3390/s22176340

sensors

MDPI

Communication

Piezoresistance Characterization of Silicon Nanowires in Uniaxial and Isostatic Pressure Variation

Elham Fakhri [1,*], Rodica Plugaru [2], Muhammad Taha Sultan [1,3], Thorsteinn Hanning Kristinsson [1], Hákon Örn Árnason [1], Neculai Plugaru [2], Andrei Manolescu [1], Snorri Ingvarsson [3] and Halldor Gudfinnur Svavarsson [1,*]

1 Department of Engineering, Reykjavik University, Menntavegur 1, 102 Reykjavik, Iceland
2 National Institute for Research and Development in Microtechnologies-IMT Bucharest, 077190 Voluntari, Romania
3 Science Institute, University of Iceland, Dunhaga 3, 107 Reykjavik, Iceland
* Correspondence: elhamf20@ru.is (E.F.); halldorsv@ru.is (H.G.S.)

Abstract: Silicon nanowires (SiNWs) are known to exhibit a large piezoresistance (PZR) effect, making them suitable for various sensing applications. Here, we report the results of a PZR investigation on randomly distributed and interconnected vertical silicon nanowire arrays as a pressure sensor. The samples were produced from p-type (100) Si wafers using a silver catalyzed top-down etching process. The piezoresistance response of these SiNW arrays was analyzed by measuring their I-V characteristics under applied uniaxial as well as isostatic pressure. The interconnected SiNWs exhibit increased mechanical stability in comparison with separated or periodic nanowires. The repeatability of the fabrication process and statistical distribution of measurements were also tested on several samples from different batches. A sensing resolution down to roughly 1 mbar pressure was observed with uniaxial force application, and more than two orders of magnitude resistance variation were determined for isostatic pressure below atmospheric pressure.

Keywords: silicon nanowires; MACE; piezoresistivity

Citation: Fakhri, E.; Plugaru, R.; Sultan, M.T.; Hanning Kristinsson, T.; Örn Árnason, H.; Plugaru, N.; Manolescu, A.; Ingvarsson, S.; Svavarsson, H.G. Piezoresistance Characterization of Silicon Nanowires in Uniaxial and Isostatic Pressure Variation. *Sensors* **2022**, *22*, 6340. https://doi.org/10.3390/s22176340

Academic Editor: Haim Abramovich

Received: 25 July 2022
Accepted: 18 August 2022
Published: 23 August 2022

Publisher's Note: MDPI stays neutral with regard to jurisdictional claims in published maps and institutional affiliations.

Copyright: © 2022 by the authors. Licensee MDPI, Basel, Switzerland. This article is an open access article distributed under the terms and conditions of the Creative Commons Attribution (CC BY) license (https://creativecommons.org/licenses/by/4.0/).

1. Introduction

Low-dimensional structures may possess unique mechanical, electrical, optical, and thermoelectric properties. Particularly, silicon nanowires (SiNWs) have demonstrated properties suitable for various advanced applications [1–3], including low-cost thermoelectric devices and chemo-biological sensors with ultrahigh sensitivity [4,5]. The integration of SiNWs in electronic devices is favoured by their compatibility with the well-established $Si\text{-}SiO_2$ electronic industrial technology. Bulk silicon has been known for a while to exhibit high piezo resistance (PZR) effect [6]. In bulk semiconductors, the PZR-effect takes place, in principle, due to a change in the electronic structure and modification of the charge-carriers effective masses. This phenomenon has found practical applications in many Si-based devices, such as pressure transducers [7], cantilevers for atomic force microscopy [8], accelerometers [9], biosensors [10], and multi-axis force sensing tools [11].

Recently, nanowires have been shown to possess the ability to significantly increase the PZR response [12]. A giant PZR was observed in p-doped SiNWs with diameters of 50 nm to 350 nm and a length of microns initially under tensile uniaxial stress [13]. However, the PZR effect in n-doped nanowires was found to be comparable to that in the bulk counterpart, both for tensile and compressive uniaxial stress [14].

On the theoretical side, the origin of the PZR effect in SiNWs has long been under debate, and most frequently, it is referred to as anomalous PZR [15]. It has been related to quantum confinement effects [16], surface charge effects [17–19], strain-induced bandgap shift [20], or changes in the charge carrier's effective masses [21]. A complex model

incorporating these mechanisms has been proposed in order to analytically quantify the PZR effect in silicon [22].

A survey of several PZR sensors based on SiNWs, e.g., cantilever [23], opto-mechanical sensor [24], flexible pressure sensor [18], or breath detector [19], shows that different methods have been used for fabricating the SiNWs, such as vapor-liquid-solid (VLS), laser ablation, and metal-assisted catalyzed etching (MACE) [25]. Among these methods, MACE is the simplest and most versatile one [26]. It relies on catalyzed etching with assistance from a perforated metal template film (typically gold or silver) [27] or randomly distributed metallic nanoparticles (typically gold or silver) [28,29] spread on the Si-wafer. To date, studies have been focused on using different gas types to apply direct pressure on SiNWs, either single SiNW or arrays of SiNWs [19,30], and have neglected the SiNWs response under isostatic pressure, which creates a load uniformly distributed on the sample surface. Here, we report on the PZR effect in SiNWs obtained by MACE under uniaxial compression load as well as isostatic pressure in a vacuum chamber. We find that the interconnected SiNWs are mechanically stronger and functionally more stable compared with the arrays of separated wires under applied uniaxial pressure. They show higher PZR sensitivity under isostatic pressure variation. We also demonstrate a simple, low-cost, and reproducible fabrication method for a robust and sensitive pressure sensor.

2. Materials and Methods

2.1. Fabrication of SiNWs

Arrays of interconnected SiNWs were fabricated by silver (Ag) MACE in a three-step process, from p-type, single-side polished 525 µm-thick Si wafers, with resistivity, ρ, of 10 Ω cm to 20 Ω cm. The nanowire patterns were made on areas of about 1 cm^2 on the polished side of the wafers. The sequence of steps used to prepare the SiNW areas is as follows:

1. Deposition of metal catalyst: Ag nanoparticles were deposited on the surface of the Si wafers by immersing the wafers in a solution of 3 M HF and 1.5 M $AgNO_3$ for 60 s.
2. Wire etching: The samples were etched by immersing them in HF:H_2O_2 (5M:0.4M) solution to obtain vertically aligned SiNWs.
3. Removal of residual Ag nanoparticles: Samples were immersed in 20% *w/v* HNO_3 to remove residual silver particles. A more detailed description can be found in Refs. [28,29].

Subsequently, 150 nm-thick aluminum electrodes were deposited on the samples by electron beam evaporation (Polyteknik Cryofox Explorer 600 LT). For the uniaxial measurements, the electrodes were deposited on the top and backside of the samples, while for the isostatic pressure measurements, the electrodes were made co-planar.

Four sets of interconnected SiNWs samples, denoted as follows, were prepared by varying the etching time: A (1 min), B (3 min), C (5 min), and D (7 min) were made for uniaxial pressure application, and sample E (40 min) was made for isostatic pressure testing.

Additionally, periodic SiNWs, such as sample F, were made as described in the Supplementary Material. Table 1 shows the list of the samples with corresponding etching times and length.

A scanning electron microscope (SEM, Zeiss Supra 35) was used to characterize the SiNW's geometry. Top and cross-sectional SEM images were used to estimate the average diameter of the wires. The Gwyddion software for data visualization and analysis was applied to surface SEM images in order to estimate the total top area of the wires. Figure 1 shows (a,b) the cross-section of the wire array and (c) the surface area of SiNWs obtained after 7 min etching. It is worth mentioning here that the SEM analysis was carried out on the sample prior to the removal of Ag nanoparticles, which are visualized as bright spots at the base of the nanowires in the cross-section.

Table 1. List of samples with different etching times and corresponding lengths. Samples A, B, C, D, and E are random wires, and sample F is with periodic wires (shown in the Supplementary Material).

Sample	Etching Time (min)	SiNW Length (µm)
A	1	0.7
B	3	1.5
C	5	2.2
D	7	3
E	40	10
F	5	0.65

As can be seen in the top-view image, the wires are partly interconnected, forming a continuous rigid structure. Further, also seen from place to place are free-standing nanowires forming bundles. Such bundle formation may take place because of capillary forces acting during the drying process following the wet-etching step. In the cross-sectional image, one may observe that the length of the wires is relatively homogeneous, around 3 µm, and their typical diameter is approximately 150 nm. According to Peng et al. [5], porosity plays an essential role in the PZR response, which increases with increased porosity. The porosity is most conveniently controlled by the concentration of Ag deposition solution and etching time. In a previous study [28], it was demonstrated that the SiNWs porosity was highly affected by the concentration of the $AgNO_3$ during the Ag deposition. A 1.5 mM $AgNO_3$ (as used for samples A–D) provided highly porous SiNWs with maximum photoluminescence spectra intensity.

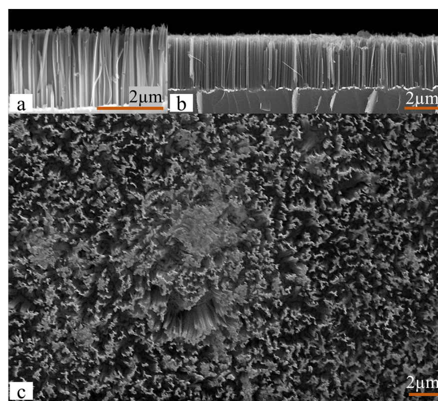

Figure 1. SEM image of SiNWs etched for 7 min (**a**), high-magnification cross-section of the same image (**b**), and (**c**) top-view SEM image of SiNWs etched for 7 min.

From the SEM image analysis, the wire's cross-sectional surface coverage was estimated at roughly 28% by using the Gwyddion program, Figure 2. By counting the average number of wires on several line scans, the wire density was estimated to be 1.6×10^7 mm^2, which corresponds to roughly 8×10^8 wires under the force meter area (7 × 7 mm).

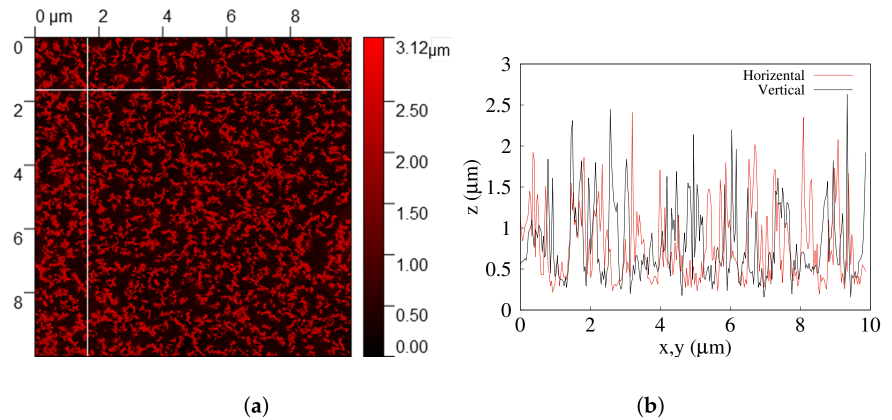

Figure 2. (**a**) Gwyddion analysis of top-view SEM image in (100 µm^2). (**b**) Two Gwyddion line-scans of the figure to the left (red color—horizontal axis, black color—vertical axis).

2.2. Measurement Setups

For uniaxial PZR tests, the samples were clamped between a metal pin of a force meter (Mark-10, M5-012), touching the top side of the samples, and a rigid copper (Cu) plate at the backside, as shown in Figure 3. In order to improve the electrical contacts, the samples were glued to the Cu backside plate with silver paste. The force meter was mounted on a vertical rod allowing for movement on the *z*-axis (vertical) by a manually adjusted screw. Uniaxial pressure was applied to the samples by pressing the pin of the force meter into the samples' surface with an intensity determined by the aforementioned screw. The applied force was in the range of 100 mN to 900 mN on an area of 7 × 7 mm (the cross-sectional area of the pin). Taking the wire coverage (28 %) into account, this corresponds to a gauge pressure of 7 kPa to 66 kPa. Figure 3 shows a sketch of the experimental setup. A Keithley 2400 SourceMeter was used to measure the resistance *R* through the sample as a function of applied pressure at a constant bias voltage of 2 V.

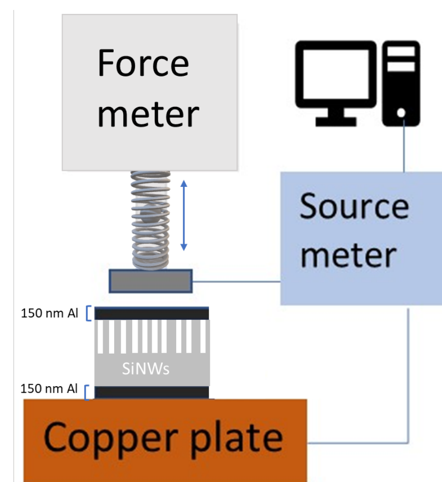

Figure 3. Schematic of the force meter setup for testing PZR characteristics.

For PZR tests under isostatic pressure variation, a vacuum chamber was used, and the air was removed while the resistance was measured at a fixed 5 V. In this case (for sample E), the contacts were made in co-planar configuration, with separate contacts on each side

of the patterned area, such that the nanowires are maximally exposed to air instead of top-and-bottom contacts as for the uniaxial measurements (performed with samples A–D). Furthermore, the wire length was increased (to 10 µm) to increase the surface area exposed to the air. The samples were mounted on a fixed sample station inside the chamber with tungsten needle tip kelvin probes as a connection.

3. Results

3.1. Electrical Response under Uniaxial Force

A maximum force of approximately 900 mN was applied to the samples using the setup shown in Figure 3. The maximum vertical force exerted on each wire thus corresponds to $900 \times 10^{-3}\,\mathrm{N}/8 \times 10^{8} \approx 1.1 \times 10^{-9}\,\mathrm{N/wire}$ or 6.6×10^{4} Pa (0.65 bar).

The force and the instantaneous resistance measured after applying the force to the sample with nanowires of length 3 µm (etched for 7 min) are shown in Figure 4a as a function of time. The maximum force was applied at the beginning (time zero) and then reduced step-wise while the resistance was being measured. Each force level was kept constant for roughly 50 s to confirm that the resistance value was stable with time. As clearly visible, the resistance changes significantly and inversely with pressure.

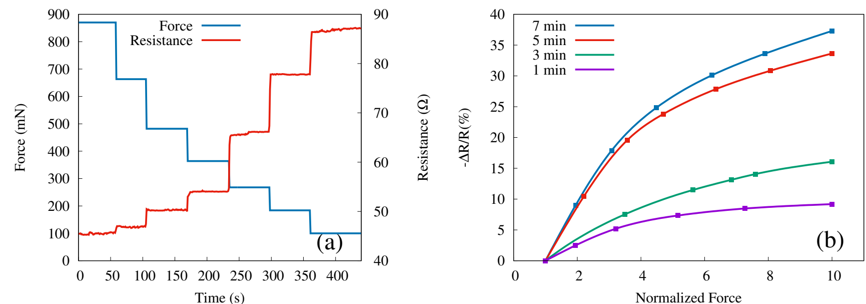

Figure 4. (**a**) Instantaneous resistance (right y-axis, red line) in response to applied force (left 4-axis, blue line) over time for sample D. (**b**) Relative resistance change versus normalized force for SiNWs samples A (purple), B (green), C (red), and D (blue).

We define the relative resistance change vs. force variation for each step $k = 1, 2, \ldots$ as

$$\frac{\Delta R}{R} = \frac{R_k - R_1}{R_1}, \tag{1}$$

where R_k is the average resistance obtained for the constant force step k. The measurements were repeated four times on each sample (A, B, C, D), each time reproducing the force steps as well as possible with the adjustable screw. A second average, this time of the relative resistance in step k, defined by Equation (1), obtained for the four measurements vs. the average normalized forces for each step, is presented in Figure 4b. Here, by normalized force, we mean the ratio of the force in a particular step k to the initial force, F_k/F_1. Hence, the maximum force values for each step-wise measurement are normalized to unity. Note that the resistance decreases when the force increases and that in Figure 4b, we show the negative of $\Delta R/R$.

Increasing the length of the nanowires (by increasing the etching time) leads to higher relative resistance, although the trend appears to saturate; only a relatively small difference between the 5 min and 7 min samples has been obtained. The highest relative change (37.3%) in resistance is observed for the longest etching time (sample D) with regards to uniaxial pressure.

In Figure 5, the resistance versus applied force is shown again for sample D (blue line), now compared with the case of the bulk Si (red line). For this measurement, we replicated sample D four times, in the same conditions of a 7 min etching time, and performed the

measurements on each sample replica. These measurements have been performed to test the repeatability of the sensor's response in the same conditions as have been performed in Figure 4a. It is worth noting that the un-uniform step size observed in Figure 4a is due to the manually adjustable screw of the force meter shown in the schematic. The data displayed are average values measured on these samples (D-like), shown with the error bars. A striking difference between these two configurations (SiNWs vs. bulk Si) is observed. No measurable change in resistance is seen for the bulk Si, in very sharp contrast to the SiNWs sample.

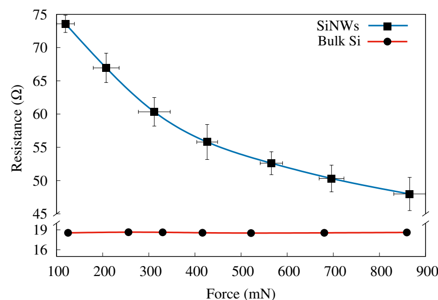

Figure 5. Resistance vs. applied force for the D-like samples (blue line) and bulk-Si (red line). Data for SiNWs are average values of four distinct samples; the error bars show the range in which the measurements fell.

Up to a 35 % change in resistivity was observed over the pressure variation in the range of 0.1 N to 0.9 N. In order to test the stability of SiNW's PZR response and response time, we performed several sets of measurements over different samples. In this stability test, the resistance shift was measured in periods of 60 s of loading and unloading force for all the samples. All samples were loaded by 860(10) mN and then unloaded to 220(10) mN. We observe a fast response (below 0.5 s), good stability, and high sensitivity to repeated pressure changes. The results of a reproducibility test for sample D are presented in Figure 6.

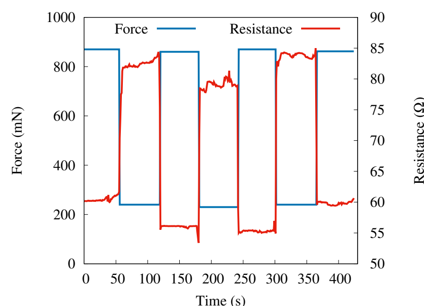

Figure 6. SiNWs PZR response due to repeated load–unload forces in real time for sample D.

Hydrogenation (exposure to hydrogen plasma) is widely used in the electronic industry to increase the mobility of charge carriers in semiconductors. It neutralizes deep and shallow defects and charged surface states [31,32]. Because the PZR effect has been attributed to surface states, we applied a hydrogenation treatment in order to explore the origin of the PZR effect in SiNWs. For hydrogen plasma treatment, we used a custom-built inductively coupled discharge setup with cylindrical geometry (290 mm long quartz tube with a diameter of 34 mm). The quartz tube was held inside a circular copper inductive coil with a diameter of 54 mm. A radio-frequency power generator CERSAR (c) (13.56 MHz) source coupled with an impedance-matching unit was utilized. For hydrogenation, a gas

mixture of Ar/H_2 (30 / −70%) was used, and the throttle valves were adjusted to stabilize the gas pressure of 29 mbar. A more detailed description and schematic of the hydrogenation setup can be found elsewhere [33,34]. In Figure 7, we compare the behavior of sample D before and after the hydrogenation. The PZR effect decreases dramatically and can be attributed to the passivation of the surface states [35].

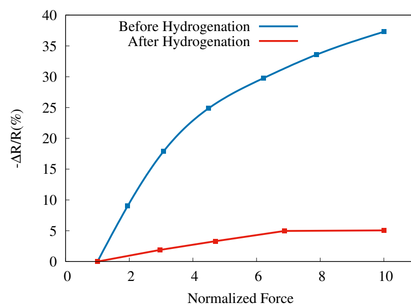

Figure 7. SiNWs PZR response for sample D before and after hydrogenation.

3.2. Electrical Response under Isostatic Pressure

Sample E (10 µm) was used for the investigation of the PZR response to isostatic pressure in a vacuum chamber. The PZR response was tested in the chamber under re-pressurizing conditions in the range of 10^{-4} mbar to 10^{3} mbar. The results are shown in Figure 8, where the resistance is plotted as a function of the pressure measured at a fixed bias voltage of 5 V. We observed a dramatic increase in the resistance by more than two orders of magnitude when pumping the air out of the vacuum chamber. We believe this is a result of combined mechanical and chemical effects: the pressure drop removes mechanical stress, and the lack of air and humidity suppresses the chemisorption. Note that the resistance values for sample E are much higher than for samples A–D because of the co-planar configuration of the contacts and also because of the larger length of the nanowires.

In the Supplementary Material we show, for comparison, the behavior of periodic arrays of SiNWs with increasing isostatic pressure.

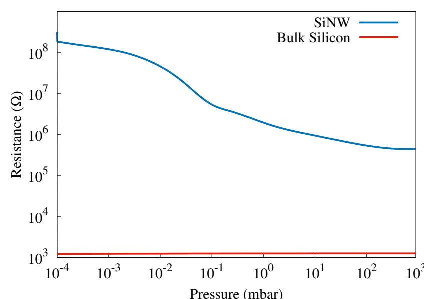

Figure 8. The resistance of sample E (on a log 10 scale) as a function of pressure measured in the vacuum chamber is shown with the blue curve. For comparison, in red, the resistance of a bulk silicon sample (i.e., without nanowires).

4. Discussion

For solid materials, the inter-atomic spacing may be altered by strain. Consequently, apart from geometric changes in semiconductors, bandstructure-related details, such as bandgap or effective mass, may change, and thereby the resistivity may change as well. An applied strain changes the bandgap and the effective mass of charge carriers, which, in

turn, affect the carrier concentration as well as their mobility [36]. Within a certain range of strain, this relationship is linear [22,37]. Niquet et al. [36] show that electron mobility saturates with strain. Subsequently, the PZR response saturates above a certain range of strain. When a uniaxial stress X is applied, the piezoresistance coefficient of the resistivity ρ in the direction of stress is defined as

$$\pi_l = \frac{\Delta\rho}{\rho_0}\frac{1}{X}, \tag{2}$$

where $\Delta\rho$ is the stress-induced change in the resistivity and ρ_0 is the reference resistivity of the unstressed material.

In our case, a uniaxial compressive force F was applied to SiNWs along their length by a force meter. The stress is $X = F/A_t$, A_t being the total cross-sectional area of the nanowires, which is equal to pA_m, where A_m is the cross-sectional area of the pin pressed into the wires, and p is the relative cross-sectional area of the wires. Assuming the electrical resistivity of the nanowires is proportional to their resistance, Equation (2) becomes

$$\pi_l = \frac{pA_m}{F} \times \frac{\Delta R}{R_0}. \tag{3}$$

The structure of our SiNWs array is robust and stable as the wires are partially interconnected, which provides high structural strength. Such stability and fast response of SiNWs is a desired property for many devices, such as solid-state accelerometers and bipolar transistors [38]. Further, our results are in agreement with the study of Ghosh et al. [19], in which large-diameter Si nanorod-based sensors were used for force detection.

He et al. [13], who measured PZR coefficients of single (p-doped) SiNWs, with diameters 50 nm to 300 nm, made from wafers with resistivities of 0.003 Ω cm to 10 Ω cm, found that the PZR was roughly inversely proportional to the diameter and proportional to the wafer resistivity. For a similar diameter and wafer resistivity as in our present work, ~150 nm and 10 Ω cm, respectively, the PZR coefficient π_l for a single wire was of the order 10^{-7} Pa^{-1}. (According to Figure 2d of Ref. [13]). Using Equation (3), with $p = 0.28$, $A_m = 49$ mm^2, $F = 0.8$ N, and $\Delta R/R = 0.35$, we obtain $\pi_l \approx 6 \times 10^{-6}$ Pa^{-1}, i.e., almost two orders of magnitude higher. Note that, in principle, Equation (2) does not depend on sample details, such as the number of nanowires or their configuration, which we believe plays a role in our case. Therefore, we attribute this higher value to a collective PZR effect brought about by the interaction between multiple and interconnected wires rather than the response of a single nanowire. Additionally, the pressure sensitivity of the sensor in the isostatic pressure variation given by $S = \frac{\Delta R}{R}/\Delta P$ [39], in the pressure range of 10^{-4} to 10^3 mbar, is 9.98×10^{-6} Pa^{-1}. It is also seen that the highest sensitivity (highest slope in Figure 8) is found in the pressure range of roughly 10^{-2} and 10^{-1} mbar where the sensitivity measure is 8.8×10^{-3} Pa^{-1}.

5. Conclusions

In summary, large arrays of interconnected SiNWs were fabricated in a simple three-step wet chemical process and used for testing the piezoresistance effect in nanowires. The interconnected structures of the SiNWs provide a great increase in mechanical stability. A pressure change of 100 Pa could be measured with this robust device. The calculated PZR coefficient based on SiNWs array with NWs length of 3 µm as resulted after MACE etching for 7 min, sample D, was almost two orders of magnitude higher for our sensor than reported for a single SiNW. Repeated measurements for different samples fabricated with the same process demonstrated good reproducibility with less than 5% deviation in pressure sensing. The electrical resistance of SiNWs of 10 µm length increased more than two orders of magnitude when measured in a vacuum. These findings make the device based on random and interconnected SiNWs a strong candidate as a simple and inexpensive alternative to various pressure-sensing applications.

Supplementary Materials: The following supporting information can be downloaded at: https://www.mdpi.com/article/10.3390/s22176340/s1, Figure S1: Cross-sectional SEM micrographs of periodic SiNWs-ZnO array with wire length of 650 nm, inset shows the top view image; Figure S2: (a) I-V characteristics for direct bias of the 650 nm periodic SiNWs, with applied pressure in the range 0.5–3.5 MPa. The blue curve corresponds to atmospheric pressure. (b) Variation of $\Delta R/R_0$ with applied pressure for a fixed direct bias of 2 V.

Author Contributions: Conceptualization, R.P.; Funding acquisition, H.G.S.; Investigation, E.F., M.T.S., T.H.K. and H.Ö.Á.; Methodology, E.F., M.T.S. and H.G.S.; Project administration, R.P., N.P., A.M. and H.G.S.; Supervision, R.P., N.P., A.M., S.I. and H.G.S.; Visualization, H.G.S.; Writing—original draft, E.F.; Writing—review & editing, M.T.S., A.M., S.I. and H.G.S. All authors have read and agreed to the published version of the manuscript.

Funding: This work was supported by Reykjavik University Ph.D. fund No. 220006, and funding from the Icelandic Research Fund Grant No. 218029-051. RP acknowledges support from the Romanian Core Program Contract No.14 N/2019 Ministry of Research, Innovation, and Digitalization.

Institutional Review Board Statement: Not applicable.

Informed Consent Statement: Not applicable.

Data Availability Statement: Not applicable.

Conflicts of Interest: The authors declare no conflict of interest.

References

1. Peng, K.Q.; Wang, X.; Li, L.; Hu, Y.; Lee, S.T. Silicon nanowires for advanced energy conversion and storage. *Nano Today* **2013**, *8*, 75–97. [CrossRef]
2. Heris, H.R.; Kateb, M.; Erlingsson, S.I.; Manolescu, A. Thermoelectric properties of tubular nanowires in the presence of a transverse magnetic field. *Nanotechnology* **2020**, *31*, 424006. [CrossRef] [PubMed]
3. Heris, H.R.; Kateb, M.; Erlingsson, S.I.; Manolescu, A. Effects of transverse geometry on the thermal conductivity of Si and Ge nanowires. *Surf. Interfaces* **2022**, *30*, 101834. [CrossRef]
4. Zhou, X.; Hu, J.; Li, C.; Ma, D.; Lee, C.; Lee, S. Silicon nanowires as chemical sensors. *Chem. Phys. Lett.* **2003**, *369*, 220–224. [CrossRef]
5. Peng, K.Q.; Wang, X.; Lee, S.T. Gas sensing properties of single crystalline porous silicon nanowires. *Appl. Phys. Lett.* **2009**, *95*, 243112. [CrossRef]
6. Smith, C.S. Piezoresistance effect in germanium and silicon. *Phys. Rev.* **1954**, *94*, 42–49. [CrossRef]
7. Tufte, O.N.; Chapman, P.D.; Long, D. Silicon diffused-element piezoresistive diaphragms. *J. Appl. Phys.* **1962**, *33*, 3322–3327. [CrossRef]
8. Tortonese, M.; Barrett, R.C.; Quate, C.F. Atomic resolution with an atomic force microscope using piezoresistive detection. *Appl. Phys. Lett.* **1993**, *62*, 834. [CrossRef]
9. Ning, Y.; Loke, Y.; McKinnon, G. Fabrication and characterization of high g-force, silicon piezoresistive accelerometers. *Sens. Actuators A Phys.* **1995**, *48*, 55–61. [CrossRef]
10. Wee, K.; Kang, G.; Park, J.; Kang, J.; Yoon, D.; Park, J.; Kim, T. Novel electrical detection of label-free disease marker proteins using piezoresistive self-sensing micro-cantilevers. *Biosens. Bioelectron.* **2005**, *20*, 1932–1938. [CrossRef]
11. Tiwari, B.; Billot, M.; Clévy, C.; Agnus, J.; Piat, E.; Lutz, P. A two-axis piezoresistive force sensing tool for microgripping. *Sensors* **2021**, *21*, 6059. [CrossRef] [PubMed]
12. Dorda, G. Piezoresistance in quantized conduction bands in silicon inversion layers. *J. Appl. Phys.* **1971**, *42*, 2053–2060. [CrossRef]
13. He, R.; Yang, P. Giant piezoresistance effect in silicon nanowires. *Nat. Nanotechnol.* **2006**, *1*, 42–46. [CrossRef] [PubMed]
14. Gao, D.; Yang, Z.; Zheng, L.; Kun, Z. Piezoresistive effect of n-type <111> -oriented Si nanowires under large tension/compression. *Nanotechnology* **2017**, *28*, 095702. [PubMed]
15. Zhang, S.; Lou, L.; Lee, C. Piezoresistive silicon nanowire based nanoelectromechanical system cantilever air flow sensor. *Appl. Phys. Lett.* **2012**, *100*, 023111. [CrossRef]
16. Cheng, W.; Yu, L.; Kong, D.; Yu, Z.; Wang, H.; Ma, Z.; Wang, Y.; Wang, J.; Pan, L.; Shi, Y. Fast-response and low-hysteresis flexible pressure sensor based on silicon nanowires. *IEEE Electron Device Lett.* **2018**, *39*, 1069–1072. [CrossRef]
17. Nguyen, T.D.; Lee, J.S. Recent Development of Flexible Tactile Sensors and Their Applications. *Sensors* **2021**, *22*, 50. [CrossRef]
18. Kim, C.; Ahn, H.; Ji, T. Flexible Pressure Sensors Based on Silicon Nanowire Array Built by Metal-Assisted Chemical Etching. *IEEE Electron Device Lett.* **2020**, *41*, 1233–1236. [CrossRef]
19. Ghosh, R.; Song, M.S.; Park, J.; Tchoe, Y.; Guha, P.; Lee, W.; Lim, Y.; Kim, B.; Kim, S.W.; Kim, M.; et al. Fabrication of piezoresistive Si nanorod-based pressure sensor arrays: A promising candidate for portable breath monitoring devices. *Nano Energy* **2021**, *80*, 105537. [CrossRef]

20. Shiri, D.; Kong, Y.; Buin, A.; Anantram, M.P. Strain induced change of bandgap and effective mass in silicon nanowires. *Appl. Phys. Lett.* **2008**, *93*, 07314. [CrossRef]
21. Zhang, J.; Zhao, Y.; Ge, Y.; Li, M.; Yang, L.; Mao, X. Design optimization and fabrication of high-sensitivity SOI pressure sensors with high signal-to-noise ratios based on silicon nanowire piezoresistors. *Micromachines* **2016**, *7*, 187. [CrossRef] [PubMed]
22. Rowe, A. Piezoresistance in silicon and its nanostructures. *J. Mater. Res.* **2014**, *29*, 731–744. [CrossRef]
23. Toriyama, T.; Tanimoto, Y.; Sugiyama, S. Single crystal silicon nano-wire piezoresistors for mechanical sensors. *J. Microelectromechanical Syst.* **2002**, *11*, 605–611. [CrossRef]
24. Toriyama, T.; Sugiyama, S. Single crystal silicon piezoresistive nano-wire bridge. *Sens. Actuators A Phys.* **2003**, *108*, 244–249. [CrossRef]
25. Schmidt, V.; Wittemann, J.V.; Senz, S.; Gösele, U. Silicon nanowires: A review on aspects of their growth and their electrical properties. *Adv. Mater.* **2009**, *21*, 2681–2702. [CrossRef]
26. Shi, D.; Chen, Y.; Li, Z.; Dong, S.; Li, L.; Hou, M.; Liu, H.; Zhao, S.; Chen, X.; Wong, C.P.; et al. Anisotropic Charge Transport Enabling High-Throughput and High-Aspect-Ratio Wet Etching of Silicon Carbide. *Small Methods* **2022**, 6, 2200329. [CrossRef]
27. Svavarsson H.G.; Hallgrimsson, B.H.; Niraula, M.; Lee K.J.; Magnusson, R. Large arrays of ultra-high aspect ratio periodic silicon nanowires obtained via top-down route. *Appl. Phys. A-Mater. Sci. Process.* **2016**, *122*, 1–6. [CrossRef]
28. Fakhri, E.; Sultan, M.; Manolescu, A.; Ingvarsson, S.; Plugaru, N.; Plugaru, R.; Svavarsson, H. Synthesis and photoluminescence study of silicon nanowires obtained by metal assisted chemical etching. In Proceedings of the 2021 International Semiconductor Conference (CAS), Sinaia, Romania, 6–8 October 2021; pp. 147–150.
29. Plugaru, R.; Fakhri, E.; Romanitan, C.; Mihalache, I.; Craciun, G.; Plugaru, N.; Árnason, H.O.; Sultan, M.T.; Nemnes, G.A.; Ingvarsson, S.; et al. Structure and electrical behavior of silicon nanowires prepared by MACE process. *arXiv* **2022**, arXiv:2206.05006
30. Neuzil, P.; Wong, C.C.; Reboud, J. Electrically controlled giant piezoresistance in silicon nanowires. *Nano Lett.* **2010**, *10*, 1248–1252. [CrossRef]
31. Danielsson, D.; Gudmundsson, J.; Svavarsson, H. Effect of hydrogenation on minority carrier lifetime in low-grade silicon. *Phys. Scr.* **2010**, *2010*, 014005. [CrossRef]
32. Svavarsson, H.G.; Sultan, M.T.; Lee, K.J.; Magnusson, R. Hydrogenated silicon films for low-loss resonant reflectors operating in the visible region. In Proceedings of the 2020 IEEE Research and Applications of Photonics, Miramar Beach, FL, USA, 10–12 August 2020; pp. 1–2.
33. Sultan, M.; Gudmundsson, J.T.; Manolescu, A.; Stoica, T.; Ciurea, M.; Svavarsson, H. Enhanced photoconductivity of embedded SiGe nanoparticles by hydrogenation. *Appl. Surf. Sci.* **2019**, *479*, 403–409. [CrossRef]
34. Sultan, M.; Gudmundsson, J.T.; Manolescu, A.; Ciurea, M.; Svavarsson, H. The Effect of H 2/Ar Plasma Treatment Over Photoconductivity of Sige Nanoparticles Sandwiched Between Silicon Oxide Matrix. In Proceedings of the 2018 International Semiconductor Conference (CAS), Sinaia, Romania, 10–12 October 2018; pp. 257–260.
35. Song, L.; Yang, D.; Yu, X. Investigation on the impact of hydrogen on the passivation of silicon surface states in clean and copper contaminated conditions. *AIP Adv.* **2019**, *9*, 105102. [CrossRef]
36. Niquet, Y.M.; Delerue, C.; Krzeminski, C. Effects of strain on the carrier mobility in silicon nanowires. *Nano Lett.* **2012**, *12*, 3545–3550. [CrossRef]
37. Matsuda, K.; Suzuki, K.; Yamamura, K.; Kanda, Y. Nonlinear piezoresistance effects in silicon. *J. Appl. Phys.* **1993**, *73*, 1838–1847. [CrossRef]
38. Doll, J.C.; Pruitt, B.L. *Piezoresistor Design and Applications*; Springer: Berlin, Germany, 2013.
39. Pataniya, P.M.; Bhakhar, S.A.; Tannarana, M.; Zankat, C.; Patel, V.; Solanki, G.; Patel, K.; Jha, P.K.; Late, D.J.; Sumesh, C. Highly sensitive and flexible pressure sensor based on two-dimensional MoSe2 nanosheets for online wrist pulse monitoring. *J. Colloid Interface Sci.* **2021**, *584*, 495–504. [CrossRef] [PubMed]

Paper II

****

Structure and electrical behavior of silicon nanowires prepared by MACE process

R. Plugaru [1,a], E. Fakhri *,[1,b], C. Romanitan [a], I. Mihalache [a], G. Craciun [a], N. Plugaru [a], H.O. Arnason [b], M.T. Sultan [c], G.A. Nemnes [d,e], S. Ingvarsson [c], H.G. Svavarsson [b], A. Manolescu [b]

a National Institute for Research and Development in Microtechnologies- IMT Bucharest, Voluntari 077190, Romania

b Department of Engineering, Reykjavik University, Menntavegur 1, Reykjavik IS-102, Iceland

c Science Institute, University of Iceland, Dunhaga 3, Reykjavik IS-107, Iceland d Horia Hulubei National Institute for Physics and Nuclear Engineering, Magurele-Ilfov 077126, Romania

e University of Bucharest, Department of Physics, Magurele-Ilfov 077125, Romania

Received 1 April 2022

Received in revised form 9 June 2022

Accepted 26 June 2022

Surfaces and Interfaces 33 (2022) 102167

Surfaces and Interfaces 33 (2022) 102167

Contents lists available at ScienceDirect

Surfaces and Interfaces

journal homepage: www.sciencedirect.com/journal/surfaces-and-interfaces

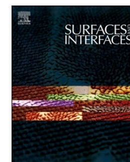

Structure and electrical behavior of silicon nanowires prepared by MACE process

R. Plugaru [1,a], E. Fakhri [*,1,b], C. Romanitan [a], I. Mihalache [a], G. Craciun [a], N. Plugaru [a], H.O. Arnason [b], M.T. Sultan [c], G.A. Nemnes [d,e], S. Ingvarsson [c], H.G. Svavarsson [b], A. Manolescu [b]

[a] National Institute for Research and Development in Microtechnologies- IMT Bucharest, Voluntari 077190, Romania
[b] Department of Engineering, Reykjavik University, Menntavegur 1, Reykjavik IS-102, Iceland
[c] Science Institute, University of Iceland, Dunhaga 3, Reykjavik IS-107, Iceland
[d] Horia Hulubei National Institute for Physics and Nuclear Engineering, Magurele-Ilfov 077126, Romania
[e] University of Bucharest, Department of Physics, Magurele-Ilfov 077125, Romania

ARTICLE INFO

Keywords:
Silicon nanowire arrays
MACE
X-ray reciprocal space maps
Surface trap states
I-V hysteresis

ABSTRACT

We report on the structure and electrical characteristics of silicon nanowire arrays prepared by metal assisted chemical etching (MACE) method, investigated by cross-sectional scanning electron microscopy (SEM) and high resolution X-ray diffraction (HR-XRD) methods. SEM micrographs show arrays of merged parallel nanowires, with lengths of 700 nm and 1000 nm, resulted after 1.5 min and 5 min etching time, respectively. X-ray reciprocal space maps (RSMs) around Si (004) reciprocal lattice point indicate the presence of 0D structural defects rather than of extended defects. The photoluminescence spectra exhibit emission bands at 1.70 eV and 1.61 eV, with intensity significantly higher in the case of longer wires and associated with the more defected surface. The transient photoluminescence spectroscopy reveals average lifetime of 60 ôs and 111 ôs for the two SiNW arrays, which correlate with a larger density of defects states in the latest case. The I-V characteristics of the nanowires, show a memristive behavior with the applied voltage sweep rate in the range 5–0.32V/s. We attribute this behavior to trap states which control the carrier concentration, and model this effect using an equivalent circuit. Photogeneration processes under excitation wavelengths in visible domain, 405 nm - 650 nm, and under light intensity in the range 20–100 mW/cm^2 provided a further insight into the trap states.

1. Introduction

Silicon nanowire (SiNW) arrays with controlled morphology (porosity, length, orientation) have been efficiently prepared by metal assisted chemical etching (MACE) processing [1–3], aiming to widen their applicability to performant light emitting devices, photodetectors, energy storage and conversion, or sensors [4–6]. Yet, defective surfaces of SiNWs resulting from chemical-assisted preparation processes can affect the electric parameters of the devices [7,8].

The dynamic hysteresis of the electrical characteristics of a nanoelectronic device when the applied voltage changes in time is one of the first indications of the presence of a charge trapping mechanism inside the devices with a relaxation time comparable to the time of the voltage variation. This phenomenon is used in memristive device, often based on metallic nanowires [9], but also on silicon nanowires [10,11]. Sensing devices based on SiNWs have also been proposed, where the dynamic occupation of the nanowire surface states created by the external charges from the adsorbed biomolecules modify the hysteresis loop [12]. Or field effect transistors where the nanowires are in contact with a dielectric, or polymer [13].

The electrical hysteresis is also present in solar cells based on perovskite materials, and associated to the degradation of the cell, due to ionic migration, charge accumulation at interfaces, and their influence on the photogenerated current [14–16]. Apart of the possible hysteretic effects, the surface states of SiNWs are also important for the characteristics of nanostructured solar cells, where the electrons trapped by surface states can act as a gate bias that enhances the photoconductivity [17–19].

In this work we report on the electrical response of Al/SiNWs/Al device structures with pristine SiNW arrays prepared by the MACE

* Corresponding author.
E-mail addresses: rodica.plugaru@imt.ro (R. Plugaru), elhamf20@ru.is (E. Fakhri).
[1] These authors contributed equally to this work.

https://doi.org/10.1016/j.surfin.2022.102167
Received 1 April 2022; Received in revised form 9 June 2022; Accepted 26 June 2022
Available online 8 July 2022
2468-0230/© 2022 Elsevier B.V. All rights reserved.

method. The nanowires are highly imperfect and in lateral contact to each other, forming a system of inter-connected wires rather than independent wires. The current-voltage (I-V) and capacitance-voltage (C-V) curves, measured in dark and under various illumination conditions in terms of wavelengths and intensity, are analyzed using an equivalent circuit with lump elements. The model, although simplistic, is able to reproduce satisfactorily the normal and inverted hysteresis observed in the I-V curves. We suggest that the intimate mechanism accounting for the hysteresis may be related to the effect of charge carrier trapping and detrapping at the surface states present in the pristine SiNW arrays. We show that traps filling by tuning the light wavelength may be used as a method to determine their origin and electronic properties.

2. Experimental

Inter-connected silicon nanowire arrays have been fabricated via metal-assisted chemical etching (MACE) as shown in the flow chart presented in Fig. 1 Single-sided polished samples (1×1 cm^2) cut from (100) oriented silicon wafers (p-type, with resistivity of $1 - 10\ \Omega\cdot$cm and thickness of 625 ôm) were used in the process. The samples were cleaned with acetone, methanol, isopropanol, and deionized water followed by drying in N_2 gas flow, then treated with HF:H_2O (1:3) solution for 3 min to remove the native oxide. To obtain the SiNW arrays, the polished side of the samples were coated with Ag nanoparticles by immersing them in HF [3 M]:$AgNO_3$ [1.5 mM] solution for 1 min. The coated samples were then cleaned with DI-water to remove the excess of Ag nanoparticles. The samples subsequently underwent etching process by immersing them in an etching solution of HF [5 M]:H_2O_2[0.4 M] for 1.5 min and 5 min, respectively, followed by immersion in H_2O:HNO_3 (3:1) to remove residual Ag nanoparticles. Finally, the samples were cleaned with DI-water, then dried with N_2 gas. For electrical measurements, two coplanar Al contacts, 2×10 mm^2 each, with the thickness of 150 nm were deposited on the surface of the samples via a hard mask. The distance between the two contacts is 6 mm. Contacts deposition was made by using an electron beam evaporator (Polyteknik Cryofox Explorer 600 LT).

Micrographs of the SiNWs were recorded on the top and at a tilt angle to observe the in-depths of the structures, by using a field emission scanning electron microscope (FE-SEM), FEI NovaTM NanoSEM 630. The structural characteristics of the SiNW arrays were investigated by using a SmartLab X-ray diffraction system from Rigaku Corp. (Osaka, Japan). X-ray reciprocal space maps (RSMs) around Si (004) reciprocal lattice point were recorded in triple-axis configuration (ultra-high resolution) with a four-bounce Ge monochromator with two reflections at incidence and a two-bounce Ge monochromator with two reflections in the front of detector. Bending profiles were obtained using grazing-incidence XRD in asymmetric skew geometry on (111) reflection. In this configuration, the incidence angle of the source was varied from 0.5° to 4° to obtain different X-ray penetration depth.

The photoluminescence (PL) emission spectra of the SiNW arrays were recorded with an Edinburgh FL920 fluorescence spectrophotometer equipped with microsecond flashlamp as an excitation source. Time-correlated single photon counting (TCSPC) technique was used to determine the photoluminescence lifetime, using excitation at 300 nm and recording the emission at 770 nm wavelength. FAST Version 3.4.2. Edinburgh Instruments Ltd software was used for experimental fit.

The I-V and C-V characteristics were measured using a Keithley 2400 and SCS 4200 Keithley system, in dark and under light illumination with various wavelengths, as well as under white light using a solar simulation lamp, with intensities in the range 20–100 mW/cm^2. The curves were recorded by forward and reverse sweeping the applied voltage in the range -10V to +10V.

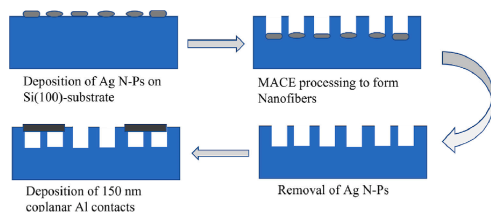

Fig. 1. Schematic illustration of the MACE steps for SiNWs preparation and Al/SiNWs/Al structures fabrication.

3. Results

3.1. Structure and PL properties of silicon nanowires

The top and cross-sectional SEM micrographs of the SiNW arrays obtained at 1.5 min and 5 min etching time, are shown in Fig. 2a–d. The length of the NWs is about 700 nm after 1.5 min etching (see Fig. 2a-b) and 1000 nm after 5 min etching (Fig. 2 c-d). In the following we refer to these two samples as $SiNW_{short}$ and $SiNW_{long}$, respectively. There is a saturation value so that the lengths of the wires are limited with the respect of the concentrations of the oxidizing agent H_2O_2, $AgNO_3$ concentration, and specific resistivity (ρ) of bulk Si [20]. As seen, the wires are laterally interconnected and form continuous structures of walls in both arrays. According to ImageJ analysis, the coverage area is 36% and 32% for $SiNW_{short}$ and $SiNW_{long}$, respectively, which suggests that the longer etching time leads to a higher porosity. Note that the coverage area means the surface occupied by tips of SiNWs observed in SEM top view image and by longer etching time the diameter of SiNWs decreases and as result the coverage area decreases. In order to investigate the microstructural features of the nanowire arrays, we performed X-ray diffraction in high resolution setup. X-ray reciprocal space maps (RSMs) around Si (004) reciprocal lattice point give information regarding the out-of-plane lattice value, relative lattice strain and the crystal imperfections. X-ray RSMs along (q_z, q_x) coordinates for $SiNW_{short}$ and $SiNW_{long}$ arrays are presented in Fig. 3a and b. The reciprocal space coordinates q_x and q_z are projections of the scattering vector along [100] and [001] directions, respectively, and are related with the angular coordinates as: $q_x = [2\sin(\omega - \theta)]/\lambda$ and $q_z = (2\sin\theta)/\lambda$.

The X-ray reciprocal space maps present an intense peak located around $q_z \in (0.7360 - 0.7365)$ Å^{-1}. Using the crystallographic relations for cubic crystals, the lattice constant a can be expressed as $\frac{4}{q_z}$ [21], giving a lattice constant equal to 5.43 Å, which corresponds to the lattice

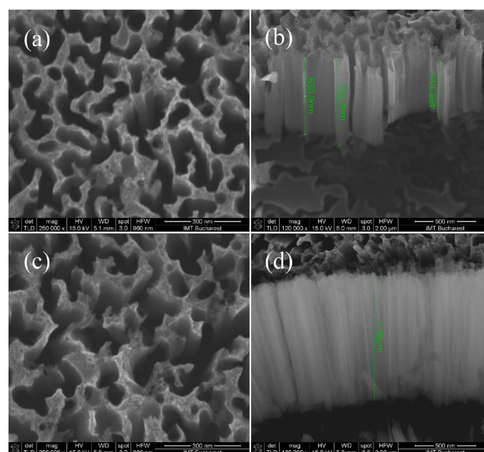

Fig. 2. SEM micrographs of the SiNWs arrays prepared by a MACE process. The etching time was: (a), (b) 1.5 min and (c), (d) 5 min.

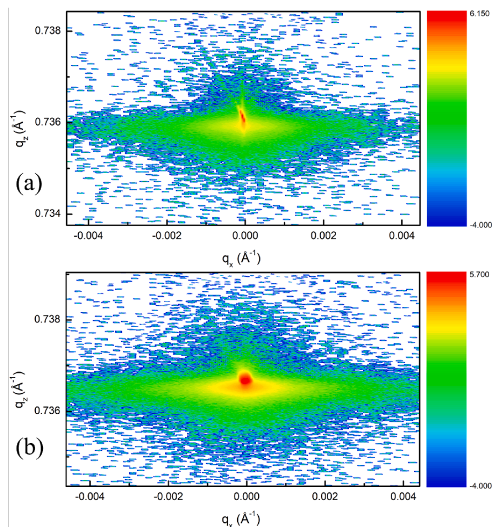

Fig. 3. X-ray reciprocal space maps (RSMs) recorded near Si (004) reciprocal lattice point on the nanowire arrays with length of (a) 700 nm and (b) 1000 nm SiNWs.

parameter of bulk Si. This is an indication that the MACE process does not affect the value of the lattice parameter of the samples. Further, it can be observed that the spot broadening increases with increasing the nanowire length in both q_z and q_x direction. The broadening of the RSM spot can be ascribed to the occurrence of bending and torsion of nanowire array, which is more pronounced for the longer (1000 nm) SiNWs, due to a higher surface energy. At the same time, the X-ray scattering in the reciprocal space looks different. For instance, the area elongated along q_x, which is related to the diffuse scattering, could be determined by crystal imperfections (e.g. point defects, extended defects, or stacking faults), and broader angular dispersion is observed for the longer nanowires. The cross section of intensity distribution of our RSM along q_x is presented below in Fig. 4a.

The X-ray rocking curves indicate two types of scattering: (1) the narrow peak is related to the specular scattering (I_{spec}), also called Bragg scattering, where the X-ray scattering has taken place on the atomic planes; (2) the broad feature indicates the presence of the X-ray diffuse scattering (XDRS), further denoted as I_{diff}. This scattering is determined by the structural imperfections in the Si lattice. To have a qualitative description of the X-ray scattering, we obtain the ratio between $I_{\text{diff}}/(I_{\text{diff}} + I_{\text{spec}})$. For instance, the shorter SiNWs exhibits a ratio of 0.31, whereas the longer SiNWs exhibits ratio of 0.94. Clearly, this ratio can be viewed as a measure of the structural defect density in our samples. It is reasonable to assume that the longer SiNWs possesses a higher density of the structural defects, being promoted by the strain relaxation processes due to the bending and torsion phenomena [22].

To prove the existence or absence of the strain relaxation processes, we obtained bending profiles of our samples, which correspond to the average tilt of the arrays - Fig. 4 b. These profiles were obtained in the framework of grazing-incidence X-ray diffraction on highly-asymmetric (111) reflection, which allowed us to attain different X-ray penetration depths, varying the incidence angles of the X-ray source. Further details regarding the grazing-incidence X-ray diffraction technique on (111) in nanowires, as well as for the bending profiles can be found in [23].

The evolution of the FWHM of the X-ray spectra with the incidence angle gives the tilt of nanowire array at different penetration depths. One may observe that the shorter nanowires determine a smaller tilt, e.g. 0.028°, comparing to the longer ones which have an average tilt of 0.037°. It is clear that the higher tilt for the longer nanowires is determined by a higher surface energy of the nanowire array. However, for both samples the bending profiles do not present dips, whose occurrence can be assigned to a quasi-local manifestation of some relaxation mechanisms in the nanowires. The absence of the strain relaxation processes can be further attributed to the absence of the extended structural defects, such as edge and screw threading dislocations. This is possible by taking into account the small length of our arrays. Also, previous investigations in highly dense nanowire arrays prepared by MACE showed the occurrence of edge and screw threading dislocations only for wires longer than 9 μm [23]. At the same time, we must consider the previous findings from the rocking curves profiles, indicating a relationship between the array length and the XRDS intensity, which was attributed to the presence of the structural defects.

The XRD findings indicate that the MACE process has determined the formation of 0D defects, nanocrystals or nanopores on the surface of SiNWs, rather than extended structural defects. The nature of structural defects is analyzed by recording the photoluminescence (PL) emission from SiNWs arrays. The PL spectra are shown in Fig. 5.

The $\text{SiNW}_{\text{short}}$ presents a rather weak PL intensity, about 1/15 of the PL for the $\text{SiNW}_{\text{long}}$. The spectrum is centered at 730 nm (1.70 eV). Sample $\text{SiNW}_{\text{long}}$ shows an intense and broad PL emission spectra in the VIS-NIR region, centered at 770 nm (1.61 eV). The red-shift in energy of 80 meV of the PL maximum position, observed for the longer NWs, could be related to the structure of interconnected skeletons and increased porosity, as resulted during the MACE process with a longer duration [20]. The observed red-shift with longer etching time is in agreement with our previous results [20]. It has however worth noting that others researchers [24], have observed blue-shift upon increasing etching time

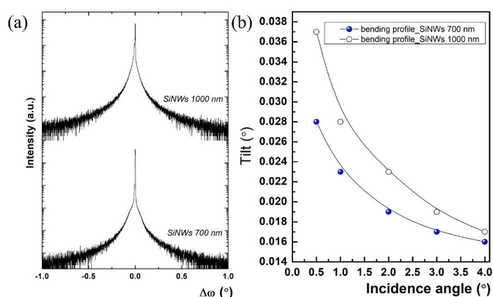

Fig. 4. Cross section of intensity distribution along q_x direction for short and long nanowire arrays (a) and (b) bending profiles.

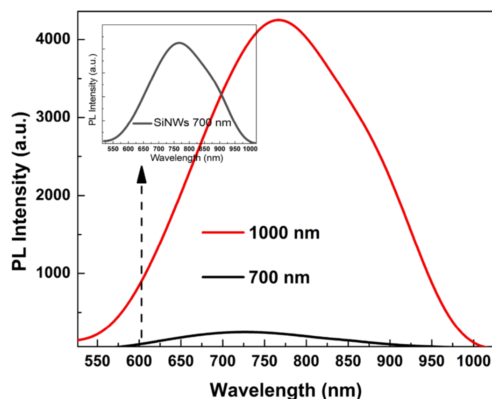

Fig. 5. PL spectra of SiNWs arrays under excitation with Xe lamp at wavelength of 350 nm and 450 W power.

and correlated that with the presence of SiO_x. It appears that in our case, the SiO_x fraction is not increasing with the etching time and consequently has a low contribution to the PL emission which strongly shifts towards NIR spectral range. A slow (S) band in the red-yellow spectral range with long microsecond decay times is reported and analyzed in porous silicon nanostructures PL spectra and attributed to phonon-assisted exciton recombination within the silicon nanostructure [25]. It was also reported that TEM images of the luminescent SiNWs prepared by MACE technique reveal that the surfaces of the SiNWs are very rough, with a few nano-sized silicon particles being attached to the SiNWs. The PL spectrum of such SiNWs was peaked at 700 nm for an excitation wavelength of 400 nm [26].

Lin et al. [27] reported that SiNWs synthesized via MACE exhibit a nanoporous structure. The PL emission band in the red region, at 730 nm was attributed to the excitons captured by the interface states between the Si nanostructures and the native oxide layer. The PL intensity increases with the porosity [27]. It was also reported that longer etching time, or higher H_2O_2 concentration could facilitate the diffusion and nucleation of Ag ions and effectively enhance the porosity of the nanowires [28]. Recently, it was shown that MACE-produced SiNW arrays are covered with porous structures, silicon nanocrystals, which result from the lateral etching of NWs sidewalls. The broad PL spectrum centered at 695 nm (1.78 eV) is attributed to radiative recombination of excitons in these nanocrystals [29]. In our experiment, even if the length of the NWs does not differ very much, the PL intensity is substantially higher in the case of long wires which suggests the formation of a larger number of luminescence centers.

The enhancement of the PL intensity and the wavelength red-shift could be attributed to enhanced porous structure of the SiNWs surface and also of a porous Si layer formed at the base of SiNWs, resulting after a longer MACE process [30,31]. Previous studies reported that HF post etching treatments of SiNWs are mandatory in order to obtain light emission [32]. Other experiments demonstrated that H_2O_2 could favor PL emission, which is attributed to SiO_2 layer formation on the NWs surface [24]. However, in this work a different etching process in terms of reagents concentration leads to a significant intensity of the PL emission, without any post-treatment, as also observed by reference [33]. This result underlines the essential role of the etching solution concentration on the formation of various light emitting centers, such as Si nanostructures, SiO_2 layer, other specific Si bonding structure. The PL lifetime of the SiNWs arrays, was measured by transient photoluminescence spectroscopy (TCSPC) method.

Fig. 6 shows PL emission decay curves of the SiNWs arrays obtained by using the excitation wavelength 300 nm and the emission wavelength 770 nm. The monoexponential lifetime decreases sharply for shorter

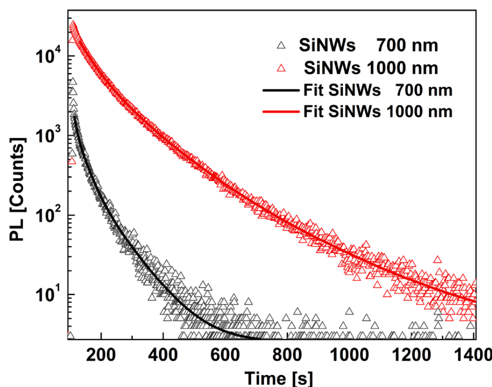

Fig. 6. PL emission decay curves of the SiNWs arrays, with average lifetime 111 μ s (1000 nm length) and 60 μ s (700 nm length), respectively.

SiNWs, indicating a smaller contribution of the surface disorder. Long lifetime observed for the longer SiNWs should be mostly dictated by nonradiative processes involving surface defects, in agreement with the results of XRD-RSM maps presented in Fig. 3. The average lifetime obtained by fitting the experimental values is 60 ôs for the short SiNWs and 111 ôs for long SiNWs. By increasing the etching time, the number of both radiative and non-radiative centers increases, however their ratio remains relatively unchanged and that determines longer luminescence lifetime coupled with stronger radiative emission.

3.2. Electrical characteristics of silicon nanowires

The I-V curves of the Al/SiNWs/Al structures, measured at various voltage sweep rates in dark and under illumination, are presented in Fig. 7 a–j. The plots are non-linear, characteristic to two diodes in antiparallel configuration, due to the Al-Si Schottky contacts. The current intensities under illumination are slightly higher compared to those measured in dark. The hysteresis observed in the I-V curves of both samples suggests that a process of trapping and de-trapping of minority (e) charge carriers, with different time constants, may take place. A dependence of the hysteresis area (in VA units) as a function of the voltage sweep rate may also be observed, see Fig. 8a and b.

In the case of the $SiNW_{short}$ sample the hysteresis area in quadrant 1, defined as area of the "down" curve minus the area of the "up" curve, shows a continuous decrease as the voltage sweep-rate increases, see Fig. 8a, but remains in the positive range of values. A different behavior may be observed in the case of $SiNW_{long}$, as the hysteresis area takes negative values at small V rates and positive values for rates beyond 1.38 V/s, see Fig. 8b. Also, the data reveal that the hysteresis area increases under illumination for short NWs, see Fig. 8a, but exhibits an interesting evolution at sweep rates below 4 V/s in the case of long NWs, Fig. 8b. Additional results obtained on SiNW arrays with lengths larger than 1000 nm and exhibiting different morphologies are shown in the Supplementary Material, Fig. S2. where it has been observed that post-treated SiNWs with HF shows minimum hysteresis and confirm that surface defect-free nanowires can be prepared by MACE using an HF post-treatment. This result is in good agreement with Choi et al [34]. It is worth noting that the untreated bulk Si shows no hysteresis and confirms the larger defective surface area of SiNWs is associated with charge trapping and hysteresis effect. The corresponding plot is shown in Supplementary Material, Fig. S3. As apparent, the extend of the hysteresis is not related with etching time in the range tested (2–10 min).

4. Modeling the I-V characteristics

We consider an equivalent electrical circuit of the Si/SiNWs/Al structures to model the observed memristive behavior of measured I-V curves. The memristive effect consists in the dependence of the I-V curve, and consequently of the electrical resistance of the device, on the history of the applied voltage, i. e. increasing or decreasing [9]. I-V hysteresis loops for multiple cycles are shown in the Supplementary Material, Fig. S1. The I-V experimental data show exponential-like dependencies, and a difference between the current ǣupg, I_{up}, i.e. when the voltage increases, and the current ǣdowng I_{down}, i.e. when the voltage decreases. A simple model to account for this behavior should combine a resistor, two diodes, and one or two capacitors, as illustrated in Fig. 9. The role of the diodes is to give the exponential-like current as a function of voltage, and the role of the $R-C$ block is to generate a voltage drop u which controls the number of charge carriers passing through the circuit. The voltage u corresponds to an electric field internal to the diodes, such that the currents through each diode D_j, $(j=1,2)$ can be written as:

$$I_{D_j}(t) = I_j\left[e^{\frac{q[V(t)-u(t)]}{n_jkT}} - e^{\frac{-qu(t)}{n_jkT}}\right] \tag{1}$$

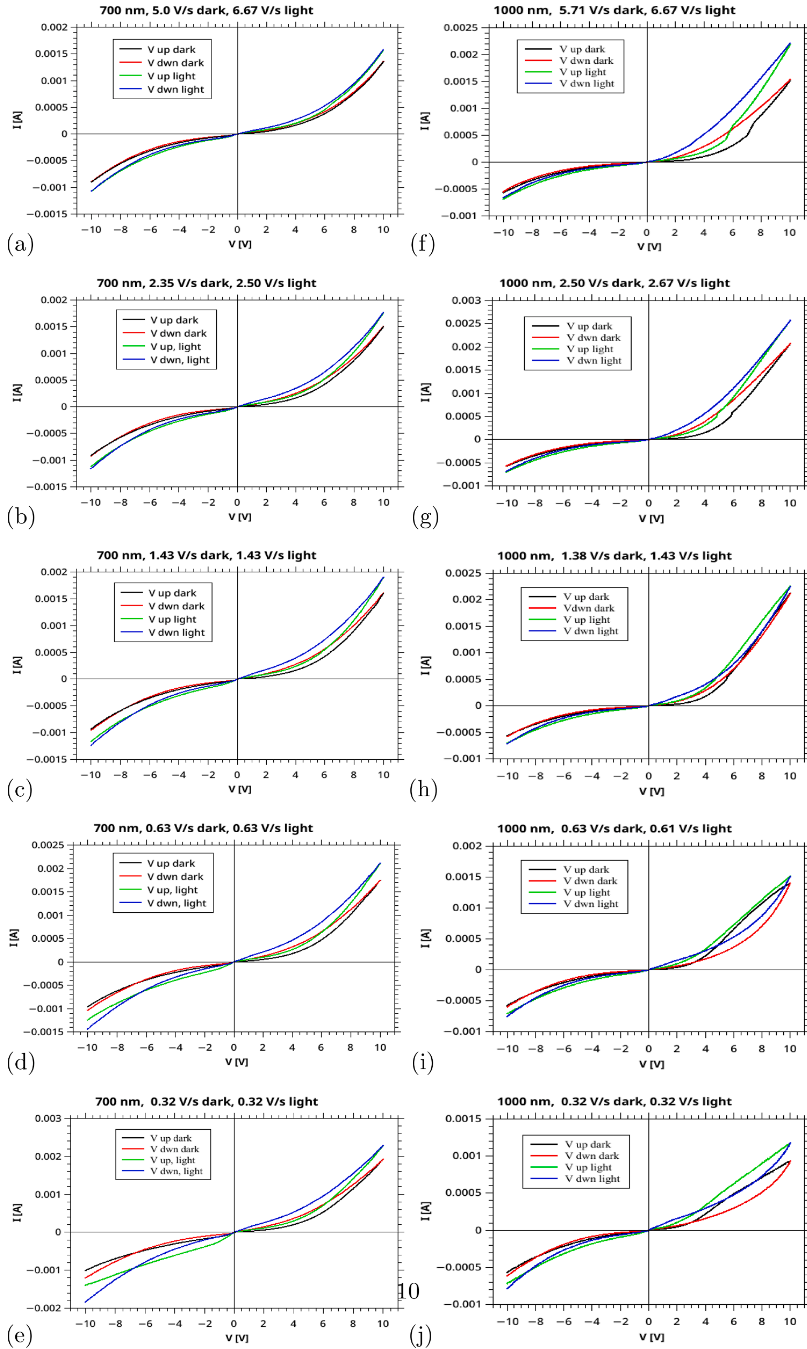

Fig. 7. Current-voltage characteristics of Al/SiNWs/Al structures: (a)-(e) short SiNWs and (f)-(j) long SiNWs, measured at various voltage sweep rates. In dark and under illumination measurements.

where I_j and n_j are diode parameters (saturation current and ideality factor, respectively), q is the elementary electric charge, k is Boltzmanns constant, and T the temperature. We begin by considering only one capacitor, C_1, and ignore the second one, i.e. $C_2 = 0$. The total current in the circuit is then:

$$I = I_{D_1} + I_{D_2} = I_R + I_{C_1}, \tag{2}$$

where $I_R = u/R$, and I_{C_1} is discussed below.

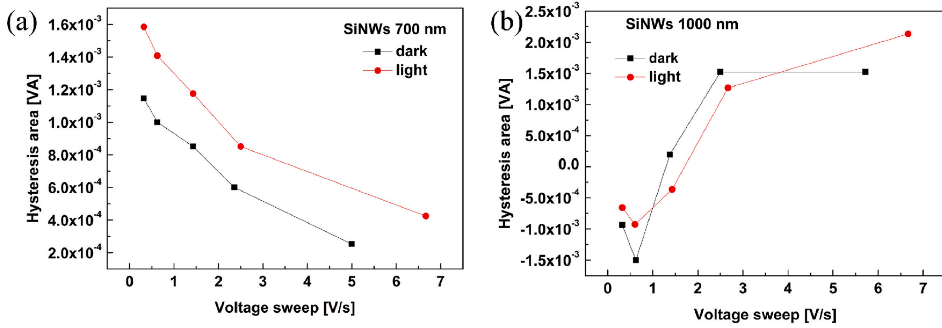

Fig. 8. Hysteresis area vs voltage sweep rate for the device: (a) short SNWs and (b) long SiNWs.

The order of magnitude of the charge associated with the capacitance C_1 needed to explain the experimental data can be inferred from the observed hysteresis effect. The total charge going through the circuit corresponds to the area of the current versus time, which can easily be evaluated since the voltage has a constant rate in time. For example, for the $SiNW_{short}$ sample, at a voltage rate of 0.63 V/s in dark (Fig. 7d), the hysteresis area between the positive voltages 4 V and 5 V, corresponding to a time interval of 1.6 s, is 0.15 mVA, or 0.24 mAs or 0.24 mC of electric charge. This gives an estimated $C_1 \approx 0.24$ mF, which is obviously a very large value for such a small sample. A more realistic assumption is to assume a much smaller capacitance, and associate the capacitor with a trapping mechanism, which temporarily stores a relatively small amount of charge, Q_1, but contributes significantly to the voltage u, which in turn has a much larger effect on the current than the stored charge. The capacitance is associated to a temporary polarization effect, likely due to interface states in the Schottky diodes [35] and/or surface states [11,12]. Therefore, we assume that the current controlled by the capacitor is

$$I_{C_1} = b\frac{dQ_1}{dt} \tag{3}$$

where b is a coefficient describing the amplification factor of the number of carriers controlled by the polarization effects associated with the charge Q_1. Here Eq. (3) is a simplified version of Equation (5) of Reference [12], where both acceptor-like and donor-like traps are considered.

Next, we denote by τ_1 the time constant associated to the relaxation of this electric or trapping charge. This relaxation process may depend on more complex phenomena, like ion displacement, diffusion, etc., which we cannot describe in detail. Instead, we define the relaxation time τ_1 via the equation

$$\frac{dQ_1}{dt} = -\frac{Q_1(t) - C_1 u(t)}{\tau_1} \tag{4}$$

which leads to an exponentially asymptotic charging or discharging with a time factor e^{-t/τ_1}. A similar assumption has been used to explain the hysteresis phenomenon in perovskite based solar cells [36].

In Fig. 10 we show the calculated I-V characteristic using empirical parameters inspired by the experimental results, but also adjusted for the convenience of the numerical calculations: $I_1 = 0.04$ mA, $I_2 = 0.03$ mA, $n_1 = -n_2 = 30$, $\tau_1 = 6$ s, $C_1 = 1.5$ nF, $b = 10^6$, $R = 1600\ \Omega$. The voltage is swept from -5 V to 5 V and back to -5 V in 50 seconds, i.e. with a rate of 0.4 V/s. The current was calculated numerically using Eqs. (1)–(4), by discretizing the time in small steps, with initial conditions $Q_1 = 0$. (The current in the two diodes was obtained using the Lambert function, since the voltage $u(t)$ implicitly depends on the current.)

The intersection of the “up” and “down” curves at negative voltages occurs because of the initial and final state of the capacitor (uncharged vs. charged). However, one feature of the hysteresis loop shown in Fig. 10 differs from the experiment. For positive voltage, the æupg curve is always above the down curve, i.e. opposite to the experimental data obtained for the sample A (700 nm). The reason is that after the voltage reached the maximum and begins to decrease, the capacitor C_1 pushes current against the main current of the source, i.e. decreasing the current compared to the “up” values. This effect does not depend on the magnitude of the coefficient b, but on its sign, which is positive. To match the experimental data with this simple model we need to assume a *negative* sign of this coefficient b for the “up” segment of the I-V characteristic, i.e. in that phase the trapping mechanism releases current with the same orientation as of the total current. The resulting I-V curves are shown in Fig. 11.

The I-V characteristic looks now qualitatively similar to the experimental data shown in Fig. 7a–e. This similarity suggests a negative intrinsic polarization mechanism of the sample, during the measurements, with a relaxation time of the order of seconds. Such a situation can also be obtained in perovskite based solar cells, where the “up” and “down” currents in the hysteresis loops can be inverted, depending on the sign of the polarization of the cell [16,36]. It is also seen in Fig. 7 that in presence of light the magnitude of the current increases, due to increased number of photogenerated charge carriers.

An additional feature may be observed in the I-V curves of the sample

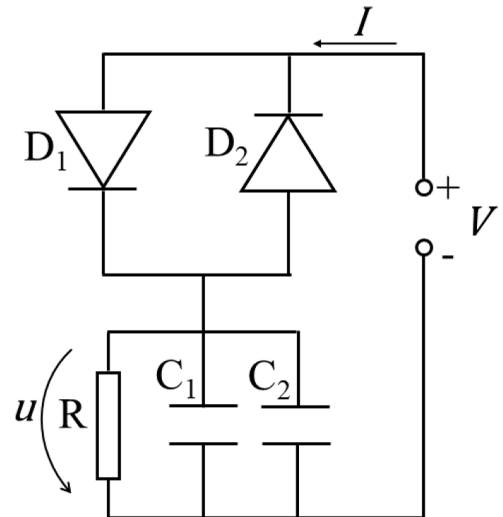

Fig. 9. A simple circuit model for the I-V characteristic with hysteresis. The direction of the current depends on the polarity of the main voltage V(t).

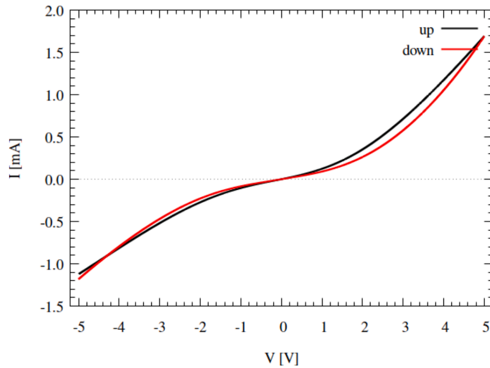

Fig. 10. The I-V characteristic with a normal current I_{C_1}. When the voltage V decreases (along the "down" curves) I_{C_1} is oriented against the source, if it is released by a normal capacitor, and consequently the total current is smaller than it was when V increased (the "up" curves).

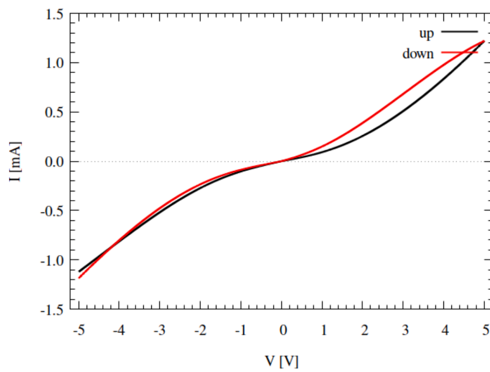

Fig. 11. The calculated I-V curves with the same parameters as in Fig. 9, but negative coefficient b. In this case the current for positive voltage is smaller when the voltage decreases, as observed for the samples of 700 nm.

$SiNW_{long}$, where the hysteresis for positive voltage reverses with decreasing the voltage rate, see Fig. 7f–j. An initial shoulder is visible at high rates on the "'up" curve, below the "down" curve, which then moves above the "down" curves at lower voltage rates, below 1.38 V/s. For lower voltage rates the hysteresis loop becomes twisted. A possible interpretation is that in this situation another capacitor, C_2, is activated at a certain positive voltage, acting now in the regular manner, i.e. pumping current against the source, $I_{C_2} = b\, dQ_2/dt$ with the b coefficient always positive. In Fig. 12 we show the results with $C_2 = 0.6$ nF. Such an example looks qualitatively similar with the data for the sample $SiNW_{long}$ shown in Fig. 7h–j. Such a twisted hysteresis loop has been shown by Thissandier et al. [37], for an array of disconnected SiNWs, when the voltage was increased above a certain threshold.

We emphasize that the model used for explaining the I-V curves is primitive, and only qualitative. The magnitude of the b coefficient and of the capacitances have somehow a complementary character: we could increase one by decreasing the other one. However, for a small b value the capacitances would be unrealistic, and for this reason we believe their role is more like a trigger for activation of more charge carriers, typical for a small polarization field inside a Schottky or a p-n diode, or for a gate inside a transistor. Since the NWs are formed in p-type Si, with resistivity of the order of 1–10 Ω·cm, then shunt resistors should be included for a more realistic circuit model. Still, the development of a more complex equivalent circuit is beyond the scope of this study.

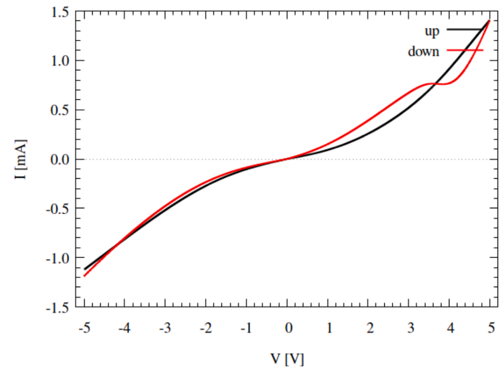

Fig. 12. The calculated I-V curves with the same parameters as in Figure 3, plus second capacitor $C_2 = 0.6$ nF which is activated gradually between voltages 0.5–1 V. The current created by the second capacitor has always a positive coefficient b.

4.1. Capacitance behavior under illumination

The C-V characteristics of the SiNW arrays measured at various frequencies are shown in Fig. 13a and b. Both structures exhibit reduced capacitance by increasing the frequency in the range 5–100 kHz, with maximum value of 9.9 nF, Fig. 14a, and 3.7 nF, Fig. 14b, at 5 kHz. However, the SiNW arrays with long NWs exhibit asymmetric behavior in the region of positive voltages, 0 to +10V, where large and switching hysteresis loops appear under the forward and reverse polarization. The presence of a positive or negative sign of the current due to traps, or equivalently, negative or positive capacitance, as proposed in the equivalent circuit, could explain the observed behavior.

Next we show the C-V characteristics measured under illumination with various wavelengths, in Fig. 14a and b. The capacitance of the structure with short NWs slightly increased when the structure is illuminated at 650 nm and 532 nm wavelength, Fig. 14a, while the structure with long NWs exhibits a significantly reduced capacitance under illumination at these wavelengths, Fig. 14b, likely due to the effect of photogenerated carries trapped at the surface states, lowering the value of the capacitive reactance. Fig. 14b also shows the capacitance changing slightly under illumination with 450 nm or 405 nm wavelength. In this case the photogenerated carriers behave like free carriers and determine the increase of the current intensity, see I-V characteristics in Fig. 7.

Fig. 15 shows the C-V characteristics under illumination with white light, with various intensities. Both structures exhibit higher capacitance when the light intensity increases, reaching 26 nF for the structure with short NWs, Fig. 15a, and 1.6 nF for SiNWs with long NWs, Fig. 15b, under illumination with 100 mW/cm^2. All the C-V curves present hysteresis, noticeable under positive applied voltage, 0,+10V. The structure with long NWs shows also a supplementary capacitance peak at positive applied voltage, that increases with the intensity of light. Also, the occurrence voltage shifts towards higher values, from 1.82 V to 2.16 V with increased light intensity.

5. Discussion and conclusions

The analysis of hysteresis exhibited by the I-V characteristics shown in Fig. 7a–e, reveals that charge carriers are trapped on the surface states in sample $SiNW_{short}$, with PL average lifetime of 60 μ s, when the voltage sweep rate varies from 5 V/s to 0.32 V/s. The hysteresis area linearly increases by lowering the sweep rate, see Fig. 8a, which suggests that the

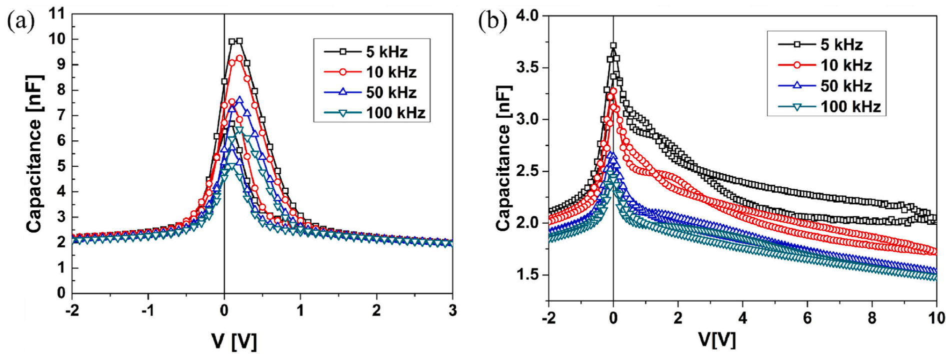

Fig. 13. Capacitance-voltage characteristics of Al/SiNWs/Al structures at various frequencies: (a) SiNWs with 700 nm length and (b) SiNWs with 1000 nm lengths.

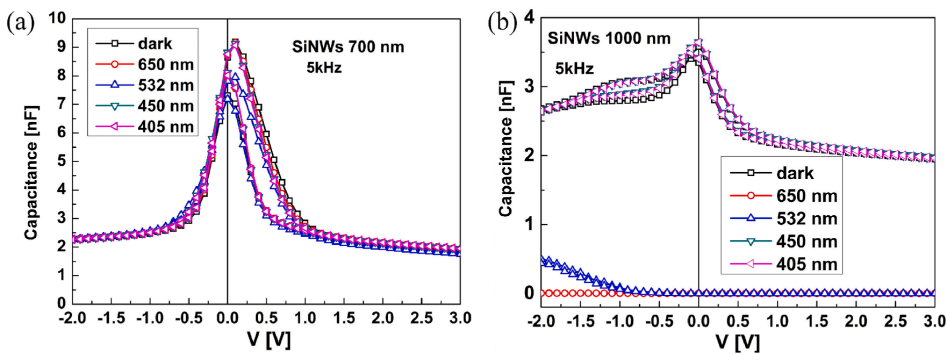

Fig. 14. Capacitance-voltage characteristics at 5 kHz, of Al/SiNWs/Al structures with: a) short (700 nm) NWs and b) long (1000 nm) NWs, under illumination with various wavelengths.

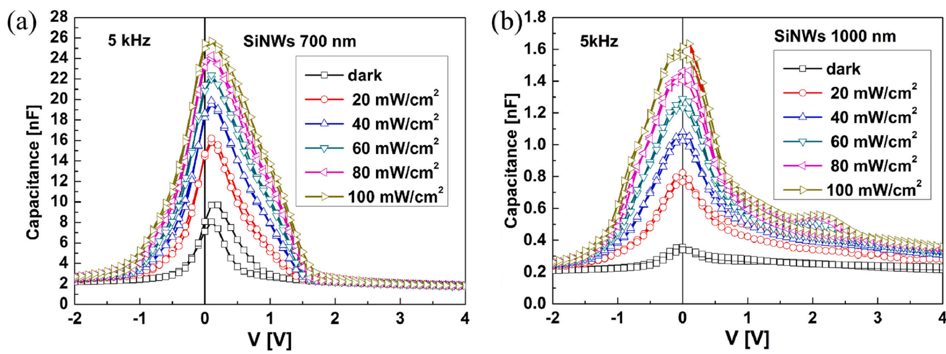

Fig. 15. Capacitance-voltage characteristics at 5 kHz, of Al/SiNWs/Al structures with: a) short NWs and (b) long NWs, as function of the white light intensity.

slow traps are involved in the process. The situation changes for the $SiNW_{long}$ sample, with PL average lifetime of 111 μ s, where larger hysteresis areas appear at faster voltage sweep rates, Fig. 7f–j. In fact, as the variation of the hysteresis area vs voltage sweep rate presented in Fig. 8a and b suggests, at slow V rates, of 0.32 V/s and 0.63 V/s, the slow traps act in the both structures. Also, since faster voltage sweeps are required to activate the fast surface states, the evolution of the hysteresis area in Fig. 8b indicates the presence of fast surface traps in the $SiNW_{long}$ sample. The I-V hysteresis in SiNWs prepared by MACE has also been obtained in Ref. [6], but the dependence on the voltage rate has not been reported. The presence of the traps in the SiNWs can also be inferred from the non-ideal diode characteristic of the Schottky contacts, observed in the I-V characteristic [38].

The C-V response of this structure to excitation with various wavelengths suggests the presence of electron traps active at energy below 2.4 eV (observed in C-V responses at 1.9 eV and 2.33 eV irradiation), which are within the band gap of porous silicon [39–41]. Although these band gap values are also within the (broad) emission band limits observed in Fig. 5, they are different than the values derived from the maxima in the PL emission spectra, centered at 1.70 eV for $SiNW_{short}$ and

1.61 eV for $SiNW_{long}$, suggesting that different trap centers are involved in the PL emission and photogeneration processes.

In summary, the evolution of I-V hysteresis vs applied voltage rates was used to assess the effect of surface traps on transport properties of the pristine SiNWs arrays. The transition from an inverted to a direct hysteresis is demonstrated considering the effect of a capacitance associated with the surface traps which controls the charge current through the structure. The I-V and C-V characteristics measured under illumination with various wavelengths in the visible domain indicate that traps filling can be detected by tuning the photons energy. Using this method we assessed the energy range of the surface trap states energy of a SiNWs array.

However, the characterization methods used in this work, including PL, I-V and CV, bring evidence on effects due to the presence of surface states, but hardly allow an accurate assignment of their energy to a specific defect or complex. First, taking into account that different techniques may give specific energy values to the same defect type, and second, the fact that we deal with a highly irregular surface which allows a variety of local environments and therefore prevents an accurate identification of the defect type, then a schematic representation of the associated energy levels may be misleading.

Author Contributions

Conceptualization, RP, HGS, AM; methodology, investigation, EF, MTS, H (MACE processes, electrical measurements), CR (x-ray diffraction), IM (PL), GC (SEM), RP, EF, H (electrical characterization); modeling, AM, GAN.; formal analysis, RP, AM; data curation, EF, HGS; writing and original draft preparation, RP, NP, AM; writing, review and editing, RP, NP, AM, HGS, SI; visualization, EF, CR, IM, RP; funding acquisition, HGS, SI, and RP.

Declaration of Competing Interest

All authors have read and agreed to the published version of the manuscript. The authors declare no conflict of interest.

Acknowledgments

This work is partially funded by Reykjavik University Ph.D. fund no. 220006 and the Icelandic Research Fund Grant no. 218029-051. RP acknowledges support from the Core program 14N/2019 MICRO-NANO-SIS PLUS.

Supplementary material

Supplementary material associated with this article can be found, in the online version, at 10.1016/j.surfin.2022.102167

References

[1] P.-J. Chien, T.-C. Wei, C.-Y. Chen, High-speed and direction-controlled formation of silicon nanowire arrays assisted by electric field, Nanoscale Res. Lett. 15 (1) (2020) 1–8.
[2] H. Han, Z. Huang, W. Lee, Metal-assisted chemical etching of silicon and nanotechnology applications, Nano Today 9 (3) (2014) 271–304.
[3] B. Azeredo, J. Sadhu, J. Ma, K. Jacobs, J. Kim, K. Lee, J. Eraker, X. Li, S. Sinha, N. Fang, et al., Silicon nanowires with controlled sidewall profile and roughness fabricated by thin-film dewetting and metal-assisted chemical etching, Nanotechnology 24 (22) (2013) 225305.
[4] L. Baraban, B. Ibarlucea, E. Baek, G. Cuniberti, Hybrid silicon nanowire devices and their functional diversity, Adv. Sci. 6 (15) (2019) 1900522.
[5] Y. Guan, G. Cao, X. Li, Single-nanowire silicon photodetectors with core-shell radial Schottky junction for self-powering application, Appl. Phys. Lett. 118 (15) (2021) 153904.
[6] F. Zaïbi, I. Slama, N. Beshchasna, J. Opitz, M. Mkandawire, R. Chtourou, Effect of etching parameters on the electrochemical response of silicon nanowires, J. Appl. Electrochem. 52 (2) (2022) 273–284.
[7] T. Moh, M. Nie, G. Pandraud, L. de Smet, E. Sudhölter, Q. Huang, P. Sarro, Effect of silicon nanowire etching on signal-to-noise ratio of sinw fets for (bio) sensor applications, Electron. Lett. 49 (13) (2013) 782–784.
[8] Y. Dan, K. Seo, K. Takei, J.H. Meza, A. Javey, K.B. Crozier, Dramatic reduction of surface recombination by in situ surface passivation of silicon nanowires, Nano Lett. 11 (6) (2011) 2527–2532.
[9] G. Milano, S. Porro, I. Valov, C. Ricciardi, Recent developments and perspectives for memristive devices based on metal oxide nanowires, Adv. Electron. Mater. 5 (9) (2019) 1800909.
[10] S. Carrara, D. Sacchetto, M.-A. Doucey, C. Baj-Rossi, G. De Micheli, Y. Leblebici, Memristive-biosensors: a new detection method by using nanofabricated memristors, Sens. Actuators B 171 (2012) 449–457.
[11] D. Sacchetto, Y. Leblebici, G. De Micheli, Memristors and Memristive Systems, Springer, New York, NY, 2014, pp. 253–280, https://doi.org/10.1007/978-1-4614-9068-5_8.
[12] F. Puppo, F.L. Traversa, M. Di Ventra, G. De Micheli, S. Carrara, Surface trap mediated electronic transport in biofunctionalized silicon nanowires, Nanotechnology 27 (34) (2016) 345503.
[13] K.P. Rajeev, C. Opoku, V. Stolojan, M. Constantinou, M. Shkunov, Effect of nanowire-dielectric interface on the hysteresis of solution processed silicon nanowire fets, Nanosci. Nanoeng. 5 (2) (2017) 17–24.
[14] K. Seki, Equivalent circuit representation of hysteresis in solar cells that considers interface charge accumulation: potential cause of hysteresis in perovskite solar cells, Appl. Phys. Lett. 109 (3) (2016) 033905.
[15] B. Chen, M. Yang, X. Zheng, C. Wu, W. Li, Y. Yan, J. Bisquert, G. Garcia-Belmonte, K. Zhu, S. Priya, Impact of capacitive effect and ion migration on the hysteretic behavior of perovskite solar cells, J. Phys. Chem. Lett. 6 (23) (2015) 4693–4700.
[16] W. Tress, J.P. Correa Baena, M. Saliba, A. Abate, M. Graetzel, Inverted current–voltage hysteresis in mixed perovskite solar cells: polarization, energy barriers, and defect recombination, Adv. Energy Mater. 6 (19) (2016) 1600396.
[17] S.A. Moiz, A. Alahmadi, A.J. Aljohani, Design of silicon nanowire array for pedot: Pss-silicon nanowire-based hybrid solar cell, Energies 13 (15) (2020) 3797.
[18] P. Yu, J. Wu, S. Liu, J. Xiong, C. Jagadish, Z.M. Wang, Design and fabrication of silicon nanowires towards efficient solar cells, Nano Today 11 (6) (2016) 704–737.
[19] R. Rurali, Colloquium: structural, electronic, and transport properties of silicon nanowires, Rev. Mod. Phys. 82 (1) (2010) 427.
[20] E. Fakhri, M. Sultan, A. Manolescu, S. Ingvarsson, N. Plugaru, R. Plugaru, H. Svavarsson, Synthesis and photoluminescence study of silicon nanowires obtained by metal assisted chemical etching. 2021 International Semiconductor Conference (CAS), IEEE, 2021, pp. 147–150.
[21] H. Stanchu, A. Kuchuk, M. Barchuk, Y.I. Mazur, V. Kladko, Z.M. Wang, D. Rafaja, G. Salamo, Asymmetrical reciprocal space mapping using x-ray diffraction: a technique for structural characterization of GAN/ALNsuperlattices, CrystEngComm 19 (22) (2017) 2977–2982.
[22] V.M. Kaganer, B. Jenichen, O. Brandt, Elastic versus plastic strain relaxation in coalesced gan nanowires: an x-ray diffraction study, Phys. Rev. Appl. 6 (6) (2016) 064023.
[23] C. Romanitan, M. Kusko, M. Popescu, P. Varasteanu, A. Radoi, C. Pachiu, Unravelling the strain relaxation processes in silicon nanowire arrays by x-ray diffraction, J. Appl. Crystallogr. 52 (5) (2019) 1077–1086.
[24] S. Congli, H. Hao, F. Huanhuan, X. Jingjing, C. Yu, J. Yong, J. Zhifeng, S. Xiaosong, Synthesis of porous silicon nano-wires and the emission of red luminescence, Appl. Surf. Sci. 282 (2013) 259–263.
[25] L. Canham, Introductory lecture: origins and applications of efficient visible photoluminescence from silicon-based nanostructures, Faraday Discuss. 222 (2020) 10–81.
[26] D. Jung, H. Sohn, Y. Kim, Optical characterization of luminescent silicon nanowires, J. Korean Phys. Soc. 74 (2) (2019) 140–144.
[27] L. Lin, S. Guo, X. Sun, J. Feng, Y. Wang, Synthesis and photoluminescence properties of porous silicon nanowire arrays, Nanoscale Res. Lett. 5 (11) (2010) 1822–1828.
[28] S.A. Razek, M.A. Swillam, N.K. Allam, Vertically aligned crystalline silicon nanowires with controlled diameters for energy conversion applications: experimental and theoretical insights, J. Appl. Phys. 115 (19) (2014) 194305.
[29] M. Naffeti, P.A. Postigo, R. Chtourou, M.A. Zaïbi, Highly efficient silicon nanowire surface passivation by bismuth nano-coating for multifunctional bi@ sinws heterostructures, Nanomaterials 10 (8) (2020) 1434.
[30] I. Leontis, A. Othonos, A.G. Nassiopoulou, Structure, morphology, and photoluminescence of porous si nanowires: effect of different chemical treatments, Nanoscale Res Lett 8 (1) (2013) 1–7.
[31] H. Okayama, K. Fukami, R. Plugaru, T. Sakka, Y.H. Ogata, Ordering and disordering of macropores formed in prepatterned p-type silicon, J Electrochem Soc 157 (1) (2009) D54.
[32] C. Amri, H. Ezzaouia, R. Ouertani, Photoluminescence origin of lightly doped silicon nanowires treated with acid vapor etching, Chin. J. Phys. 63 (2020) 325–336.
[33] R.-C. Wang, C.-Y. Chao, W.-S. Su, Electrochemically controlled fabrication of lightly doped porous Si nanowire arrays with excellent antireflective and self-cleaning properties, Acta Mater. 60 (5) (2012) 2097–2103.
[34] M. Dawood, T. Liew, P. Lianto, M. Hong, S. Tripathy, J. Thong, W. Choi, Interference lithographically defined and catalytically etched, large-area silicon nanocones from nanowires, Nanotechnology 21 (20) (2010) 205305.
[35] S.M. Sze, K.K. Ng, Physics of Semiconductor Devices, third ed., John Wiley & Sons, Ltd., 2006, pp. 134–196.

[36] G.A. Nemnes, C. Besleaga, A.G. Tomulescu, I. Pintilie, L. Pintilie, K. Torfason, A. Manolescu, Dynamic electrical behavior of halide perovskite based solar cells, Sol. Energy Mater. Sol. Cells 159 (2017) 197–203.
[37] F. Thissandier, A. Le Comte, O. Crosnier, P. Gentile, G. Bidan, E. Hadji, T. Brousse, S. Sadki, Highly doped silicon nanowires based electrodes for micro-electrochemical capacitor applications, Electrochem. Commun. 25 (2012) 109–111.
[38] A. Rouis, N. Hizem, M. Hassen, A. Kalboussi, Electrical properties of silicon nanowires schottky barriers prepared by mace at different etching time, Silicon (2021).
[39] J. Rams, B. Mendez, G. Craciun, R. Plugaru, J. Piqueras, Cathodoluminescence enhancement in porous silicon cracked in vacuum, Appl. Phys. Lett. 74 (12) (1999) 1728–1730.
[40] Z. Chen, T.-Y. Lee, G. Bosman, Electrical band gap of porous silicon, Appl. Phys. Lett. 64 (25) (1994) 3446–3448.
[41] T. Van Buuren, T. Tiedje, J. Dahn, B. Way, Photoelectron spectroscopy measurements of the band gap in porous silicon, Appl. Phys. Lett. 63 (21) (1993) 2911–2913.

Paper III

****

Synthesis and photoluminescence study of silicon nanowires obtained by metal assisted chemical etching

E. Fakhri *, M. T. Sultan **, A. Manolescu*, S. Ingvarsson**, N. Plugaru***, R. Plugaru***, H. G.Svavarsson*

* Department of Engineering, Reykjavik University, IS-102, Reykjavik, Iceland

** Science Institute, University of Iceland, IS-107 Reykjavik, Iceland

*** National Institute for Research and Development in Microtechnologies-(IMT) Bucharest, 077190 Voluntari, Romania

2021 International Semiconductor Conference (CAS) | 978-1-6654-3571-0/21/$31.00 ©2021 IEEE

DOI: 10.1109/CAS52836.2021.9604178

Synthesis and photoluminescence study of silicon nanowires obtained by metal assisted chemical etching

E. Fakhri *, M. T. Sultan **, A. Manolescu*, S. Ingvarsson, N. Plugaru***, R. Plugaru***, H. G. Svavarsson***

* Department of Engineering, Reykjavik University, IS-102, Reykjavik, Iceland

** Science Institute, University of Iceland, IS-107 Reykjavik, Iceland

*** National Institute for Research and Development in Microtechnologies-(IMT) Bucharest, 077190 Voluntari, Romania

E-mail: Elhamf20@ru.is

2021 International Semiconductor Conference (CAS) | 978-1-6654-3571-0/21/$31.00 ©2021 IEEE | DOI: 10.1109/CAS52836.2021.9604178

Abstract*— Silicon nanowires (SiNWs) hold potential applications in optoelectronics and SiNW-based optical sensors. Here, a photoluminescence study of SiNW arrays fabricated with a simple two-step silver (Ag) catalyzed etching of silicon wafers is presented. The morphology and photoluminescence properties were investigated for SiNWs of different lengths obtained by varying Ag concentration (as silver nitrate, $AgNO_3$) and etching time. The samples consist of vertically aligned SiNWs with length in the range ~10-40 µm. Our foremost result is that the photoluminescence intensity from the SiNW arrays is an order of magnitude higher than that from bulk Si. This is accompanied by a red-shift in the peak position of approximately 0.09 eV, which may be attributed either to the variation in size of the Ag-nanoparticles created during the etching process or different lengths of the SiNWs. The results indicate that SiNWs obtained by simple and cost-effective metal catalyzed etching, are potentially promising for optoelectronic applications.

***Keywords*— MACE, SEM, Si-nanowire arrays, photoluminescence, optoelectonics.**

1. Introduction

Owing to their unique mechanical, electrical, optical and thermoelectrical properties, silicon nanowires (SiNWs) have shown potential application in optoelectronics, bio-chemical sensing, flexible-electronics, photovoltaics and energy storage [1,2].

The commonly used approaches to fabricate SiNWs can be divided into two main categories: a) bottom-up (for instance chemical-vapor-deposition, thermal evaporation and laser-ablation) and b) top-down lithography-based methods (such as metal assisted chemical etching, MACE). The bottom-up methods are generally known to have limitation in terms of equipment complexity and expense which will hinder their application for industrial settings. On the other hand, top-down methods, particularly MACE, has proven to be scalable, inexpensive and simple to fabricate nanowires, often with superior quality [3]. Silicon MACE processing involves the deposition of either a metallic nanopattern or nanoparticles, followed by catalyzed etching water-based solution of hydrofluoric acid (HF) and an oxidizer (most commonly H_2O_2). Several metals have been proposed in assisting the etching process, of which Ag has shown to give superior results. Peng *et al.* [3] showed that the immersion of silicon wafer in a mixture of $HF/AgNO_3$ allows deposition of Ag-nanoparticles (Ag-NPS). After such metal deposition, a solution containing HF and H_2O_2 is used to etch the silicon. This method enables high etching rate, exceeding 1 µm/min, and the possibility to fabricate a wide range of vertical structures with aspect ratio of up to 10^3, depending on the shape, distribution and density of the catalytic metal particles [4]. Nanoscale silicon structures such as SiNWs are well-known for their ability to exhibit high energy peaks in room temperature photoluminescence (PL) spectra, due to quantum confinement (QC) effects and surface defects [5].

In this contribution, we report on the fabrication of SiNW arrays via MACE

Authorized licensed use limited to: Reykjavik University. Downloaded on August 04,2022 at 15:15:46 UTC from IEEE Xplore. Restrictions apply.

process by using $AgNO_3$ (aq) solution. The effects of varying $AgNO_3$ concentration and etching time on the SiNWs morphology and PL emission were investigated. Optimum $AgNO_3$ concentration and etching time was determined to give long, vertically aligned, SiNWs. We find that the PL intensity from the SiNW arrays is an order of magnitude higher than that from bulk Si, with a red shift of ~ 0.09 eV in the peak position. The possible causes for the red shift are discussed.

2. Experimental details

Single-side polished p-type (boron - doped) crystalline-Si (100) wafers with thickness of 550 μm and resistivity of 10-20 Ω.cm (carrier concentration of 10^{15} cm^{-3}) were used for the NW arrays fabrication. The process consisted into two steps: A) deposition of Ag-NPs, and B) Ag catalyzed etching of the Si wafer.

A) Prior to deposition of Ag-NPs, the samples were cleaned with acetone, methanol, isopropanol, and deionized water (DI-water) followed by drying with N_2 gas. Subsequently, the samples were treated with a solution of 40% W/V HF and water in 1:1 ratio for 3 min., to remove native oxide. After rinsing with DI water and drying with N_2, the polished sides of the Si-wafers were coated with Ag-particles by immersing them in HF [3 M]:[χ mM] $AgNO_3$ solution for 1 min, (χ=0.8, 1.0, 1.5, 3.0 mM). The deposition was ended by immersing the sample in DI-water and let to dry.

B) The samples were etched by immersion in a solution of HF:H_2O_2 [5 M:0.4 M] for a given time, followed by immersion in a mixture of H_2O and 60% w/v HNO_3 in 3:1 ratio to remove residual Ag-particles [4]. Then, the samples were rinsed with DI water and dried with N_2 gas.

In this study, the molar ratio of $AgNO_3$ and etching time were varied in order to determine their effects on the SiNWs morphology, as listed in **Table 1.**

Table 1. List of samples with different $AgNO_3$ concentration, χ, and corresponding etching time, t_e.

$AgNO_3$ χ [mM]	0.8	1.0	1.5					3
Etching time, t_e [min]	45	45	30	45	60	100	150	45

The morphology of the SiNWs was characterized by SEM (ZEISS SUPRA 35), and energy dispersive X-ray spectroscopy (EDS). The PL spectra were collected at room temperature (RT) using a Princeton Instrument Acton SP2750 triple grating monochromator/spectrograph equipped with Si-CCD detector. The SiNWs samples were mounted in a cryogenic pump (Leybold-Heraeus RG 210) and excited with a 15 mW HeCd laser, at 325 nm wavelength and a spot diameter of ~100-200 μm. A more detailed description of the set-up can be found elsewhere [6].

3. Results and discussion

Fig. 1 shows the SEM micrographs in different magnification of Ag-NPs on top of the Si wafer after being immersed in the $AgNO_3$ solution for 1 minute, rinsed and dried. The Ag-NPs are isolated, with diameters between 70 and 180 nm (for 1.5 mM $AgNO_3$), varying with the deposition time and/or $AgNO_3$ concentration [7,8]. The SEM cross-section images of etched structures presented in Fig. 2 show quasi-ordered SiNWs, with a preferential orientation along [100] crystallographic direction, in agreement with [8,9]. Initially, in the case of SiNWs obtained by etching in solutions with 0.8, 1.0 and 1.5-mM concentration, it was observed the formation of vertically aligned columnar structures, with a uniform etching depth as evidenced in the SEM images. In Fig. 2(c) the diameter of SiNWs for (1.5 mM $AgNO_3$ concentration) determined from SEM images varies between 90 and 135 nm. Also, the obtained nanowires are bundled together as a consequence of capillary forces being activated when extracting the samples out of the etching solution [7,10]. These forces become more

Authorized licensed use limited to: Reykjavik University. Downloaded on August 04,2022 at 15:15:46 UTC from IEEE Xplore. Restrictions apply.

dominant as the length of the NWs increases, thus resulting in more like a columnar structure rather than free-standing individual NWs [10]. Increasing the concentration further to 3 mM resulted in the formation of porous columnar structure with deep etch pits-like structures and reduced length. The length of SiNWs decreased from ~ 17, 15, 13 for 0.8, 1.0 and 1.5 mM, respectively, to 9 μm for the 3.0 mM $AgNO_3$ concentration, for an etching time of 45 min. The decrease in NWs length may be attributed to Si surface having less coverage, i.e. larger Ag-NPs and therefore a longer time is needed for HF to dissolve and dissipate the oxidized Si [8].

To investigate the effect of etching time (t_e = 30, 45, 60, 100 and 150 min) on the morphology, the 1.5 mM structure was considered (Fig. 3). It was observed that vertically aligned SiNWs were obtained for etching time up to 60 min (Fig. 3(b)). When increasing t_e to 100 and 150 min (Fig. 3(c)), the tips of the nanowires start to congregate and form bundles, as also has been observed in [4,11]. As seen in Fig. 3(d), the length of the SiNWs increases roughly linearly (0.37±0.05 μm/min) with etching time up to ~ 100 min, and shows a smaller dependence for longer periods.

Fig. 4 shows the PL spectra of SiNWs obtained by etching samples with various $AgNO_3$ concentrations and fixed etching time. The PL spectra measured on structures with fixed $AgNO_3$ concentration and various etching times are plotted in Fig.5. The data were deconvoluted by fitting the spectra with Gaussians to determine the peak value. Figs 4 and 5 show that the PL peak intensity increases and red-shifts from 728 to 752 nm, and from 724 to 761 nm with increasing $AgNO_3$ concentration and etching time, respectively. These results are in fair agreement with previous studies [5]. Several mechanisms, including oxygen deficient-related defect centers and QC effects [11] were reported for explaining the PL-emission of such nanostructures. The QC contribution requires that the size of nanostructures to be less that the exciton Bohr radius. However, recently it has been shown that when the diameter of the NWs is much larger than that of excitons Bohr radius (i.e. ~5 nm for Si), the resulting PL spectra is unlikely to originate from SiNWs. In such cases (as in the present one), it is more likely that the emission originates from the Si nanocrystals or nanopores on the surface of SiNWs [11].

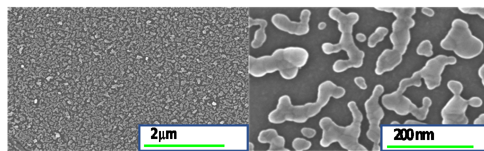

Figure 1. SEM micrographs of Ag-NPs obtained by immersing the sample in $HF:H_2O:AgNO3$ (1.5mM) in different magnification.

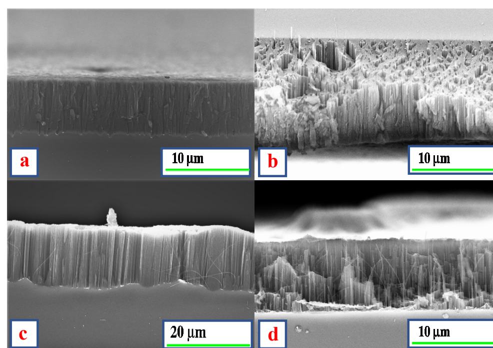

Figure 2. SEM micrographs of SiNWs obtained by etching the samples having varying $AgNO_3$ concentration i.e. (a) 0.8, (b) 1, (c) 1.5 and (d) 3 mM, respectively.

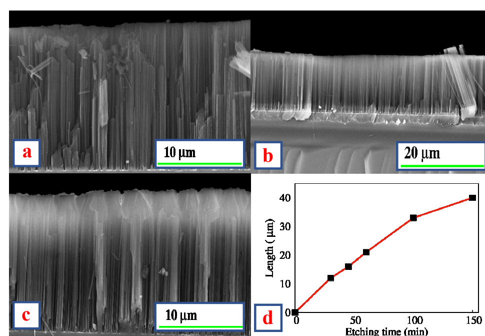

Figure 3. SEM images of nanowires obtained by etching for (a) 30, (b) 60 (c) 150 min, respectively. For each structure the Ag-NPs were obtained by immersing the samples in $HF:AgNO_3$ [1.5 mM]. (d) Plot of the SiNWs length obtained for varying etching time.

Authorized licensed use limited to: Reykjavik University. Downloaded on August 04,2022 at 15:15:46 UTC from IEEE Xplore. Restrictions apply.

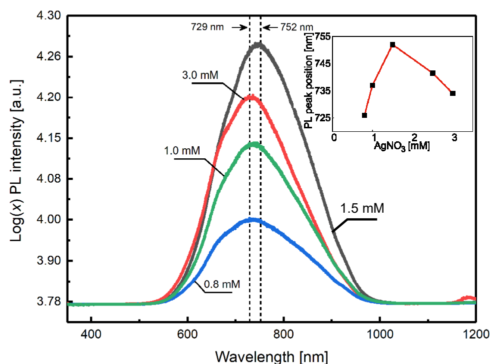

Figure 4. RT PL-spectra of SiNWs obtained for various $AgNO_3$ concentration at fixed etching time t_e of 45 min. The inset shows peak positions from respective plots obtained by Gaussian fitting.

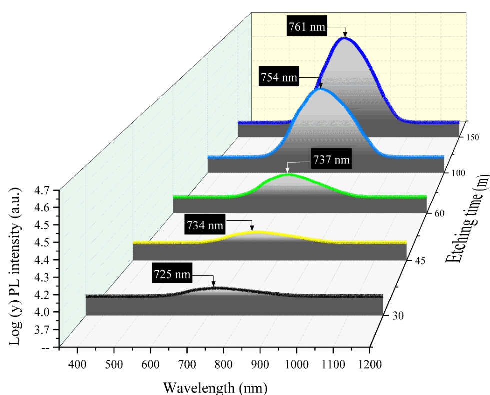

Figure 5. RT PL-spectra of SiNWs obtained for various etching time t_e for a fixed concentration of $AgNO_3$, 1.5 mM.

4. Conclusions

In summary, crystalline Si(001) p-type substrates were utilized to obtain arrays of random, vertically aligned SiNWs via MACE using Ag as a metal catalyst. The morphology and length of obtained SiNWs is evidenced to be dependent on Ag (as $AgNO_3$) concentration and the etching time. The analysis of the PL spectra reveals that the emission intensity from the SiNW arrays increases with increasing the etching time (NW length, respectively). The PL emission is likely to originate from the Si nanocrystals or nanopores on the surface of SiNWs. The results demonstrate that MACE is a promising, scalable and cost-effective process to obtain SiNW arrays with geometrically controlled PL emission, for potential application in optoelectronic and Si-based sensors.

Acknowledgments.

This work is partially funded by Reykjavik University Ph.D. fund no. 220006 and the Icelandic Research Fund Grants no. 218029-051. RP acknowledges support from the Core program 14N/2019 MICRO-NANO-SIS PLUS.

References

[1] KQ. Peng, X. Wang, L. Li, Y. Hu, ST. Lee. *"Silicon nanowires for advanced energy conversion and storage."* Nano Today 8.1.75-97, Feb 2013.

[2] A. Boukai, Y. Bunimovich, J. Tahir-Kheli, J. Yu, W. Goddard, J. Heath. *"Silicon nanowires as efficient thermoelectric materials Nat."* Lett 451. 168-71, Jan 2008.

[3] KQ. Peng, YJ. Yan, SP. Gao, J. Zhu. *"Synthesis of large-area silicon nanowire arrays via self-assembling nanoelectrochemistry."* Advanced materials. 1164-1167, Aug 2002.

[4] HG. Svavarsson, BH. Hallgrimsson, M. Niraula, KJ. Lee, R. Magnusson. *"Large arrays of ultra-high aspect ratio periodic silicon nanowires obtained via top–down route."* Applied Physics A 122.2, Feb 2016.

[5] V. Sivakov, F. Voigt, A. Berger, G. Bauer, S. Christiansen. *"Roughness of silicon nanowire sidewalls and room temperature photoluminescence."* Physical Review B 82.12. 125446, Sep 2010.

[6] MT. Sultan, JT. Gudmundsson, A. Manolescu, HG. Svavarsson. *"Structural and photoluminescence study of TiO_2 layer with self-assembled $Si_{1-x}Ge_x$ nanoislands."* Journal of Applied Physics 128.8. 085304, Aug 2020.

[7] S. Kato, Y. Kurokawa, K. Gotoh, T. Soga. *"Fabrication of a Silicon Nanowire Solar Cell on a Silicon-on-Insulator Substrate."* Applied Sciences 9.5. 818, Feb 2019.

[8] R. Venkatesan, MK. Arivalagan, V. Venkatachalapathy, JM. Pearce, J. Mayandi. *"Effects of silver catalyst concentration in metal assisted chemical etching of silicon."* Materials Letters 221. 206-210, Mar 2018.

[9] K. Gonchar, A. Zubairova, A. Schleusener, LA. Osminkina, V. Sivakov. *"Optical properties of silicon nanowires fabricated by environment-friendly chemistry."* Nanoscale research letters 11.1 .1-5, Aug 2016.

[10] B. Ozdemir, M. Kulakci, R. Turan, HE. Unalan. *"Effect of electroless etching parameters on the growth and reflection properties of silicon nanowires."* Nanotechnology 22.15. 155606, Mar 2011.

[11] M. Naffeti, PA. Postigo, R. Chtourou, MA. Zaïbi. *"Elucidating the effect of etching time key-parameter toward optically and electrically-active siliconnanowire"* Nanomaterials 10.3.404,Feb2020.

Authorized licensed use limited to: Reykjavik University. Downloaded on August 04,2022 at 15:15:46 UTC from IEEE Xplore. Restrictions apply.

Paper IV

****

Germanium coated silicon nanowires as human respiratory sensing device

E. Fakhri*, M. T. Sultan†, A. Manolescu*, S. Ingvarsson†, H. G. Svavarsson*

*Department of Engineering, Reykjavik University, Menntavegur 1, IS-102 Reykjavik, Iceland

†Science Institute, University of Iceland, Reykjavik, Iceland

2022 International Semiconductor Conference (CAS) | 978-1-6654-5255-7/22/$31.00 ©2022 IEEE

DOI: 10.1109/CAS56377.2022.9934678

Germanium coated silicon nanowires as human respiratory sensing device

E. Fakhri[*] , **M. T. Sultan**[†] , **A. Manolescu**[*] , **S. Ingvarsson**[†] , **H. G. Svavarsson**[*]
Email: Elhamf20@ru.is
[*]Department of Engineering, Reykjavik University, Menntavegur 1, IS-102 Reykjavik, Iceland
[†]Science Institute, University of Iceland, Reykjavík, Iceland

***Abstract*—We report on germanium coated silicon nanowires structures synthesized with metal assisted chemical etching and qualify their functionality as human respiratory sensor. The sensors were made from p-type single-crystalline (100) silicon wafers using a silver catalyzed top-down etching, afterwards coated by 50 nm germanium thin layer using a magnetron sputtering. The germanium post-treatment was performed by rapid thermal annealing at 450 and 700°C. The sensors were characterized by X-ray diffraction diffractogram and scanning electron microscopy. It is demonstrated that the sensors are highly sensitive as human breath detectors, with rapid response and frequency detectability. They are also shown to be a good candidate for human respiratory disease diagnoses.**

***Index Terms*—Silicon nanowire arrays, MACE, air flow sensors, humidity sensors**

I. Introduction

Sleep apnea syndrome is a potentially serious disorder during which breathing readily stops and starts with the occurrence of approximately 30 apneas during 7-8 hours of sleep. Increasing number of individuals suffer from sleep apnea complications, for instance hypertension and stroke, making sleep apnea a frequent cause of stroke. Therefore, respiratory monitoring of individuals posing sleep apnea syndrome is of prime importance.

In this context pressure and humidity sensors are of particular interest as they offer broad application in industry process control, environmental monitoring, clean rooms, medical or health care facilities, and more [1]–[3]. With rapid growth in technology, a vast variety of materials have been investigated for pressure and humidity sensing, to mention silicon nanowires (SiNWs), ZnO, GaN,TiO_2, carbon nanotubes, composite fibres/polymers(such as PDMS) combined with conductive nanostructure such as metals, carbon nanotubes and modified graphene [1], [2], [4]. However for these composite systems the long term sensing is not reliable as they tend to degrade in ambient atmosphere over time. Of these materials SiNWs pose superior characteristics due to its unique structural, electrical, optical, and thermoelectric properties [5], device compatibility, having larger surface area with high sensitivity to pressure and humidity.

It has been shown that SiNWs exhibit an anomolous piezoresistance effect, much higher than bulk silicon [6], and several sensors based on piezoresistance properties of SiNWs, prepared with metal assisted chemical etching (MACE) have also been proposed, for instance flexible pressure sensors [7], airflow sensing devices [8], or other pressure sensors [9]. Zhang et al [10], reported a flow sensor based on SiNWs NEMS sensors for a low pressure range which is critical for bio-compatible devices such as breath sensors. Additionally, stability, fast response and recovery time, and stabilized resistance baseline are important factors that most of the proposed sensors could not achieve [4]. Recently, a breath sensor based on periodic silicon nanorods was proposed [2]. In this paper we report a fabrication rout and characterisation of a low-cost, easy to fabricate, bio-compatible, and rapidly scalable breath sensor, based on random and interconnected SiNWs, coated with germanium nanoparticles.

II. Experimental

A. Materials and methods

Synthesis of arrays of random and interconnected SiNWs were fabricated on $10{\times}10$ mm^2 p-type, single-side polished, 525 µm thick Si (001) substrates, with resistivity of ρ of 0.1-0.5 Ωcm. A full description of synthesis process can be found in previous publication [5]. Briefly, a three step MACE process, with silver as metal, was performed as follows:

1) The Si substrate was deposited with Ag nanoparticles catalyst by immersing the substrate in a solution of 3 M HF and 2 mM $AgNO_3$ for 60 seconds.
2) To obtain vertically aligned SiNWs, after deposition of Ag nanoparticles, the substrate was etched by a HF:H_2O_2 (5M:0.4M) solution.
3) After etching the excess Ag nanoparticles were removed by immersing the sample in a 20% w/v HNO_3 solution.

Two structural schemes were utilized in this study including SiNWs and Ge-coated SiNWs either in as-synthesized or annealed state. For the Ge deposition, direct current magnetron sputtering was utilized at constant power of 30 W using a 5N-Ge target. Argon was utilized as working gas and the throttle valves were adjusted to stabilize the growth pressure of 0.7 Pa. After deposition, the sampler were subjected to rapid thermal annealing and ex-situ characterizations. JPilec JetFirst 150 was used to anneal the samples at 450 and 700°C under vacuum at 2×10^{-5} bar.

B. Characterization

The samples were characterized using X-ray diffraction (XRD) measurements using a Panalytical X'pert diffractometer (CuKα, 0.15406 nm) and scanning electron microscopy

2022 International Semiconductor Conference (CAS) | 978-1-6654-5255-7/22/$31.00 ©2022 IEEE | DOI: 10.1109/CAS56377.2022.9934678

Authorized licensed use limited to: Reykjavik University. Downloaded on November 11,2022 at 13:51:31 UTC from IEEE Xplore. Restrictions apply.

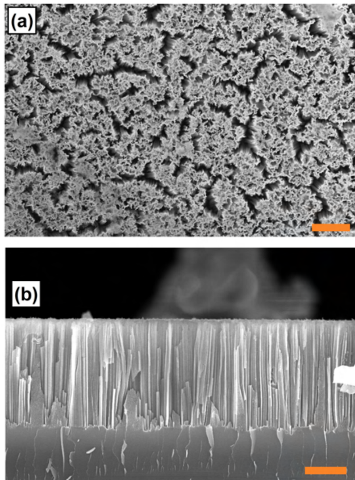

Fig. 1. (a) Top-view and (b) cross-sectional SEM micrograph of SiNWs obtained by MACE. The scale bar provided is 2μm.

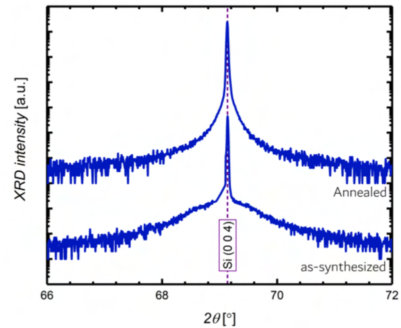

Fig. 2. XRD diffractorgram along Si (004) atomic plane obtained over SiNWs based structures both in un-annealed (lower plot) and annealed (upper plot) state.

(SEM, Zeiss Supra 35). A detailed description regarding X-ray diffraction analysis is provided in our previous work [11]. For electrical measurements, two co-planar Au-contacts, 2×10 mm^2 each, with 250 nm thickness, were deposited on the surface of the samples via a hard mask using an electron beam evaporator (Polyteknik Cryofox Explorer 600 LT). The distance between the two contacts was 6 mm.

III. Results and Discussion

A. Structure characterization

Figure 1 shows (a) top view and (b) cross-sectional view of SiNWs obtained after 20 min etching. The top view image indicates that the wires are interconnected, forming a bundled rigid structure. Such bundle formation may take place because of capillary forces acting during the drying process following the wet-etching step. In the cross-sectional image one can see that the length of the wires is relatively homogeneous, around 5.5 µm. The XRD diffractogram obtained over structures (i.e.), SiNWs annealed and un-annealed (UA) around (004) atomic plane. Fig. 2, shows a variation in FWHM of peak, which is strongly influenced by strain-relaxation related phenomena [12]. For (UA) SiNWs the XRD plot showed a peak along with broad hump, which when annealed at 700°C showed a sharp feature. Such an effect can be attributed to structural defects and consequent strain relaxation phenomena in nanowires, which arise due to bending and torsion as has been well-documented in a study by Romanitan *et. al.* [12].

B. Respiratory sensing

The human respiratory sensing was investigated using various SiNWs based sensors, as shown in Fig. 3. All structures were tested for three different breathing modes i.e., normal, rapid, and deep breathing, and are labeled respectively in Fig. 3. In order to show the repeatability of the measurements, two breathing sequences are shown for each mode. For SiNWs (both annealed and UA) there is a significant drift in the resistance baseline with time (indicated by arrow), unlike Ge-coated SiNWs in both UA-state and annealed at 450 and 700°C. We attribute this difference to the higher Ge-hole mobility as compared to Si. Additionally, for the bare SiNWs and for two samples coated with Ge, UA and annealed at 450°C, the amplitude of the resistance waves caused by breath is higher than for the Ge-SiNWs annealed at 700°C. However, the sensitivity to capture detailed features of the resistance oscillations, with lower response and recovery time, along with several non-periodic kinks during exhaling and inhaling breathing cycles, may vary between our samples. Such detailed features in breathing profile can be visualized in the differential plots in Fig. 4(a-c). We can see differences that may possibly be related to breathing details, but also to internal sample behavior, such as delayed response, hysteresis, or other transient phenomena to be studied separately [13].

The sensor samples were mounted on a ceramic chip having patterned interdigital Au-electrode. Thin Al-wires were attached between co-planar contacts on sample and electrodes on ceramic chip. The sample was than mounted firmly on to philtrum using a double-sided tape, while the thin coaxial cables between the signal processing unit and sample were properly dressed within a canula tube to avoid any loose connections and/or interference with unintended objects. A schematic illustration of setup is shown in Fig. 5(a).

Fig. 5(b) shows the response of a sensor (Ge coated SiNWs annealed at 700°C) to periodic monitoring of the human breathing. It can be observed that the sensor can efficiently detect the different breathing states i.e., in our case normal, rapid, and deep breathing, Fig. 5(c). We want to emphasize that the fabrications of our samples is considerable simpler than those with complex multi-step process and materials [4], [14]–[16], particularly composite fibres or polymers combined

Authorized licensed use limited to: Reykjavik University. Downloaded on November 11,2022 at 13:51:31 UTC from IEEE Xplore. Restrictions apply.

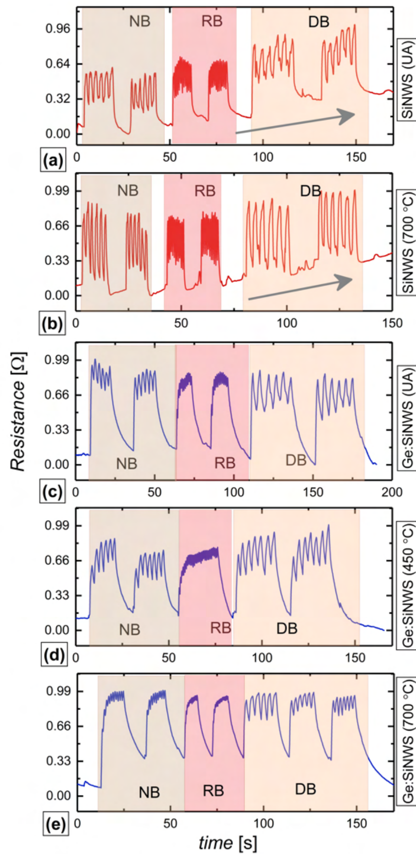

Fig. 3. Room-temperature resistance change as a function of time for (a) UA-SiNWs (b) SiNWs annealed at 700°C, (c) UA-Ge:SiNWs and annealed Ge:SiNWs at (d) 450°C and (e) 700°C, respectively, under normal (NB), rapid (RB), and deep (DB) breathing, also represented as highlighted regions.

with conductive nano-materials like metals, carbon nano tubes or graphene, which are often unstable and tend to degrade in ambient atmosphere over time.

Our sensors were able to capture breathing patterns without losing any features. It is to mention here that the waveform obtained during breathing is assumed to mimic the intended breath modes, while a discontinuity between waves may indicate a potential menace. Therefore, our sensors can provide a possible indication of risky situation, for instance in case of sleep apnea, or other breathing threats like f.ex. choking and asthma. Moreover, our samples were tested for re-usability, after aging them for four weeks. The samples were also tested for longer and repeated breathing cycles. A longer breathing sequence is shown in Fig. 6, as a differential plot (dR/dt vs time), for NB and RB breathing modes, where the inset in the NB plot shows the repeatability of the signal.

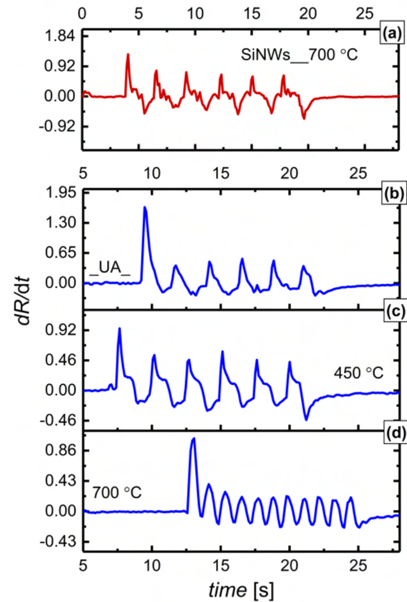

Fig. 4. Differential plots obtained from Fig. 3 of NB states for (a) SiNWs annealed at 700C°C (b) UA-Ge:SiNWs and annealed Ge:SiNWs at (c) 450 °C and (d) 700°C, prospectively.

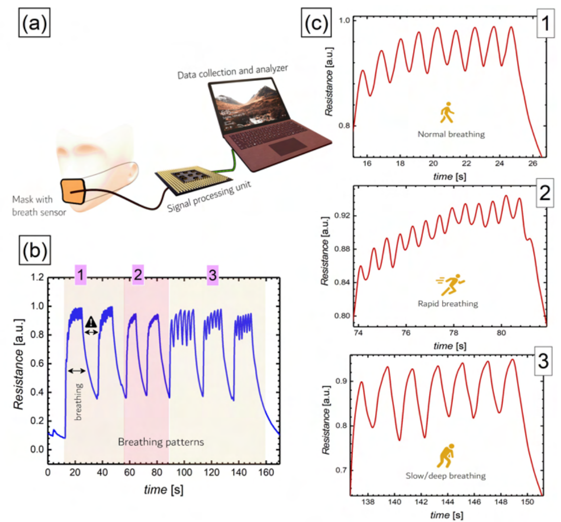

Fig. 5. (a) Schematic of the respiratory setup utilized. (b) The breathing response in real time recorded using annealed (700°C) Ge:SiNWs. (c) The data marked as 1, 2 and 3 expanded.

Authorized licensed use limited to: Reykjavik University. Downloaded on November 11,2022 at 13:51:31 UTC from IEEE Xplore. Restrictions apply.

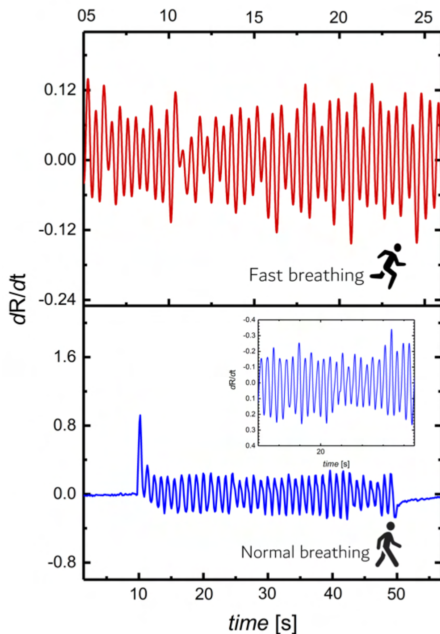

Fig. 6. Differential plot for Ge:SiNWs structure annealed at 700°C, 5 min, under RB (upper plot) and NB (lower plot) modes for an increased number of cycles. The sensor was tested again under similar condition for repeatability the results from which are shown in an inset for NB mode.

IV. Conclusion

In conclusion, we synthesized random arrays of SiNWs by MACE for application in respiratory sensing. The obtained structure were characterized via XRD and SEM showing SiNWs of ~ 5.5 μm, bundled together. The structures were further treated either by rapid thermal annealing and/or coated with Ge films with aim to increase the sensitivity and efficiency. It was observed that SiNWs coated with Ge and annealed for 5 min at 700°C resulted in higher efficiency, faster response, and improved signal profile, without any baseline drift in resistance. We have demonstrated the fabrication of portable, easy to fabricate, and wearable sensor with a great potential for application in devices intended to monitor a human respiratory profile and for other possible applications of pressure sensing.

Acknowledgment

This work was supported by Reykjavik University Ph.D. fund no. 220006 and the Icelandic Research Fund Grant no. 218029-051. We are grateful to Rodica Plugaru and Neculai Plugaru for discussions.

References

[1] X. Wang, Y. Deng, X. Chen, P. Jiang, Y. K. Cheung, and H. Yu, “An ultrafast-response and flexible humidity sensor for human respiration monitoring and noncontact safety warning,” *Microsystems & Nanoengineering 2021 7:1*, vol. 7, pp. 1–11, nov 2021.

[2] R. Ghosh, M. S. Song, J. Park, Y. Tchoe, P. Guha, W. Lee, Y. Lim, B. Kim, S.-W. Kim, M. Kim, *et al.*, “Fabrication of piezoresistive si nanorod-based pressure sensor arrays: A promising candidate for portable breath monitoring devices,” *Nano Energy*, vol. 80, p. 105537, 2021.

[3] Y. Liu, H. Wang, W. Zhao, M. Zhang, H. Qin, and Y. Xie, “Flexible, Stretchable Sensors for Wearable Health Monitoring: Sensing Mechanisms, Materials, Fabrication Strategies and Features,” *Sensors 2018, Vol. 18, Page 645*, vol. 18, p. 645, feb 2018.

[4] C. Lou, K. Hou, W. Zhu, X. Wang, X. Yang, R. Dong, H. Chen, L. Guo, and X. Liu, “Human respiratory monitoring based on schottky resistance humidity sensors,” *Materials*, vol. 13, no. 2, p. 430, 2020.

[5] E. Fakhri, M. Sultan, A. Manolescu, S. Ingvarsson, N. Plugaru, R. Plugaru, and H. Svavarsson, “Synthesis and photoluminescence study of silicon nanowires obtained by metal assisted chemical etching,” in *2021 International Semiconductor Conference (CAS)*, pp. 147–150, IEEE, 2021.

[6] A. Lugstein, M. Steinmair, A. Steiger, H. Kosina, and E. Bertagnolli, “Anomalous piezoresistance effect in ultrastrained silicon nanowires,” *Nano letters*, vol. 10, no. 8, pp. 3204–3208, 2010.

[7] C. Kim, H. Ahn, and T. Ji, “Flexible pressure sensors based on silicon nanowire array built by metal-assisted chemical etching,” *IEEE Electron Device Letters*, vol. 41, no. 8, pp. 1233–1236, 2020.

[8] S. Zhang, L. Lou, and C. Lee, “Piezoresistive silicon nanowire based nanoelectromechanical system cantilever air flow sensor,” *Applied Physics Letters*, vol. 100, no. 2, p. 023111, 2012.

[9] E. Fakhri, R. Plugaru, M. T. Sultan, T. H. Kristinsson, H. O. Árnason, N. Plugaru, A. Manolescu, S. Ingvarsson, and H. G. Svavarsson, “Piezoresistance characterization of silicon nanowires in uniaxial and isostatic pressure variation,” arXiv:2206.04991, 2022.

[10] S. Zhang, L. Lou, T. Wang, W. M. Tsang, D.-L. Kwong, and C. Lee, “Characterizations of silicon nanowires (sinws) embedded nems sensors and for potential biomedical applications,” in *2013 IEEE MTT-S International Microwave Workshop Series on RF and Wireless Technologies for Biomedical and Healthcare Applications (IMWS-BIO)*, pp. 1–3, IEEE, 2013.

[11] M. T. Sultan, J. T. Gudmundsson, A. Manolescu, V. S. Teodorescu, M. L. Ciurea, and H. G. Svavarsson, “Efficacy of annealing and fabrication parameters on photo-response of SiGe in TiO2 matrix—,” *Nanotechnology*, vol. 30, p. 365604, jun 2019.

[12] C. Romanitan, M. Kusko, M. Popescu, P. Varasteanu, A. Radoi, and C. Pachiu, “Unravelling the strain relaxation processes in silicon nanowire arrays by X-ray diffraction,” *Journal of Applied Crystallography*, vol. 52, pp. 1077–1086, sep 2019.

[13] R. Plugaru, E. Fakhri, C. Romanitan, I. Mihalache, G. Craciun, N. Plugaru, H. O. Árnason, M. T. Sultan, G. A. Nemnes, S. Ingvarsson, H. G. Svavarsson, and A. Manolescu, “Structure and electrical behavior of silicon nanowires prepared by mace process,” arXiv:2206.05006, 2022.

[14] H. Shi, R. Wang, P. Yu, J. Shi, and L. Liu, “Facile environment-friendly peptide-based humidity sensor for multifunctional applications,” *Applied Nanoscience (Switzerland)*, vol. 11, pp. 961–969, mar 2021.

[15] J. He, P. Xiao, J. Shi, Y. Liang, W. Lu, Y. Chen, W. Wang, P. Théato, S. W. Kuo, and T. Chen, “High Performance Humidity Fluctuation Sensor for Wearable Devices via a Bioinspired Atomic-Precise Tunable Graphene-Polymer Heterogeneous Sensing Junction,” *Chemistry of Materials*, vol. 30, pp. 4343–4354, jul 2018.

[16] S. Kundu, R. Majumder, R. Ghosh, M. Pradhan, S. Roy, P. Singha, D. Ghosh, A. Banerjee, D. Banerjee, and M. Pal Chowdhury, “Relative humidity sensing properties of doped polyaniline-encased multiwall carbon nanotubes: wearable and flexible human respiration monitoring application,” *Journal of Materials Science*, vol. 55, pp. 3884–3901, mar 2020.

Authorized licensed use limited to: Reykjavik University. Downloaded on November 11,2022 at 13:51:31 UTC from IEEE Xplore. Restrictions apply.

Bibliography

[1] J. Zhu, X. Liu, Q. Shi, *et al.*, “Development trends and perspectives of future sensors and mems/nems,” *Micromachines*, vol. 11, no. 1, p. 7, 2019.

[2] D. Nunes, A. Pimentel, A. Gonçalves, *et al.*, “Metal oxide nanostructures for sensor applications,” *Semiconductor Science and Technology*, vol. 34, no. 4, p. 043 001, 2019.

[3] R. Chen, T.-T. D. Tran, K. W. Ng, *et al.*, “Nanolasers grown on silicon,” *Nature Photonics*, vol. 5, no. 3, pp. 170–175, 2011.

[4] J. Appenzeller, J. Knoch, M. T. Bjork, H. Riel, H. Schmid, and W. Riess, “Toward nanowire electronics,” *IEEE Transactions on electron devices*, vol. 55, no. 11, pp. 2827–2845, 2008.

[5] W. Heywang and K. Zaininger, “Silicon: The semiconductor material,” in *Silicon*, Springer, 2004, pp. 25–42.

[6] H. R. Heris, M. Kateb, S. I. Erlingsson, and A. Manolescu, “Thermoelectric properties of tubular nanowires in the presence of a transverse magnetic field,” *Nanotechnology*, vol. 31, no. 42, p. 424 006, 2020.

[7] K.-Q. Peng, X. Wang, L. Li, Y. Hu, and S.-T. Lee, “Silicon nanowires for advanced energy conversion and storage,” *Nano Today*, vol. 8, no. 1, pp. 75–97, 2013.

[8] A. I. Boukai, Y. Bunimovich, J. Tahir-Kheli, J.-K. Yu, W. A. Goddard Iii, and J. R. Heath, “Silicon nanowires as efficient thermoelectric materials,” *nature*, vol. 451, no. 7175, pp. 168–171, 2008.

[9] W. Cheng, L. Yu, D. Kong, *et al.*, “Fast-response and low-hysteresis flexible pressure sensor based on silicon nanowires,” *IEEE Electron Device Letters*, vol. 39, no. 7, pp. 1069–1072, 2018.

[10] S. Zhang, L. Lou, and C. Lee, “Piezoresistive silicon nanowire based nanoelectromechanical system cantilever air flow sensor,” *Applied Physics Letters*, vol. 100, no. 2, p. 023 111, 2012.

[11] R. Ghosh, M. S. Song, J. B. Park, *et al.*, "Fabrication of piezoresistive Si nanorod-based pressure sensor arrays: A promising candidate for portable breath monitoring devices," *Nano Energy*, vol. 80, p. 105 537, Feb. 2021, ISSN: 2211-2855. DOI: 10.1016/J.NANOEN.2020.105537.

[12] E. C. Garnett and P. Yang, "Silicon nanowire radial p- n junction solar cells," *Journal of the American Chemical Society*, vol. 130, no. 29, pp. 9224–9225, 2008.

[13] S. A. Razek, M. A. Swillam, and N. K. Allam, "Vertically aligned crystalline silicon nanowires with controlled diameters for energy conversion applications: Experimental and theoretical insights," *Journal of Applied Physics*, no. 19, p. 194 305, 2014.

[14] E. F. Pecora, N. Lawrence, P. Gregg, *et al.*, "Nanopatterning of silicon nanowires for enhancing visible photoluminescence," *Nanoscale*, vol. 4, no. 9, pp. 2863–2866, 2012.

[15] K. A. Gonchar, D. V. Moiseev, I. V. Bozhev, and L. A. Osminkina, "Influence of h2o2 concentration on the structural and photoluminescent properties of porous silicon nanowires fabricated by metal-assisted chemical etching," *Materials Science in Semiconductor Processing*, vol. 125, p. 105 644, 2021.

[16] M. Dawood, S. Tripathy, S. Dolmanan, T. Ng, H. Tan, and J. Lam, "Influence of catalytic gold and silver metal nanoparticles on structural, optical, and vibrational properties of silicon nanowires synthesized by metal-assisted chemical etching," *Journal of Applied Physics*, vol. 112, no. 7, p. 073 509, 2012.

[17] V. A. Sivakov, F. Voigt, A. Berger, G. Bauer, and S. H. Christiansen, "Roughness of silicon nanowire sidewalls and room temperature photoluminescence," *Physical Review B*, vol. 82, no. 12, p. 125 446, 2010.

[18] M. Naffeti, P. A. Postigo, R. Chtourou, and M. A. Zaïbi, "Elucidating the effect of etching time key-parameter toward optically and electrically-active silicon nanowires," *Nanomaterials*, vol. 10, no. 3, p. 404, 2020.

[19] A. Fiorillo, C. Critello, and S. Pullano, "Theory, technology and applications of piezoresistive sensors: A review," *Sensors and Actuators A: Physical*, vol. 281, pp. 156–175, 2018.

[20] S. Stassi, V. Cauda, G. Canavese, and C. F. Pirri, "Flexible tactile sensing based on piezoresistive composites: A review," *Sensors*, vol. 14, no. 3, pp. 5296–5332, 2014.

[21] J. Li, L. Fang, B. Sun, X. Li, and S. H. Kang, "Recent progress in flexible and stretchable piezoresistive sensors and their applications," *Journal of the Electrochemical Society*, vol. 167, no. 3, p. 037 561, 2020.

[22] K. Winkler, E. Bertagnolli, and A. Lugstein, “Origin of anomalous piezoresistive effects in vls grown si nanowires,” *Nano letters*, vol. 15, no. 3, pp. 1780–1785, 2015.

[23] S. Basu, *Crystalline Silicon: Properties and Uses*. BoD–Books on Demand, 2011.

[24] T. Mikolajick, A. Heinzig, J. Trommer, *et al.*, “Silicon nanowires–a versatile technology platform,” *physica status solidi (RRL)–Rapid Research Letters*, vol. 7, no. 10, pp. 793–799, 2013.

[25] a. R. Wagner and s. W. Ellis, “Vapor-liquid-solid mechanism of single crystal growth,” *Applied physics letters*, vol. 4, no. 5, pp. 89–90, 1964.

[26] Z. Huang, H. Fang, and J. Zhu, “Fabrication of silicon nanowire arrays with controlled diameter, length, and density,” *Advanced materials*, vol. 19, no. 5, pp. 744–748, 2007.

[27] M. Shao, D. D. D. Ma, and S.-T. Lee, “Silicon nanowires–synthesis, properties, and applications,” *European Journal of Inorganic Chemistry*, vol. 2010, no. 27, pp. 4264–4278, 2010.

[28] L. Schubert, P. Werner, N. Zakharov, *et al.*, “Silicon nanowhiskers grown on< 111> si substrates by molecular-beam epitaxy,” *Applied Physics Letters*, vol. 84, no. 24, pp. 4968–4970, 2004.

[29] Z. Huang, N. Geyer, P. Werner, J. De Boor, and U. Gösele, “Metal-assisted chemical etching of silicon: A review: In memory of prof. ulrich gösele,” *Advanced materials*, vol. 23, no. 2, pp. 285–308, 2011.

[30] H. G. Svavarsson, B. H. Hallgrimsson, M. Niraula, K. J. Lee, and R. Magnusson, “Large arrays of ultra-high aspect ratio periodic silicon nanowires obtained via top–down route,” *Applied Physics A*, vol. 122, no. 2, pp. 1–6, 2016.

[31] A. A. Leonardi, M. J. L. Faro, and A. Irrera, “Silicon nanowires synthesis by metal-assisted chemical etching: A review,” *Nanomaterials*, vol. 11, no. 2, p. 383, 2021.

[32] W. Thomson, “Xix. on the electro-dynamic qualities of metals:—effects of magnetization on the electric conductivity of nickel and of iron,” *Proceedings of the Royal Society of London*, no. 8, pp. 546–550, 1857.

[33] P. W. Bridgman, “The resistance of 72 elements, alloys and compounds to 100,000 kg/cm2,” in *Volume VII Collected Experimental Papers, Volume VII*, Harvard University Press, 2013, pp. 4113–4197.

[34] A. Rowe, “Piezoresistance in silicon and its nanostructures,” *Journal of Materials Research*, vol. 29, no. 6, pp. 731–744, 2014.

[35] R. Bogue, “Recent developments in mems sensors: A review of applications, markets and technologies,” *Sensor Review*, 2013.

[36] S. S. Kumar and B. Pant, "Polysilicon thin film piezoresistive pressure microsensor: Design, fabrication and characterization," *Microsystem Technologies*, vol. 21, no. 9, pp. 1949–1958, 2015.

[37] D. Colman, R. Bate, and J. Mize, "Mobility anisotropy and piezoresistance in silicon p-type inversion layers," *Journal of Applied Physics*, vol. 39, no. 4, pp. 1923–1931, 1968.

[38] G. Dorda, I. Eisele, and H. Gesch, "Many-valley interactions in n-type silicon inversion layers," *Physical Review B*, vol. 17, no. 4, p. 1785, 1978.

[39] R. Craddock, "Sensors based on silicon strain gauges," in *IEE Colloquium on Sensing Via Strain*, IET, 1993, pp. 5–1.

[40] C. S. Smith, "Piezoresistance effect in germanium and silicon," *Physical review*, vol. 94, no. 1, p. 42, 1954.

[41] O. N. Tufte, P. D. Chapman, and D. Long, "Silicon diffused-element piezoresistive diaphragms," *Journal of Applied Physics*, vol. 33, 1962.

[42] M. Tortonese, R. C. Barrett, and C. F. Quate, "Atomic resolution with an atomic force microscope using piezoresistive detection," *Applied Physics Letters*, vol. 62, p. 834, 1993.

[43] Y. Ning, Y. Loke, and G. McKinnon, "Fabrication and characterization of high g-force, silicon piezoresistive accelerometers," *Sensors and Actuators A: Physical*, vol. 48, pp. 55–61, 1995.

[44] K. Wee, G. Kang, J. Park, *et al.*, "Novel electrical detection of label-free disease marker proteins using piezoresistive self-sensing micro-cantilevers," *Biosensors and Bioelectronics*, vol. 20, pp. 1932–1938, 2005.

[45] J. Kim, K. T. Park, H. C. Kim, and K. Chun, "Fabrication of a piezoresistive pressure sensor for enhancing sensitivity using silicon nanowire," in *TRANSDUCERS 2009-2009 International Solid-State Sensors, Actuators and Microsystems Conference*, IEEE, 2009, pp. 1936–1939.

[46] R. He, X. Feng, M. Roukes, and P. Yang, "Self-transducing silicon nanowire electromechanical systems at room temperature," *Nano letters*, vol. 8, no. 6, pp. 1756–1761, 2008.

[47] J. S. Milne, A. C. H. Rowe, S. Arscott, and C. Renner, "Giant piezoresistance effects in silicon nanowires and microwires," *Phys. Rev. Lett.*, vol. 105, p. 226 802, 22 Nov. 2010. DOI: 10.1103/PhysRevLett.105.226802. [Online]. Available: https://link.aps.org/doi/10.1103/PhysRevLett.105.226802.

[48] B. W. Soon, P. Neuzil, C. C. Wong, J. Reboud, H. H. Feng, and C. Lee, "Ultrasensitive nanowire pressure sensor makes its debut," *Procedia Engineering*, vol. 5, pp. 1127–1130, 2010.

[49] X. Deng, Z. Zhang, and G. Tang, "Applied physics letters, 100," *Article ID*, vol. 63107, 2012.

[50] M. Sansa, M. Fernández-Regúlez, Á. San Paulo, and F. Pérez-Murano, "Electrical transduction in nanomechanical resonators based on doubly clamped bottom-up silicon nanowires," *Applied Physics Letters*, vol. 101, no. 24, p. 243 115, 2012.

[51] P. E. Allain, F. Parrain, A. Bosseboeuf, S. Mâaroufi, P. Coste, and A. Walther, "Large-range mems motion detection with subangström noise level using an integrated piezoresistive silicon nanowire," *Journal of microelectromechanical systems*, vol. 22, no. 3, pp. 716–722, 2013.

[52] R. He and P. Yang, "Giant piezoresistance effect in silicon nanowires," *Nature nanotechnology*, vol. 1, no. 1, pp. 42–46, 2006.

[53] D. Gao, Z. Yang, L. Zheng, and Z. Kun, "Piezoresistive effect of n-type $<$ 111 $>$-oriented si nanowires under large tension/compression," *Nanotechnology*, vol. 28, p. 095 702, 2017.

[54] S. Huang, B. Zhang, Y. Lin, C.-S. Lee, and X. Zhang, "Compact biomimetic hair sensors based on single silicon nanowires for ultrafast and highly-sensitive airflow detection," *Nano Letters*, vol. 21, no. 11, pp. 4684–4691, 2021.

[55] T. Toriyama, Y. Tanimoto, and S. Sugiyama, "Single crystal silicon nano-wire piezoresistors for mechanical sensors," *Journal of microelectromechanical systems*, vol. 11, no. 5, pp. 605–611, 2002.

[56] M. Messina and J. Njuguna, "Potential of silicon nanowires structures as nanoscale piezoresistors in mechanical sensors," in *IOP Conference Series: Materials Science and Engineering*, IOP Publishing, vol. 40, 2012, p. 012 038.

[57] P. Neuzil, C. C. Wong, and J. Reboud, "Electrically controlled giant piezoresistance in silicon nanowires," *Nano letters*, vol. 10, no. 4, pp. 1248–1252, 2010.

[58] A. Lugstein, M. Steinmair, A. Steiger, H. Kosina, and E. Bertagnolli, "Anomalous piezoresistance effect in ultrastrained silicon nanowires," *Nano letters*, vol. 10, no. 8, pp. 3204–3208, 2010.

[59] J. M. Nichol, E. R. Hemesath, L. J. Lauhon, and R. Budakian, "Displacement detection of silicon nanowires by polarization-enhanced fiber-optic interferometry," *Applied Physics Letters*, vol. 93, no. 19, p. 193 110, 2008.

[60] C. Lou, K. Hou, W. Zhu, *et al.*, "Human Respiratory Monitoring Based on Schottky Resistance Humidity Sensors," *Materials 2020, Vol. 13, Page 430*, vol. 13, no. 2, p. 430, Jan. 2020. DOI: 10.3390/MA13020430. [Online]. Available: https://www.mdpi.com/1996-1944/13/2/430/htm%20https://www.mdpi.com/1996-1944/13/2/430.

[61] S. Pidashetti and K. B. Balavalad, “Design and development of silicon nanowire-based pressure sensor for medical applications,” in *Smart Intelligent Computing and Applications, Volume 2*, Springer, 2022, pp. 93–101.

[62] L. Lou, S. Zhang, W.-T. Park, J. Tsai, D.-L. Kwong, and C. Lee, “Optimization of nems pressure sensors with a multilayered diaphragm using silicon nanowires as piezoresistive sensing elements,” *Journal of Micromechanics and Microengineering*, vol. 22, no. 5, p. 055 012, 2012.

[63] X. Chen, C. K. Wong, C. A. Yuan, and G. Zhang, “Nanowire-based gas sensors,” *Sensors and Actuators B: Chemical*, vol. 177, pp. 178–195, 2013.

[64] F. Demami, L. Ni, R. Rogel, A.-C. Salaun, and L. Pichon, “Silicon nanowires based resistors as gas sensors,” *Sensors and Actuators B: Chemical*, vol. 170, pp. 158–162, 2012.

[65] A. Mirzaei, S. Y. Kang, S.-W. Choi, *et al.*, “Fabrication and gas sensing properties of vertically aligned si nanowires,” *Applied Surface Science*, vol. 427, pp. 215–226, 2018.

[66] N. Shehada, G. Bronstrup, K. Funka, S. Christiansen, M. Leja, and H. Haick, “Ultrasensitive silicon nanowire for real-world gas sensing: Noninvasive diagnosis of cancer from breath volatolome,” *Nano letters*, vol. 15, no. 2, pp. 1288–1295, 2015.

[67] K.-Q. Peng, X. Wang, and S.-T. Lee, “Gas sensing properties of single crystalline porous silicon nanowires,” *Applied Physics Letters*, vol. 95, no. 24, pp. 243–112, 2009.

[68] B. Zhang, J. Yu, and X. Zhang, “A perspective on ultralong silicon nanowires for flexible sensors,” *Applied Physics Letters*, vol. 120, no. 13, p. 130 501, 2022.

[69] C. Kim, H. Ahn, and T. Ji, “Flexible pressure sensors based on silicon nanowire array built by metal-assisted chemical etching,” *IEEE Electron Device Letters*, vol. 41, no. 8, pp. 1233–1236, 2020.

[70] W. Cheng, L. Yu, D. Kong, *et al.*, “Fast-response and low-hysteresis flexible pressure sensor based on silicon nanowires,” *IEEE Electron Device Letters*, vol. 39, no. 7, pp. 1069–1072, 2018.

[71] H. Cui, S. Li, S. Deng, H. Chen, and C. Wang, “Flexible, transparent, and free-standing silicon nanowire sers platform for in situ food inspection,” *Acs Sensors*, vol. 2, no. 3, pp. 386–393, 2017.

[72] B.-C. Zhang, J.-S. Jie, Z.-B. Shao, S.-Y. Huang, L. He, and X.-H. Zhang, “One-step growth of large-area silicon nanowire fabrics for high-performance multifunctional wearable sensors,” *Nano Research*, vol. 12, no. 11, pp. 2723–2728, 2019.

[73] N. Shehada, J. C. Cancilla, J. S. Torrecilla, *et al.*, "Silicon nanowire sensors enable diagnosis of patients via exhaled breath," *ACS nano*, vol. 10, no. 7, pp. 7047–7057, 2016.

[74] T.-D. Nguyen and J. S. Lee, "Recent development of flexible tactile sensors and their applications," *Sensors*, vol. 22, no. 1, p. 50, 2021.

[75] R. Ghosh, M. S. Song, J. Park, *et al.*, "Fabrication of piezoresistive si nanorod-based pressure sensor arrays: A promising candidate for portable breath monitoring devices," *Nano Energy*, vol. 80, p. 105 537, 2021.

[76] D. Shiri, Y. Kong, A. Buin, and M. P. 1. Anantram, "Strain induced change of bandgap and effective mass in silicon nanowires," *Applied Physics Letters*, vol. 93, p. 07 314, 2008.

[77] J. Zhang, Y. Zhao, Y. Ge, M. Li, L. Yang, and X. Mao, "Design optimization and fabrication of high-sensitivity soi pressure sensors with high signal-to-noise ratios based on silicon nanowire piezoresistors," *Micromachines*, vol. 7, no. 10, p. 187, 2016.

[78] L. O. M. Chua, "The missing circuit element. circuit theory," *IEEE Trans*, vol. 18, pp. 507–519, 1971.

[79] Y. Yang, P. Gao, S. Gaba, T. Chang, X. Pan, and W. Lu, "Observation of conducting filament growth in nanoscale resistive memories," *Nature communications*, vol. 3, no. 1, pp. 1–8, 2012.

[80] B. Hwang and J.-S. Lee, "Hybrid organic-inorganic perovskite memory with long-term stability in air," *Scientific reports*, vol. 7, no. 1, pp. 1–7, 2017.

[81] A. Sawa, "Resistive switching in transition metal oxides," *Materials today*, vol. 11, no. 6, pp. 28–36, 2008.

[82] A. Rouis, N. Hizem, M. Hassen, and A. Kalboussi, "Electrical properties of silicon nanowires schottky barriers prepared by mace at different etching time," *Silicon*, vol. 14, no. 9, pp. 4731–4737, 2022.

[83] S. P. Adhikari, M. P. Sah, H. Kim, and L. O. Chua, "Three fingerprints of memristor," *IEEE Transactions on Circuits and Systems I: Regular Papers*, vol. 60, no. 11, pp. 3008–3021, 2013.

[84] W. Schottky, "Halbleitertheorie der sperrschicht," *Naturwissenschaften*, vol. 26, no. 52, pp. 843–843, 1938.

[85] Z. Zhang and J. T. Yates Jr, "Band bending in semiconductors: Chemical and physical consequences at surfaces and interfaces," *Chemical reviews*, vol. 112, no. 10, pp. 5520–5551, 2012.

[86] W. M. Haynes, *CRC handbook of chemistry and physics*. CRC press, 2016.

[87] P. Mazzolini, "Functional properties control of doped tio2 for transparent electrodes and photoanodes," 2015.

[88] D. Dimova-Malinovska, M. Sendova-Vassileva, N. Tzenov, and M. Kamenova, "Preparation of thin porous silicon layers by stain etching," *Thin solid films*, vol. 297, no. 1-2, pp. 9–12, 1997.

[89] X. Li and P. Bohn, "Metal-assisted chemical etching in hf/h 2 o 2 produces porous silicon," *Applied Physics Letters*, vol. 77, no. 16, pp. 2572–2574, 2000.

[90] K.-Q. Peng, Y.-J. Yan, S.-P. Gao, and J. Zhu, "Synthesis of large-area silicon nanowire arrays via self-assembling nanoelectrochemistry," *Advanced materials*, vol. 14, no. 16, pp. 1164–1167, 2002.

[91] H. Fang, Y. Wu, J. Zhao, and J. Zhu, "Silver catalysis in the fabrication of silicon nanowire arrays," *Nanotechnology*, vol. 17, no. 15, p. 3768, 2006.

[92] S.-W. Chang, V. P. Chuang, S. T. Boles, C. A. Ross, and C. V. Thompson, "Densely packed arrays of ultra-high-aspect-ratio silicon nanowires fabricated using block-copolymer lithography and metal-assisted etching," *Advanced functional materials*, vol. 19, no. 15, pp. 2495–2500, 2009.

[93] K. Peng, Y. Wu, H. Fang, X. Zhong, Y. Xu, and J. Zhu, "Uniform, axial-orientation alignment of one-dimensional single-crystal silicon nanostructure arrays," *Angewandte Chemie*, vol. 117, no. 18, pp. 2797–2802, 2005.

[94] S. Chattopadhyay and P. W. Bohn, "Direct-write patterning of microstructured porous silicon arrays by focused-ion-beam pt deposition and metal-assisted electroless etching," *Journal of applied physics*, vol. 96, no. 11, pp. 6888–6894, 2004.

[95] D. J. Carney, H. G. Svavarsson, H. Hemmati, A. Fannin, J. W. Yoon, and R. Magnusson, "Refractometric sensing with periodic nano-indented arrays: Effect of structural dimensions," *Sensors*, vol. 19, no. 4, p. 897, 2019.

[96] A. Bashir, T. I. Awan, A. Tehseen, M. B. Tahir, and M. Ijaz, "Chapter 3—interfaces and surfaces," *Chemistry of Nanomaterials; Awan, TI, Bashir, A., Tehseen, A., Eds*, pp. 51–87, 2020.

[97] B. G. Streetman, S. Banerjee, *et al.*, *Solid state electronic devices*. Pearson/Prentice Hall Upper Saddle River, 2006, vol. 10.

[98] H. Okayama, K. Fukami, R. Plugaru, T. Sakka, and Y. H. Ogata, "Ordering and disordering of macropores formed in prepatterned p-type silicon," *Journal of The Electrochemical Society*, vol. 157, no. 1, p. D54, 2009.

[99] I. Leontis, A. Othonos, and A. G. Nassiopoulou, "Structure, morphology, and photoluminescence of porous si nanowires: Effect of different chemical treatments," *Nanoscale research letters*, vol. 8, no. 1, pp. 1–7, 2013.

[100] J. C. Doll and B. L. Pruitt, *Piezoresistor design and applications* (Microsystems and nanosystems), eng. New York: Springer Science + Business Media, 2013, ISBN: 978-1-4614-8517-9.

[101] K. Matsuda, K. Suzuki, K. Yamamura, and Y. Kanda, "Nonlinear piezoresistance effects in silicon," *Journal of applied physics*, vol. 73, no. 4, pp. 1838–1847, 1993.

[102] Y.-M. Niquet, C. Delerue, and C. Krzeminski, "Effects of strain on the carrier mobility in silicon nanowires," *Nano letters*, vol. 12, no. 7, pp. 3545–3550, 2012.

[103] X. Zhou, J. Hu, C. Li, D. Ma, C. Lee, and S. Lee, "Silicon nanowires as chemical sensors," *Chemical Physics Letters*, vol. 369, no. 1-2, pp. 220–224, 2003.

[104] Y. Qin, Y. Wang, and Y. Liu, "Vertically aligned silicon nanowires with rough surface and its no2 sensing properties," *Journal of Materials Science: Materials in Electronics*, vol. 27, no. 11, pp. 11 319–11 324, 2016.

[105] J. Kim, S. D. Oh, J. H. Kim, D. H. Shin, S. Kim, and S.-H. Choi, "Graphene/si-nanowire heterostructure molecular sensors," *Scientific reports*, vol. 4, no. 1, pp. 1–5, 2014.

[106] P. M. Pataniya, S. A. Bhakhar, M. Tannarana, *et al.*, "Highly sensitive and flexible pressure sensor based on two-dimensional mose2 nanosheets for online wrist pulse monitoring," *Journal of colloid and interface science*, vol. 584, pp. 495–504, 2021.

[107] W. H. Bragg and W. L. Bragg, "The reflection of x-rays by crystals," *Proceedings of the Royal Society of London. Series A, Containing Papers of a Mathematical and Physical Character*, vol. 88, no. 605, pp. 428–438, 1913.

[108] N. E. Widjonarko, "Introduction to advanced x-ray diffraction techniques for polymeric thin films," *Coatings*, vol. 6, no. 4, p. 54, 2016.

[109] M. Birkholz, *Thin film analysis by X-ray scattering*. John Wiley & Sons, 2006.

[110] D. E. Newbury, "Energy-dispersive spectrometry," *Characterization of Materials*, 2002.

[111] D. E. Newbury and N. W. Ritchie, "Elemental mapping of microstructures by scanning electron microscopy-energy dispersive x-ray spectrometry (sem-eds): Extraordinary advances with the silicon drift detector (sdd)," *Journal of Analytical Atomic Spectrometry*, vol. 28, no. 7, pp. 973–988, 2013.

[112] Y. Cui and C. M. Lieber, "Functional nanoscale electronic devices assembled using silicon nanowire building blocks," *science*, vol. 291, no. 5505, pp. 851–853, 2001.

[113] X. Chen, J. Zhang, Z. Wang, Q. Yan, and S. Hui, "Humidity sensing behavior of silicon nanowires with hexamethyldisilazane modification," *Sensors and Actuators B: Chemical*, vol. 156, no. 2, pp. 631–636, 2011.

[114] M. Akbari-Saatlu, M. Procek, C. Mattsson, *et al.*, "Silicon nanowires for gas sensing: A review," *Nanomaterials*, vol. 10, no. 11, p. 2215, 2020.

[115] X. Yang, Y. Wang, and T. Li, "High performance humidity sensor by using silicon nanowire array," in *2018 IEEE 13th Annual International Conference on Nano/Micro Engineered and Molecular Systems (NEMS)*, IEEE, 2018, pp. 603–606.

[116] H. Li, J. Zhang, B. Tao, L. Wan, and W. Gong, "Investigation of capacitive humidity sensing behavior of silicon nanowires," *Physica E: Low-dimensional Systems and Nanostructures*, vol. 41, no. 4, pp. 600–604, 2009.